

University of Southampton Research Repository ePrints Soton

Copyright © and Moral Rights for this thesis are retained by the author and/or other copyright owners. A copy can be downloaded for personal non-commercial research or study, without prior permission or charge. This thesis cannot be reproduced or quoted extensively from without first obtaining permission in writing from the copyright holder/s. The content must not be changed in any way or sold commercially in any format or medium without the formal permission of the copyright holders.

When referring to this work, full bibliographic details including the author, title, awarding institution and date of the thesis must be given e.g.

AUTHOR (year of submission) "Full thesis title", University of Southampton, name of the University School or Department, PhD Thesis, pagination

UNIVERSITY OF SOUTHAMPTON

FACULTY OF NATURAL AND ENVIRONMENTAL SCIENCES

School of Chemistry

**Oxygen evolution electrocatalysts for proton exchange membrane water
electrolysis**

by

Peter William Richardson

Thesis for the degree of Doctor of Philosophy

January 2015

UNIVERSITY OF SOUTHAMPTON

ABSTRACT

FACULTY OF NATURAL AND ENVIRONMENTAL SCIENCES

Chemistry

Thesis for the degree of Doctor of Philosophy

OXYGEN EVOLUTION ELECTROCATALYSTS FOR PROTON EXCHANGE MEMBRANE WATER ELECTROLYSIS

Peter William Richardson

Proton exchange membrane (PEM) water electrolyzers are forecast to become an important intermediary energy storage technology between renewable power sources and energy distribution/usage. This is because they offer a production route to high purity H₂ that is both non-polluting and efficient. Energy stored as H₂ can be converted back to electricity for use in the national grid, pumped into existing natural gas networks or used as a fuel for hydrogen-powered vehicles. The majority of the energy losses in a PEM water electrolyser are associated with the high overpotential that is required for the electrochemical evolution of O₂ that occurs at the anode. The highly oxidising conditions of this reaction coupled to the low pH of the PEM environment restrict electrocatalyst selection to expensive noble metal oxides. Thus to enhance the commercial viability of PEM electrolyzers, the goal of electrocatalyst development for the O₂ evolution reaction is to (i) increase the catalytic performance, (ii) increase the catalyst stability and (iii) reduce the cost of the catalyst components.

In this work a range of iridium-based electrocatalysts with reduced Ir contents have been prepared. Two methods are employed to reduce the Ir content: (i) mixing the Ir with ruthenium to form a binary metal oxide and (ii) dispersing the active Ir phase on an indium tin oxide (ITO) support. Investigation of the electrocatalysts via a combination of different physical and electrochemical characterisation techniques, including a novel in-situ X-ray absorbance experiment, indicates that both approaches produce electrocatalysts with comparable or improved O₂ evolution activity compared to the state-of-the-art iridium oxide (IrO₂) material. However selection of the most appropriate catalyst for PEM electrolysis may ultimately be a compromise between activity, stability and cost.

Contents

Contents	i
DECLARATION OF AUTHORSHIP.....	v
Acknowledgements.....	vii
1. Introduction.....	1
1.1 The energy challenge.....	1
1.1.1 Security of energy supplies.....	2
1.1.2 Climate change	2
1.1.3 Atmospheric pollution.....	3
1.1.4 Meeting the challenge	3
1.2 Hydrogen	4
1.2.1 Hydrogen as an energy carrier.....	4
1.2.2 Hydrogen production	4
1.2.2.1 Reformation of hydrocarbons.....	5
1.2.2.2 Water electrolysis.....	6
1.3 PEM water electrolysis.....	7
1.3.1 General principles	7
1.3.2 Thermodynamics and kinetics	8
1.3.3 Cell structure and components.....	9
1.3.3.1 Proton exchange membranes.....	10
1.3.3.2 Cathode electrocatalysts	11
1.3.3.3 Anode electrocatalysts	12
1.3.3.3.1 The O ₂ evolution reaction	12
1.3.3.3.2 O ₂ evolution electrocatalysts.....	14
1.4 Aims and objectives.....	16
1.5 References.....	17
2. Experimental methods and techniques.....	23
2.1 Reagents and materials	23
2.2 Electrochemical techniques.....	25
2.2.1 Cyclic voltammetry.....	25
2.2.2 Steady state polarization	27
2.2.3 Electrochemistry experimental details	28
2.2.3.1 Thin film rotating disk electrode half-cell	28
2.2.3.2 PEM water electrolyser cell	29
2.2.3.2.1 CCM preparation	29

2.2.3.2.2	PEM electrolyser cell	30
2.3	BET surface area analysis	32
2.3.1	Experimental details	33
2.4	Thermogravimetric analysis	33
2.4.1	Experimental details	34
2.5	X-ray diffraction	34
2.5.1	Experimental details	36
2.6	Electron microscopy and energy dispersive X-ray analysis	36
2.6.1	Transmission electron microscopy (TEM)	36
2.6.2	EDX analysis	37
2.6.3	Experimental details	37
2.7	X-ray absorption spectroscopy (XAS)	37
2.7.1	Theory of XAS.....	38
2.7.2	EXAFS	40
2.7.3	XANES	41
2.7.4	Experimental aspects of XAS.....	43
2.7.4.1	Synchrotron	43
2.7.4.2	Beamline B18	43
2.7.4.3	XAS transmission measurements	43
2.7.4.4	XAS fluorescence measurements	45
2.7.4.5	In-situ electrochemical XAS measurements	45
2.7.4.5.1	Electrode preparation	47
2.7.4.6	Data processing	48
2.8	References	49
3.	Mixed iridium-ruthenium electrocatalysts for O₂ evolution	51
3.1	Introduction.....	51
3.2	Experimental details	54
3.2.1	Preparation of Ir _x Ru _y O ₂ electrocatalysts	54
3.2.2	EDX analysis	55
3.2.3	XRD	55
3.2.4	TEM.....	55
3.2.5	BET.....	55
3.2.6	Electrochemical characterisation	55
3.2.6.1	Cyclic voltammetry	56
3.2.6.2	Steady state polarisation	56
3.2.6.3	PEM electrolyser tests.....	56
3.2.6.3.1	Steady state polarisation curves	56

3.2.6.3.2	Stability test	56
3.2.7	XANES	56
3.3	Results and discussion	58
3.3.1	EDX analysis	58
3.3.2	XRD.....	58
3.3.3	TEM.....	61
3.3.4	BET surface area.....	63
3.3.5	Electrochemical characterisation.....	64
3.3.5.1	Cyclic voltammetry.....	64
3.3.5.2	Steady state polarisation	72
3.3.6	PEM electrolyser cell tests.....	77
3.3.7	XANES analysis	79
3.3.7.1	Ru K-edge	80
3.3.7.2	Ir L ₃ edge	86
3.4	Conclusions.....	93
3.5	References.....	94
4.	Ir/ITO electrocatalysts for the O₂ evolution reaction	97
4.1	Introduction	97
4.2	Experimental details	99
4.2.1	Preparation of supported electrocatalysts by formaldehyde reduction.....	99
4.2.2	EDX analysis	100
4.2.3	XRD.....	100
4.2.4	TEM.....	100
4.2.5	BET	100
4.2.6	TGA.....	100
4.2.7	Electrochemical characterisation.....	100
4.2.7.1	Cyclic voltammetry.....	101
4.2.7.2	Steady state polarisation	101
4.2.7.3	Stability tests	101
4.2.8	PEM electrolyser tests.....	101
4.2.8.1	Polarisation curves	101
4.2.8.2	Stability test.....	102
4.2.9	XANES and EXAFS	102
4.3	Results and discussion	103
4.3.1	Analysis of Ir/ITO catalysts with variable Ir loading	103
4.3.1.1	EDX analysis	103
4.3.1.2	XRD	104

4.3.1.3	TEM.....	105
4.3.1.4	BET surface area.....	107
4.3.1.5	Electrochemical characterisation.....	108
4.3.1.5.1	Cyclic voltammetry	108
4.3.1.5.2	Steady state polarisation.....	110
4.3.1.5.3	Stability test.....	113
4.3.1.6	PEM water electrolyser cell tests	117
4.3.2	Heat treatment of 40 % Ir/ITO	120
4.3.2.1	XRD.....	120
4.3.2.2	TGA.....	121
4.3.2.3	TEM.....	122
4.3.2.4	EXAFS.....	123
4.3.2.5	Electrochemical characterisation.....	125
4.3.2.5.1	Cyclic voltammetry	125
4.3.2.5.2	Steady state polarisation.....	126
4.3.2.6	In situ XANES.....	128
4.4	Conclusions	132
4.5	References	133
5.	Conclusions.....	137
5.1	References	142

DECLARATION OF AUTHORSHIP

I, Peter William Richardson

declare that the thesis entitled

Oxygen evolution electrocatalysts for proton exchange membrane water electrolysis

and the work presented in the thesis are both my own, and have been generated by me as the result of my own original research. I confirm that:

- this work was done wholly or mainly while in candidature for a research degree at this University;
- where any part of this thesis has previously been submitted for a degree or any other qualification at this University or any other institution, this has been clearly stated;
- where I have consulted the published work of others, this is always clearly attributed;
- where I have quoted from the work of others, the source is always given. With the exception of such quotations, this thesis is entirely my own work;
- I have acknowledged all main sources of help;
- where the thesis is based on work done by myself jointly with others, I have made clear exactly what was done by others and what I have contributed myself;
- none of this work has been published before submission

Signed:

Date:.....

Acknowledgements

First of all, I want to thank my supervisor Andrea Russell for giving me the opportunity to study for a PhD, and for her guidance and motivation throughout the last 4 years. I would also like to acknowledge Derek Pletcher and Andrew Hector for their valuable knowledge and discussions. I would like to thank Nick van Dijk and Kris Hyde and the many others at ITM Power who have helped to make this work possible. I am especially grateful to Liz Payne-Johnson, Rachel Lister and Eleanor Wallace for their help with electrolyser assembly and testing. For his help and assistance with setting up the B18 beamline at Diamond Light Source, I would like to thank Diego Gianolio. I would also like to express my thanks to Konstant Venter for his help with the design and the construction of the in situ electrochemical XAS cell. The XAS experiments would not have been possible without your efforts.

I am very grateful to the many members of staff without whom research in the Chemistry department would not be possible: Karl, Keith and Mark in Stores; Anne in the tea room; Lee, Pzemslaw and Paul in the glassblowing workshop; and Alan, Rob and Konstant in the mechanical workshop. A big thanks also to Alistair Clark for his advice with SEM. I must also thank the fantastic electrochemistry community at Southampton, especially my new research group – Phil, Jack, Charlie, Gabriella, Rachel and David – and also the many members of the SCFED Project (www.scfed.net – check it out, it's the future!).

I would like to thank all members of the Russell Group past and present, for their friendship and advice. Gael Chouchelamane for introducing me to electrochemistry, Steve Price for answering so many questions and for proof reading this thesis, Steve Thompson for running the night shifts at Diamond, Emma Barley for helping me complete some of the final experimental work, and Anna Wise for our grand tour of the world's synchrotrons with such exotic locations as San Francisco (twice!), New York, Grenoble, Zurich, Hamburg ... and Didcot.

To Christine and David for their advice and encouragement.

To Mum, Dad, Robert and Jack for their love and support in all that I have done.

And finally to Louise, whose love and support has got me through the highs and lows of doing this PhD. Thank you.

1. Introduction

PEM water electrolyzers are forecast to become an important intermediary energy storage technology between renewable power sources and energy distribution/usage. This is because they offer a production route to high purity H₂ that is both non-polluting and efficient. Energy stored as H₂ can be converted back to electricity for use in the national grid, pumped into existing natural gas networks or used as a fuel for hydrogen-powered vehicles. The majority of the energy losses in a PEM water electrolyser are associated with the high overpotential that is required for the electrochemical evolution of O₂ that occurs at the anode. The highly oxidising conditions of this reaction coupled to the low pH of PEM environment restrict electrocatalyst selection to expensive noble metal oxides. Thus to enhance the commercial viability of PEM electrolyzers, it is imperative to reduce the amount of precious metal used without reducing the activity or stability of the catalyst. This introductory chapter will present the arguments for the use of H₂ as an energy storage medium, followed by an introduction to PEM water electrolyzers and the O₂ evolution reaction, and finally a brief outline of the thesis. Literature reviews relevant to the results presented later in this thesis can be found at the start of each of the results chapters (Chapters 3 and 4).

1.1 The energy challenge

Humans need sources of energy in order to survive. As a species we are dependent on energy and fuels for two of our most basic needs, heating and cooking, as well as a wide array of important industrial processes such as electricity generation, metallurgy, food production and transportation.

The choice of primary energy source is varied. For the majority of human history, wood was burnt for domestic use whilst windmills and watermills were used to power industrial processes. The development of the steam engine in the late 18th Century enabled large scale coal mining, which led to the Industrial Revolution and a move towards fossil fuels; first coal, then petroleum (oil) and later natural gas. The invention of the internal combustion engine (ICE) in the late 19th Century and its application in the transportation sector further increased the demand for petroleum products. In the 20th Century non-fossil fuel based energy sources such as nuclear fission, hydroelectricity, biomass, solar power and wind turbines were also developed. All of these primary energy sources are often converted into other, secondary

Chapter 1: Introduction

forms of energy that are more convenient for the end user, such as electricity or petrol (gasoline).

Industrialisation has led to improved living standards and economic prosperity, which in turn has led to an increased global population requiring more energy. Fossil fuels are the favoured choice for over 80 % of the world's energy needs because they are relatively abundant, economical to extract and use, and convenient to store and transport¹. However, several issues arise from their use; (i) security of energy supplies; (ii) climate change; and (iii) atmospheric pollution.

1.1.1 Security of energy supplies

Fossil fuels are formed over many millions of years through geological processes. Their reserves are therefore limited and once consumed, cannot be replaced on any realistic time-scale. Although new sources and extraction techniques are pursued², alternative energy sources will have to be in place when all reserves are eventually depleted.

Of more immediate concern is the continued reliance on fossil fuels as the global energy demand continues to increase³. The UK Government predicts that by 2020, 93 % of its primary energy needs will be met through fossil fuels and that they will continue to be predominant for many decades thereafter⁴. As fossil fuel reserves are not evenly distributed across the world, regions with few or no resources are dependent on imports from those that do. As populations grow and developing countries expand their economies and become more energy intensive, these imbalances will increase competition for fossil fuels. Increased competition combined with other factors such as abuses of market power and national/international conflict, threatens to escalate energy prices and the security of supplies.

1.1.2 Climate change

Over the past two centuries, the average global temperature has risen by about 0.8 °C, and it is projected to increase by another 1 – 2 °C over the next 100 years^{5,6}. Global warming may result in changes to the Earth's climate, with potentially drastic physical, ecological and social consequences. The rise in global temperatures has been partially attributed to a concurrent increase in the concentration of various greenhouse gases in the atmosphere, in particular carbon dioxide (CO₂) which has increased by 40 % compared to pre-Industrial Revolution levels⁵. CO₂ is a waste product of fossil fuel combustion and although it is also produced by

several natural processes, the increase in atmospheric CO₂ is a direct consequence of cumulative CO₂ emissions since the Industrial Revolution.

1.1.3 Atmospheric pollution

Many other pollutants aside from CO₂ are emitted by the combustion of fossil fuels. These include nitrous oxides (NO_x), sulphur oxides (SO_x) and various complex hydrocarbons. SO_x are the major source of acid rains which have adverse effects on forests, freshwaters and soils. NO_x reacts with volatile organic compounds in the presence of sunlight to form photochemical smog that surrounds cities with dense traffic on hot and dry days. Developed countries have taken measures to improve their air quality through strict legislation and the development of technologies such as catalytic converters in vehicle exhausts. However the effects of atmospheric pollution are still a major issue in many developing countries where legislation is less robust.

1.1.4 Meeting the challenge

Various governments and international bodies have recognised the need to address the consequences of using fossil fuels. In 1997 more than 100 countries ratified the Kyoto Protocol, indicating their commitment to reducing greenhouse gas emissions⁷. In 2008 the European Union outlined its climate and energy policy, which included the more ambitious 20-20-20 targets^{8,9}. This proposes that by 2020, the EU will reduce greenhouse gas emissions by 20 % of 1990 levels, decrease energy consumption by 20 % by increasing energy efficiency and increase use of renewable energy sources to 20 % of total energy production.

In order to meet such targets, many governments have invested in new renewable energy sources such as solar and wind power, to generate electricity. However the energy produced by these sources is intermittent and so cannot compensate for fluctuating consumer energy demands. As electricity cannot be stored, a non-polluting energy storage medium is required. Furthermore non-polluting alternatives are also required to replace the petroleum-based fuels used in the transportation sector. Hydrogen (H₂) has the potential to fulfil both of these criteria and it has been suggested as an alternative energy vector in a sustainable future energy infrastructure known as the Hydrogen Economy^{10,11}.

1.2 Hydrogen

Hydrogen is the lightest chemical element (atomic weight 1.0079) and has the simplest atomic structure with one proton and one electron. Although it is the most prevalent element in the universe, its abundance on Earth in the elemental form H₂ is small, because of its low density (density 0.0899 g L⁻¹). Instead, it predominantly exists as a component of many different naturally occurring substances such as in hydrocarbons and water.

1.2.1 Hydrogen as an energy carrier

Hydrogen has significant potential as an energy carrier for a number of reasons. Firstly, it can be produced from a wide range of natural resources using a variety of process technologies and primary energy sources, including fossil fuels, nuclear and renewable options¹². This diversity reduces the energy security concerns that accompany the use of hydrocarbons. Once formed, H₂ can be combusted as a fuel to produce heat or used in a fuel cell to produce electricity, with water as the only emission. H₂ is therefore an ideal choice in any future sustainable energy infrastructure as it liberates no pollutants to the atmosphere. Furthermore, if derived from non-fossil primary energy sources or from fossil fuels coupled with CO₂ sequestration, its utilisation would eliminate greenhouse gas emissions.

The development of the fuel cell is of key importance to the deployment of a H₂ infrastructure. Fuel cells are electrochemical devices that convert chemical energy into electrical energy. Unlike batteries, fuel cells continue to work so long as the fuel is externally provided. Fuel cells are particularly attractive to the automotive industry as they are more efficient than ICE's, in addition to being non-polluting¹³. Larger fuel cell units have also been developed for stationary power applications¹⁴.

1.2.2 Hydrogen production

Around 45-50 x 10⁹ kg of hydrogen is produced each year for a wide variety of applications¹⁵. The electrolysis of water was the first industrialised production method, however the reformation of hydrocarbons is the most widely used industrial process today as it is a more economical method. Other methods to produce H₂ can be found in the literature but will not be discussed in this thesis^{12,16}.

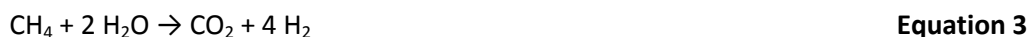
1.2.2.1 Reformation of hydrocarbons

Three primary chemical processes have been developed for the reformation of hydrocarbons; (i) steam reforming; (ii) partial oxidation (POX); and (iii) autothermal reforming (ATR). Methane is the most suitable hydrocarbon feedstock as it is widely available, cheap and has the highest hydrogen-to-carbon ratio amongst all the hydrocarbons. However reformation from oil and coal is also possible¹⁷.

Steam reforming is achieved by reacting methane with steam over a nickel-based catalyst at high temperature (700 – 900 °C) and pressure (3 – 25 bar) (equation 1).



To remove the CO, the syngas (mixture of CO and H₂ gases) is further processed by reaction with steam in the water-gas shift reaction (equation 2). The overall reaction for steam reformation of methane is given by equation 3.



POX is an alternative procedure in which the hydrogen is produced via the partial combustion of methane with oxygen (equation 4).



The POX reaction is exothermic and so does not require an external heat source, in contrast to steam reforming which requires large amounts of expensive superheated steam. This allows POX systems to have more compact reactor designs¹⁸. However compared to steam reforming, the yield of H₂ from POX is lower as only two H₂ molecules are produced per CH₄ molecule. ATR is a combination of both steam reforming (equation 1) and POX (equation 3). The syngas produced by both POX and ATR also requires further processing via the water-gas shift reaction (equation 2).

The final step in all three production methods is the separation of the hydrogen from the carbon dioxide and other impurity gases. This step is important as high purity hydrogen is vital for fuel cell applications^{19,20}. The hydrogen is isolated and purified by pressure swing adsorption in which the CO₂ and other gases are adsorbed onto a suitable material such as activated carbon, in a packed-bed unit at high pressures. The captured CO₂ is then vented into the atmosphere.

Chapter 1: Introduction

Although it is the most economical H₂ production method at present, the reformation of hydrocarbons cannot contribute to the establishment of a sustainable energy infrastructure as it does not relieve the dependency on fossil fuels nor reduce the emission of large amounts of CO₂ to the atmosphere. To reduce the emission of greenhouse gases to zero, the CO₂ could be sequestered underground in geological formations¹⁵. However, the feasibility and proof of permanent CO₂ storage has yet to be determined.

1.2.2.2 Water electrolysis

Water electrolysis is the splitting of water into gaseous H₂ and O₂ by the application of electricity. First observed in 1789²¹, it was developed into an industrialised process in the late 19th and early 20th centuries²². Although it has largely been replaced by hydrocarbon reformation, water electrolysis is still used to produce H₂ at locations where large amounts of surplus electricity are available¹⁵, or to produce O₂ for life support systems in nuclear submarines and the space industry²³. Water electrolysis is preferable to hydrocarbon reforming for sustainable H₂ production because it does not rely on the use of fossil fuels, releases no CO₂ to the atmosphere and delivers high purity H₂, without the need for expensive post-production purification.

Three types of water electrolyser technology have been developed that are differentiated by the type of electrolyte medium; alkaline electrolysers²⁴, PEM electrolysers and solid oxide electrolysers²⁵. Alkaline electrolysers are the most mature technology and comprise two electrodes immersed in a liquid alkaline electrolyte, typically 25-30 % KOH, with a diaphragm placed between the electrodes to separate the two product gases. In contrast PEM electrolysers have a solid polymer electrolyte with the water fed to the anode and cathode. Solid oxide water electrolysers use a solid ceramic electrolyte and operate at high temperatures (700-1000 °C) using superheated steam. A full description of each electrolyser type is not within the scope of this thesis. However as this work focuses on PEM water electrolysers, a detailed description of this technology will be provided in the following sections.

PEM electrolysers offer several advantages to the more established alkaline electrolyser technology. The thin, conductive polymer electrolyte facilitates high current densities and voltage efficiencies^{26,27}, flexible production rates and rapid system response times²⁸, low H₂/O₂ gas crossover²⁹, and inherent greater safety than alkaline electrolytes^{30,31}. The strong structural properties of the membrane also allow for the option of operating at high pressures^{32,33}. This

would negate the need for post-production H₂ compression, which is energy intensive and expensive.

1.3 PEM water electrolysis

1.3.1 General principles

A PEM water electrolysis cell consists of an anode and cathode separated by a proton exchange membrane electrolyte. During operation, water is fed to the anode where it is split into O₂ gas, protons and electrons (equation 5) by the application of a voltage. The protons migrate through the membrane to the cathode where they are combined with electrons to form H₂ gas (equation 6). The overall cell reaction is given by equation 7. A schematic of a PEM water electrolysis cell is shown in figure 1.

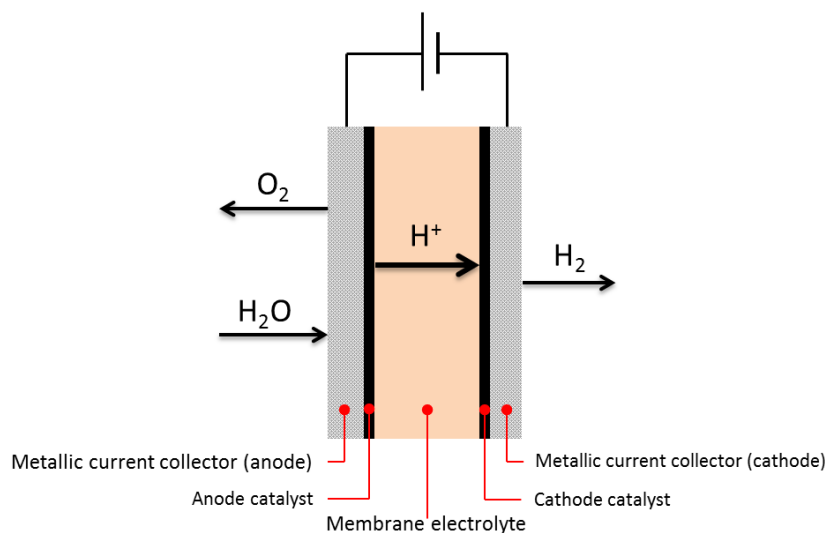


Figure 1 Schematic of a PEM water electrolyser

Chapter 1: Introduction

1.3.2 Thermodynamics and kinetics

The total energy requirement to split water into H₂ and O₂ is determined by the enthalpy change of the reaction, which may be expressed by equation 8

$$\Delta H = \Delta G + T\Delta S \quad \text{Equation 8}$$

where ΔH is the enthalpy change ($\Delta H = 298.15 \text{ kJ mol}^{-1}$), ΔG is the change in the Gibbs free energy ($\Delta G = 237.2 \text{ kJ mol}^{-1}$), T is the temperature and ΔS is the entropy change (16.3 J mol^{-1}). The ΔG term corresponds to the electrical energy requirement, while the $T\Delta S$ term represents the thermal energy associated with the reaction. The electrolysis process is an endothermic ($\Delta H > 0$) and non-spontaneous ($\Delta G > 0$) electrochemical reaction.

The equilibrium cell voltage, E_{cell}^e , represents the lowest required voltage for water electrolysis to occur. It is related to the Gibbs free energy by equation 9

$$E_{cell}^e = \frac{\Delta G}{nF} \quad \text{Equation 9}$$

where n is the number of electrons transferred in the reaction ($n = 2$) and F is the Faraday constant (96485 C mol^{-1}). At standard temperature and pressure (298.15 K and 1 atm), E_{cell}^e for water electrolysis is 1.23 V.

The equilibrium cell voltage represents the minimum electrical energy required for water electrolysis. However, most commercial electrolyzers operate under adiabatic conditions. The cell voltage must therefore also provide the energy corresponding to the entropy change of the reaction. Under these circumstances, the entire enthalpy of the reaction is supplied electrically and the cell voltage is termed the thermoneutral cell voltage, V_{tn} . The thermoneutral voltage is related to ΔH by the expression (equation 10)

$$V_{tn} = \frac{\Delta H}{nF} \quad \text{Equation 10}$$

The thermoneutral voltage for water electrolysis is 1.48 V. This voltage represents the potential at which the reaction is neither endothermic nor exothermic. At voltages $< 1.48 \text{ V}$ the system will absorb heat from its surroundings, whereas at voltages $> 1.48 \text{ V}$ heat will be emitted by the system.

For water electrolysis to operate at a practical rate for H₂ production, a cell voltage in excess of E_{cell}^e and V_{tn} is required in order to overcome the various resistances associated with the cell

reaction. Actual cell voltages, V_{cell} , comprise a combination of both thermodynamic and kinetic contributions as expressed by equation 11

$$V_{cell} = E_{cell}^e + \eta_a + \eta_c + IR \quad \text{Equation 11}$$

where η_a and η_c are the overpotentials associated with the anodic and cathodic reactions, respectively, and IR represents energy dissipation due to ohmic resistances within the electrolysis cell. The ohmic resistance is largely related to the conductivity of the membrane electrolyte, but may also include contributions from the electrodes and electrical connections. The overpotentials represent the electrical energy required to overcome the activation energy barriers for the electrode reactions and drive electron transfer at an acceptable rate. All three terms are inefficiencies which must be minimised in order to increase the efficiency of H_2 production. The magnitude at which the current density, j , varies with the overpotential is determined by the Tafel equation, which for an anodic reaction and cathodic reaction are given by equation 12 and equation 13, respectively

$$\log j = \log j_0 + \frac{\alpha_A n F}{2.3 RT} \eta \quad \text{Equation 12}$$

$$\log j = \log j_0 + \frac{\alpha_C n F}{2.3 RT} \eta \quad \text{Equation 13}$$

where j_0 is the exchange current density and α_A and α_C are the transfer coefficient associated with anodic and cathodic reactions, respectively. The linear relationship between the overpotential and the logarithm of current density is characterised by the Tafel slope $\frac{\alpha n F}{RT}$ and the exchange current density j_0 . Both terms are dependent on the electrode material and are key kinetic parameters that determine specific electrocatalytic activity.

1.3.3 Cell structure and components

The central component of a PEM water electrolyser cell consists of a proton exchange membrane inserted between an anode and a cathode. Electrocatalysts are used at both electrodes to lower the activation energies of the associated electrode reactions, and increase the efficiency of the electrolysis process. An electrocatalyst increases the rate of an electrochemical reaction by changing the nature of the transition state/s or intermediate product/s. PEM water electrolyser electrocatalysts usually comprise a composite of electrocatalytic particles and electrolyte polymer, and are applied to either side of the membrane to form a catalyst coated membrane (CCM) (also termed a membrane electrode assembly (MEA)).

Chapter 1: Introduction

To complete the PEM electrolyser cell, porous metallic meshes or sinters are pressed up against the CCM to provide electrical contact and mechanical support, and to facilitate the delivery and removal of reactants and products. In order to produce H₂ at a desired output with a reasonable voltage, individual cells are linked together to form an electrolyser stack, as shown in figure 2.



Figure 2 Photograph of a PEM water electrolyser stack

A range of commercial PEM electrolyzers are available from a small number of manufacturers worldwide³⁴⁻³⁷. However wide scale adoption of PEM systems is restricted by the high cost of the materials used for the membrane electrolyte and the electrocatalysts.

1.3.3.1 Proton exchange membranes

Perfluorosulfonic acid polymers are the state-of-the-art materials used as membranes in PEM water electrolyzers^{12,38}. The commercial Nafion membrane from *DuPont* is widely used as it has good chemical stability, proton conductivity and mechanical strength^{39,40}. It consists of a polytetrafluoroethylene (PTFE) backbone with sulfonic acid side chains, as shown in figure 3. The C-F bonds of the PTFE backbone provide chemical stability, while the presence of fluorine atoms bonded to the same carbon as the SO₃H groups make the sulfonic acid a superacid, increasing its proton conductivity⁴¹.

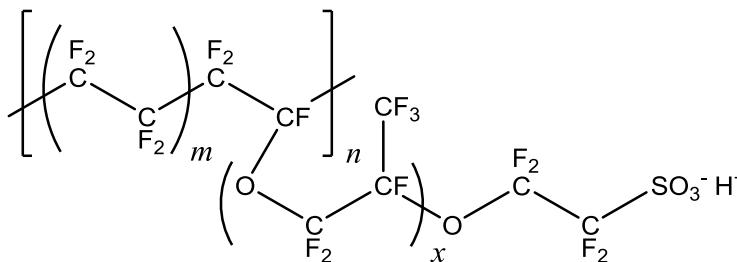


Figure 3 Chemical structure of Nafion®

One drawback to Nafion membranes is that they are limited to operating temperatures below the boiling point of water, as the proton conduction is dependent on the presence of water acting as a bridge between neighbouring sulfonic acid groups. Reinforcing the membrane with inorganic oxides such as TiO₂ and SiO₂, allows it to be used at elevated operating temperatures and pressures^{42,43}. The hygroscopic characteristic of these oxides enhance the water retention properties of the composite membrane, preventing dehydration at high temperatures.

Nafion is also an expensive option, because of the high costs associated with its production and its disposal due to the fluorine content³⁸. A number of low-cost hydrocarbon polymers have been investigated as alternative membrane materials including sulfonated polyether ether ketone (SPEEK)⁴⁴, polyether sulfone (PES)⁴⁴ and sulfonated polyphenyl quinoxaline (SPPQ)⁴⁵. Despite the reported high ionic conductivities and mechanical strength of some of these materials, Nafion remains the standard choice for PEM electrolyser systems due to its superior durability.

1.3.3.2 Cathode electrocatalysts

Platinum electrocatalysts are typically used at the cathode, as Pt is the most catalytically active material for H₂ evolution⁴⁶. It is also stable in the highly acidic conditions. Pt nanoparticles supported on carbon black (Pt/C) are the current state-of-the-art⁴⁷⁻⁴⁹, although Pt black is also widely used^{32,50,51}. The development of Pt/C electrocatalysts has allowed lower precious metal loadings to be achieved. However Pt/C still represents a significant investment cost, especially if some catalyst is lost via the degradation or corrosion of the carbon support⁵². To reduce costs, the use of less expensive noble metals has been studied. Palladium catalysts dispersed on carbon black (Pd/C)⁵³ and on carbon nano-tubes (Pd/CNT)⁵⁴ have shown favourable H₂ evolution activity, with only a slight increase in overpotential compared to Pt/C.

To reduce the cost of the cathode further, the development of non-noble catalysts is also of interest. A range of different materials including cobalt and nickel glyoximes^{32,55}, molybdenum

Chapter 1: Introduction

sulphide nanoparticles⁵⁶ and tungsten carbide⁵⁷ have shown promise as potential cathode catalysts. However the difficulties of incorporating some of these materials into functional electrode structures, in addition to concerns over their long term stability, means that Pt will continue to be the standard material for some time to come.

1.3.3.3 Anode electrocatalysts

The electrochemical evolution of O₂ is a complex reaction that proceeds via several steps. The intermediates formed in each step are of high energy, with high activation energy barriers⁵⁸. Significantly larger overpotentials are therefore required to drive O₂ evolution compared to H₂ evolution, to the extent that the overall cell voltage of a PEM water electrolyser cell is largely determined by the O₂ evolution reaction. Furthermore, the high anodic potentials and acidic conditions limit the choice of electrocatalyst materials to noble metals and their oxides.

1.3.3.3.1 The O₂ evolution reaction

Several reaction mechanisms have been proposed for the O₂ evolution reaction in acidic media^{59, 60}. The rate determining step, and therefore the reaction mechanism, may be elucidated from the value of the Tafel slope found from steady state polarisation measurements. The Tafel slope expresses the rate at which the potential increases with current density. A lower value of Tafel slope therefore represents a more catalytically active material because it allows lower energy consumption for the same production rate. In acidic media, the most active materials for O₂ evolution exhibit Tafel slopes in the range 30 - 40 mV dec⁻¹, for which the following reaction mechanism has been proposed⁵⁹

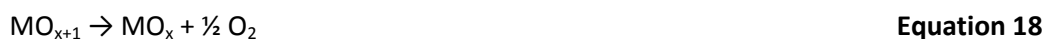


where OH_{ads} and O_{ads} represent a hydroxide molecule and an oxygen atom, respectively, adsorbed on the electrode surface. The steps 15a and 15b represent two alternate paths; the chemical oxide path (equation 15a) and the electrochemical oxide path (equation 15b). The strength of the interaction between the electrode surface and the adsorbed intermediate determines whether one or the other of the steps is dominant⁶¹. If step 15a is rate determining the observed Tafel slope is 30 mV dec⁻¹, whereas it is 40 mV dec⁻¹ if step 15b is rate

determining. In contrast if the first step (equation 14) is rate determining, the Tafel slope is 120 mV dec^{-1} and the material will be a poor catalyst for O_2 evolution. The predicted Tafel slope for the final step (equation 16) is 15 mV dec^{-1} , however a value this low has never been reported.

The O_2 evolution reaction does not occur on a bare metallic surface, but on a metal oxide that is grown electrochemically during the anodic process^{46,62,63}. This is because the strength of metal-oxygen bonds is much greater than the energy of dissociation of the O-O molecule. Anodic oxides such as these are sometimes referred to as hydrous oxides, as the metal ions are partially surrounded by hydroxide molecules in a structure that resembles that of metal ions in solution⁶⁴. Anhydrous metal oxides, wherein the metal oxide is formed non-electrochemically, are also catalytically active. Anhydrous oxides may be prepared by thermally treating a hydrous oxide, via the formation of a thin surface oxide film or by the preparation of metal oxide nanoparticles.

Trasatti proposed that the basis of O_2 evolution electrocatalysis may be understood as a consequence of the anodic oxidation of the metal oxide (MO_x) to an unstable higher oxidation state⁶⁵, as described by equations 17 and 18



with the relaxation of the higher oxidation state back to the lower oxide (equation 18) resulting in the liberation of O_2 . Plots of O_2 evolution overpotential at constant current density for a range of metal oxides, against the enthalpy of transition of the oxide from a lower to higher oxidation state (ΔH_t) was found to produce a volcano-type curve^{65,66}, as shown in figure 4. Materials with intermediate values of ΔH_t , such as RuO_2 ($\Delta H_t = -79.5 \text{ kJ mol}^{-1}$) and IrO_2 ($\Delta H_t = -83.4 \text{ kJ mol}^{-1}$), sit at the apex of this curve. Oxides with high values of ΔH_t such as Fe_2O_3 ($\Delta H_t = -238.5 \text{ kJ mol}^{-1}$) are too easily oxidised and adsorb oxygen intermediates too strongly. Oxides with a low ΔH_t such as PbO_2 ($\Delta H_t = -48.1 \text{ kJ mol}^{-1}$) are difficult to oxidise and adsorb intermediates too weakly.

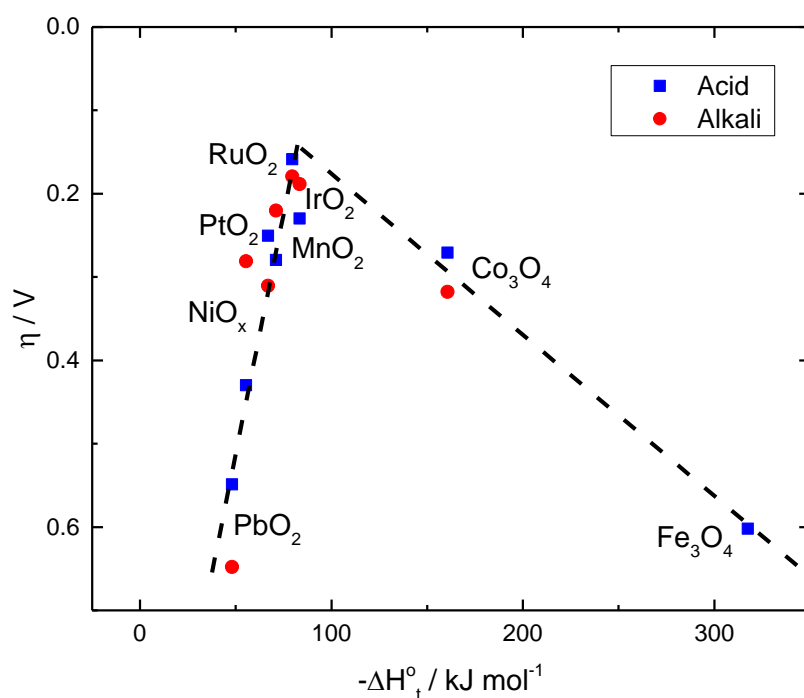


Figure 4 O₂ evolution overpotential (η) on various metal oxides as a function of the enthalpy of lower to higher oxide transition, in acidic (blue squares) and alkali (red circles) ^{63, 66}

The capacity of metal oxide electrocatalysts to undergo several redox transitions has also been correlated to their electrochemical activity⁶⁷. Metal oxides such as RuO₂ and IrO₂ that possess a lower oxide/higher oxide redox couple at a potential close to the O₂ evolution equilibrium potential, are observed to evolve O₂ at relatively low overpotentials. Materials with stable electronic configurations such as PbO₂, or oxides that undergo transitions at very high potentials such as PtO₂, evolve O₂ at higher overpotentials.

1.3.3.3.2 O₂ evolution electrocatalysts

IrO₂ is regarded as the state-of-the-art electrocatalyst for the O₂ evolution reaction in PEM water electrolyzers. Although RuO₂ is more active than IrO₂, it is unsuitable for commercial electrolyzers as it oxidises to the volatile RuO₄ at potentials above 1.8 V and corrodes^{68,69}. Early O₂ evolution electrocatalyst studies focused on metal oxide electrodes developed for the chloro-alkali industry, as active materials for chlorine evolution were found to also be active for O₂ evolution⁶⁶. Known commercially as Dimensionally Stable Anodes (DSA[®]), these electrodes consist of an inert Ti support coated with a thin film of IrO₂ or RuO₂ and are typically prepared through the thermal decomposition of metal chloride precursor salts⁷⁰⁻⁷². However

DSA[®] electrodes are unsuitable for PEM water electrolyzers as they cannot be fully integrated with the polymer electrolyte, resulting in a poor contact between the catalyst layer and the membrane⁷³⁻⁷⁵. Passivation of the Ti supports, via the formation of titanium oxide (TiO₂), is also a major issue that leads to the detachment and deactivation of the catalyst layer^{76,77}. The deposition of electrocatalyst nanoparticles directly onto the membrane is the preferred electrode/electrocatalyst structure, as it ensures a good contact at the catalyst/membrane interface and minimises ohmic losses. Metal oxide powders may be prepared by a number of routes such as the Adams fusion⁷⁸⁻⁸⁰, modified polyol^{81,82}, hydrolysis^{83,84}, sol-gel^{85,86} and sulphite-complex methods⁸⁷.

The high cost and low natural abundance of IrO₂ is a significant obstacle to the commercial implementation of PEM electrolyser technology. Many investigators have attempted to decrease the investment cost of the anode electrocatalyst by diluting the Ir content with other metal oxides. Mixing two or more metal oxides may also result in changes to the electrochemical properties of the catalyst, via synergic effects between the active and inactive components of the mixture. For synergic effects to occur, the different components must be intimately mixed at an atomic scale so as to form common electronic band structures⁸⁴. However, mixing two or more oxides may result in the surface segregation of one of the components⁸⁸. The preparation method of the catalyst has been suggested as an important factor in producing intimately mixed oxides⁸⁹.

Mixtures of IrO₂ and RuO₂ have been widely studied as Ru is less expensive than Ir⁹⁰⁻⁹³. Additions of Ru to Ir have been shown to improve that activity of the composite material with respect to pure IrO₂, and the stability compared to RuO₂. It was suggested that the RuO₂ sites are stabilised by the formation of a common *d*-band between IrO₂ and RuO₂, which suppresses the oxidation of RuO₂ to RuO₄⁹⁴. IrO₂ has also been mixed with other transition metals that are inactive towards the O₂ evolution reaction but are less expensive than RuO₂ and show good stability under O₂ evolution, such as tin oxide (SnO₂)^{82,95,96} and tantalum oxide (Ta₂O₅)^{97,98}. Various ternary oxide combinations have also been reported including SnO₂-IrO₂-Ta₂O₅⁹⁹, Ir_xRu_yTa_zO₂¹⁰⁰ and (Sn_{1-2x}Ru_xIr_x)O₂⁸⁰.

An alternative method to reduce the precious metal content of O₂ evolution electrocatalysts is to deposit the Ir/IrO₂ onto a supporting material. Catalyst supports provide a surface for the dispersal of electrocatalyst particles, facilitating high active surface areas and reduced catalyst loadings. The ideal candidate support material for an O₂ evolution electrocatalyst must be; (i) electronically conductive; (ii) electrochemically stable at high anodic potentials; (iii) chemically

Chapter 1: Introduction

stable in highly oxidising and acidic conditions. Carbon, the support material of choice for H₂ evolution reaction electrocatalysts, is unsuitable for O₂ evolution as it corrodes at the high anodic potentials employed¹⁰¹. Instead, a number of metal carbides and metal oxides have been suggested as potential supports including tantalum carbide (TaC)¹⁰², titanium carbide (TiC)¹⁰³, SnO₂¹⁰⁴, antimony tin oxide (SnO₂/Sb₂O₅ or ATO)^{105,106}, TiO₂¹⁰⁷ and titanium sub-oxides (Ti_nO_{2n-1})^{108,109}. Research in the closely related field of O₂ reduction reaction electrocatalysts for PEM fuel cells has implied that tungsten carbide (WC)¹¹⁰, tungsten oxide (WO_x)¹¹⁰ and indium tin oxide (In₂O₃/SnO₂ or ITO)¹¹¹ may also be suitable.

Despite the potential lower cost of mixed oxides or supported electrocatalysts, IrO₂ remains the preferred anode catalyst for commercial PEM water electrolyzers.

1.4 Aims and objectives

This chapter has provided an introduction to the science of PEM water electrolysis, the O₂ evolution reaction and O₂ evolution electrocatalysts. It has highlighted that the current commercial viability of PEM electrolyzers is significantly inhibited by the energy losses that occur with anodic O₂ evolution, in addition to the high cost of the IrO₂ electrocatalysts used for this reaction. To lower the cost of PEM electrolyser manufacture and operation, O₂ evolution electrocatalysts must therefore reduce the precious metal content without compromising, and ideally increasing, the catalytic activity and stability.

This work focusses on the investigation and characterisation of Ir-based nanoparticle electrocatalysts, with the overall aim to aid the development of O₂ evolution electrocatalysts with reduced Ir contents compared to the current state-of-the-art, IrO₂. It is intended that this will be achieved by focussing on two areas of study that have shown promise in the literature as alternative catalyst materials. These are (i) the binary metal oxide Ir_xRu_yO₂ and (ii) supported IrO₂/X or Ir/X (where X represents the support material) compounds.

Chapter 3 will focus on the Ir_xRu_yO₂ electrocatalyst with the aim to investigate the interaction between the two metal constituents under operational conditions (i.e. O₂ evolution), in order to understand how the composition affects the activity and the stability of the catalyst. This will be achieved through the preparation and characterisation, both physiochemical and electrochemical, of catalysts with the nominal compositions: IrO₂, Ir_{0.75}Ru_{0.25}O₂, Ir_{0.50}Ru_{0.50}O₂, Ir_{0.25}Ru_{0.75}O₂ and RuO₂. The interaction between the Ir and Ru under O₂ evolution conditions

will be probed via the use of in-situ X-ray absorbance spectroscopy. These experiments will allow for the characterisation of both metal's oxidation state under potential control.

Chapter 4 will investigate the feasibility of supported Ir electrocatalysts for PEM water electrolyzers. Utilising ITO as the support material, the effect of Ir loading on the support will be examined by preparing catalysts with the nominal Ir loadings 40, 20, 10 and 5 wt. %. The effect of heat treatment on the performance of the electrocatalysts will also be explored.

The theoretical and experimental details of the various synthetic and analytical techniques used throughout this thesis, will be introduced in **Chapter 2**. The final chapter (**Chapter 5**) will present the conclusions reached over the course of the thesis and set out recommendations for future work.

1.5 References

- (1) International Energy Agency *IEA Key World Energy Statistics*, 2012.
- (2) Andrews, I. J. *The Carboniferous Bowland Shale Gas Study: Geology and Resource Estimation*, British Geology Survey for the Department of Energy and Climate Change, 2013.
- (3) International Energy Agency *World Energy Outlook 2011*, 2011.
- (4) Department of Trade and Industry *Meeting the Energy Challenge: A White Paper on Energy*, UK Government, 2007.
- (5) International Panel on Climate Control *Climate Change 2013; The Physical Science Basis*, 2013.
- (6) Meinshausen, M.; Meinshausen, N.; Hare, W.; Raper, S. C. B.; Frieler, K.; Knutti, R.; Frame, D. J.; Allen, M. R. *Nature* **2009**, *458*, 1158.
- (7) Conference of the Parties at the Convention *Kyoto Protocol to the United Nations Framework Convention on Climate Change*, 1997.
- (8) Commission of the European Communities *Communication from the Commission to the European Parliament, the Council, the European Economic and Social Committee and the Committee of the Regions; 20 20 by 2020 Europe's Climate Change Opportunity*, 2008.
- (9) European Parliament and the Council *Decision No 406/2009/EC of the European Parliament and of the Council of 23 April 2009; on the effort of Member States to reduce their greenhouse gas emissions to meet the Community's greenhouse gas emission reduction commitments up to 2020*, 2009.
- (10) Bockris, J. O. M. *Science* **1972**, *176*, 1323.
- (11) Bockris, J. O. M. *International Journal of Hydrogen Energy* **2013**, *38*, 2579.

Chapter 1: Introduction

- (12) Holladay, J. D.; Hu, J.; King, D. L.; Wang, Y. *Catalysis Today* **2009**, *139*, 244.
- (13) Ahluwalia, R. K.; Wang, X. *Journal of Power Sources* **2008**, *177*, 167.
- (14) Carrette, L.; Friedrich, K. A.; Stimming, U. *Fuel Cells* **2001**, *1*, 5.
- (15) Rand, D. A. J.; Dell, R. M. *Hydrogen Energy; Challenges and Prospects*; Royal Society of Chemistry: Cambridge, UK, 2008.
- (16) Turner, J.; Sverdrup, G.; Mann, M. K.; Maness, P.-C.; Kroposki, B.; Ghirardi, M.; Evans, R. J.; Blake, D. *International Journal of Energy Research* **2008**, *32*, 379.
- (17) Navarro, R. M.; Peña, M. A.; Fierro, J. L. G. *Chemical Reviews* **2007**, *107*, 3952.
- (18) International Energy Agency *Hydrogen Production and Storage: R&D Priorities and Gaps*, 2006.
- (19) Cheng, X.; Shi, Z.; Glass, N.; Zhang, L.; Zhang, J.; Song, D.; Liu, Z.-S.; Wang, H.; Shen, J. *Journal of Power Sources* **2007**, *165*, 739.
- (20) Alayoglu, S.; Nilekar, A. U.; Mavrikakis, M.; Eichhorn, B. *Nature Materials* **2008**, *7*, 333.
- (21) Pearson, G. *Philosophical Transactions of the Royal Society of London* **1797**, *87*, 142.
- (22) LeRoy, R. L. *International Journal of Hydrogen Energy* **1983**, *8*, 401.
- (23) Lu, P. W. T.; Srinivasan, S. *Journal of Applied Electrochemistry* **1979**, *9*, 269.
- (24) Zeng, K.; Zhang, D. *Progress in Energy and Combustion Science* **2010**, *36*, 307.
- (25) Laguna-Bercero, M. A. *Journal of Power Sources* **2012**, *203*, 4.
- (26) Ayers, K. E.; Anderson, E. B.; Capuano, C.; Carter, B.; Dalton, L.; Hanlon, G.; Manco, J.; Niedzwiecki, M. *ECS Transactions* **2010**, *33*, 3.
- (27) Slade, S.; Campbell, S. A.; Ralph, T. R.; Walsh, F. C. *Journal of The Electrochemical Society* **2002**, *149*, A1556.
- (28) Clarke, R. E.; Giddey, S.; Ciacchi, F. T.; Badwal, S. P. S.; Paul, B.; Andrews, J. *International Journal of Hydrogen Energy* **2009**, *34*, 2531.
- (29) Barbir, F. *Solar Energy* **2005**, *78*, 661.
- (30) Millet, P.; Ranjbari, A.; de Guglielmo, F.; Grigoriev, S. A.; Auprêtre, F. *International Journal of Hydrogen Energy* **2012**, *37*, 17478.
- (31) Grigoriev, S. A.; Millet, P.; Korobtsev, S. V.; Porembskiy, V. I.; Pepic, M.; Etievant, C.; Puyenchet, C.; Fateev, V. N. *International Journal of Hydrogen Energy* **2009**, *34*, 5986.
- (32) Millet, P.; Ngameni, R.; Grigoriev, S. A.; Mbemba, N.; Brisset, F.; Ranjbari, A.; Etiévant, C. *International Journal of Hydrogen Energy* **2010**, *35*, 5043.
- (33) Millet, P.; Alleau, T.; Durand, R. *Journal of Applied Electrochemistry* **1993**, *23*, 322.

- (34) ITM Power PLC, <http://www.itm-power.com/>, Accessed 05/01/2015.
- (35) Hydrogenics Corporation, <http://www.hydrogenics.com/home>, Accessed 05/01/2015.
- (36) Proton OnSite, <http://www.protononsite.com/>, Accessed 05/01/2015.
- (37) H2 Logic <http://www.h2logic.com/com/fuelcellpower.asp>, Accessed 05/01/2015.
- (38) Goñi-Urtiaga, A.; Presvytes, D.; Scott, K. *International Journal of Hydrogen Energy* **2012**, *37*, 3358.
- (39) Ito, H.; Maeda, T.; Nakano, A.; Takenaka, H. *International Journal of Hydrogen Energy* **2011**, *36*, 10527.
- (40) Mauritz, K. A.; Moore, R. B. *Chemical Reviews* **2004**, *104*, 4535.
- (41) Costamagna, P.; Srinivasan, S. *Journal of Power Sources* **2001**, *102*, 242.
- (42) Baglio, V.; Ornelas, R.; Matteucci, F.; Martina, F.; Ciccarella, G.; Zama, I.; Arriaga, L. G.; Antonucci, V.; Aricò, A. S. *Fuel Cells* **2009**, *9*, 247.
- (43) Antonucci, V.; Di Blasi, A.; Baglio, V.; Ornelas, R.; Matteucci, F.; Ledesma-Garcia, J.; Arriaga, L. G.; Aricò, A. S. *Electrochimica Acta* **2008**, *53*, 7350.
- (44) Linkous, C. A.; Anderson, H. R.; Kopitzke, R. W.; Nelson, G. L. *International Journal of Hydrogen Energy* **1998**, *23*, 525.
- (45) Wei, G.; Xu, L.; Huang, C.; Wang, Y. *International Journal of Hydrogen Energy* **2010**, *35*, 7778.
- (46) Miles, M. H.; Thomason, M. A. *Journal of The Electrochemical Society* **1976**, *123*, 1459.
- (47) Su, H.; Linkov, V.; Bladergroen, B. J. *International Journal of Hydrogen Energy* **2013**, *38*, 9601.
- (48) Millet, P.; Mbemba, N.; Grigoriev, S. A.; Fateev, V. N.; Aukauloo, A.; Etiévant, C. *International Journal of Hydrogen Energy* **2011**, *36*, 4134.
- (49) Siracusano, S.; Baglio, V.; Briguglio, N.; Brunaccini, G.; Di Blasi, A.; Stassi, A.; Ornelas, R.; Trifoni, E.; Antonucci, V.; Aricò, A. S. *International Journal of Hydrogen Energy* **2012**, *37*, 1939.
- (50) Hwang, C. M.; Ishida, M.; Ito, H.; Maeda, T.; Nakano, A.; Kato, A.; Yoshida, T. *Journal of Power Sources* **2012**, *202*, 108.
- (51) Yamaguchi, M.; Okisawa, K.; Nakanori, T. In *Energy Conversion Engineering Conference, 1997. IECEC-97., Proceedings of the 32nd Intersociety 1997*; Vol. 3, p 1958.
- (52) Kangasniemi, K. H.; Condit, D. A.; Jarvi, T. D. *Journal of The Electrochemical Society* **2004**, *151*, E125.
- (53) Grigoriev, S. A.; Millet, P.; Fateev, V. N. *Journal of Power Sources* **2008**, *177*, 281.

Chapter 1: Introduction

- (54) Grigoriev, S. A.; Mamat, M. S.; Dzhus, K. A.; Walker, G. S.; Millet, P. *International Journal of Hydrogen Energy* **2011**, *36*, 4143.
- (55) Pantani, O.; Anxolabéhère-Mallart, E.; Aukauloo, A.; Millet, P. *Electrochemistry Communications* **2007**, *9*, 54.
- (56) Hinnemann, B.; Moses, P. G.; Bonde, J.; Jørgensen, K. P.; Nielsen, J. H.; Horch, S.; Chorkendorff, I.; Nørskov, J. K. *Journal of the American Chemical Society* **2005**, *127*, 5308.
- (57) Nikiforov, A. V.; Petrushina, I. M.; Christensen, E.; Alexeev, N. V.; Samokhin, A. V.; Bjerrum, N. J. *International Journal of Hydrogen Energy* **2012**, *37*, 18591.
- (58) Guerrini, E.; Trasatti, S. In *Catalysis for Sustainable Energy Production*; 1 ed.; Barbaro, P., Bianchini, C., Eds.; Wiley-VCH: Weinheim, 2009, p 235.
- (59) Bockris, J. O. M. *The Journal of Chemical Physics* **1956**, *24*, 817.
- (60) Krasil'shchikov, A. I. *Russian Journal of Physical Chemistry* **1963**, *37*, 273.
- (61) Faria, L. A.; Boodts, J. F. C.; Trasatti, S. *Journal of Applied Electrochemistry* **1996**, *26*, 1195.
- (62) Tseung, A. C. C.; Jasem, S. *Electrochimica Acta* **1977**, *22*, 31.
- (63) Burke, L. D.; McCarthy, F.; O'Meara, T. O. *Journal of the Chemical Society, Faraday Transactions 1: Physical Chemistry in Condensed Phases* **1972**, *68*, 1086.
- (64) Burke, L. D.; O'Sullivan, E. J. M. *Journal of Electroanalytical Chemistry and Interfacial Electrochemistry* **1981**, *117*, 155.
- (65) Trasatti, S. *Journal of Electroanalytical Chemistry* **1980**, *111*, 125.
- (66) Trasatti, S. *Electrochimica Acta* **1984**, *29*, 1503.
- (67) Rasiyah, P.; Tseung, A. C. C. *Journal of The Electrochemical Society* **1984**, *131*, 803.
- (68) Hine, F.; Yasuda, M.; Noda, T.; Yoshida, T.; Okuda, J. *Journal of The Electrochemical Society* **1979**, *126*, 1439.
- (69) Lodi, G.; Sivieri, E.; Battisti, A.; Trasatti, S. *Journal of Applied Electrochemistry* **1978**, *8*, 135.
- (70) Galizzioli, D.; Tantardini, F.; Trasatti, S. *Journal of Applied Electrochemistry* **1974**, *4*, 57.
- (71) De Pauli, C. P.; Trasatti, S. *Journal of Electroanalytical Chemistry* **2002**, *538-539*, 145.
- (72) Beer, H. In *Improvements in or relating to Electrodes for Electrolysis*; Patent, U., Ed.; UK UK 1969; Vol. GB1147442.
- (73) Song, S.; Zhang, H.; Ma, X.; Shao, Z.; Baker, R. T.; Yi, B. *International Journal of Hydrogen Energy* **2008**, *33*, 4955.

- (74) Marshall, A.; Børresen, B.; Hagen, G.; Sunde, S.; Tsyppkin, M.; Tunold, R. *Russian Journal of Electrochemistry* **2006**, *42*, 1134.
- (75) Xu, W.; Scott, K.; Basu, S. *Journal of Power Sources* **2011**, *196*, 8918.
- (76) Xu, L. K.; Scantlebury, J. D. *Corrosion Science* **2003**, *45*, 2729.
- (77) Chen, G.; Chen, X.; Yue, P. L. *The Journal of Physical Chemistry B* **2002**, *106*, 4364.
- (78) Adams, R.; Shriener, R. L. *Journal of the American Chemical Society* **1923**, *45*, 2171.
- (79) Rasten, E.; Hagen, G.; Tunold, R. *Electrochimica Acta* **2003**, *48*, 3945.
- (80) Hutchings, R.; Müller, K.; Kötz, R.; Stucki, S. *Journal of Materials Science* **1984**, *19*, 3987.
- (81) Marshall, A.; Børresen, B.; Hagen, G.; Tsyppkin, M.; Tunold, R. *Materials Chemistry and Physics* **2005**, *94*, 226.
- (82) Marshall, A.; Børresen, B.; Hagen, G.; Tsyppkin, M.; Tunold, R. *Electrochimica Acta* **2006**, *51*, 3161.
- (83) Ioroi, T.; Kitazawa, N.; Yasuda, K.; Yamamoto, Y.; Takenaka, H. *Journal of The Electrochemical Society* **2000**, *147*, 2018.
- (84) Owe, L.-E.; Tsyppkin, M.; Wallwork, K. S.; Haverkamp, R. G.; Sunde, S. *Electrochimica Acta* **2012**, *70*, 158.
- (85) Guglielmi, M.; Colombo, P.; Rigato, V.; Battaglin, G.; Boscolo-Boscoletto, A.; DeBattisti, A. *Journal of The Electrochemical Society* **1992**, *139*, 1655.
- (86) Kameyama, K.; Shohji, S.; Onoue, S.; Nishimura, K.; Yahikozawa, K.; Takasu, Y. *Journal of The Electrochemical Society* **1993**, *140*, 1034.
- (87) Siracusano, S.; Baglio, V.; Stassi, A.; Ornelas, R.; Antonucci, V.; Aricò, A. S. *International Journal of Hydrogen Energy* **2011**, *36*, 7822.
- (88) Angelinetta, C.; Trasatti, S.; Atanososka, L. D.; Atanasoski, R. T. *Journal of Electroanalytical Chemistry and Interfacial Electrochemistry* **1986**, *214*, 535.
- (89) Trasatti, S. *Electrochimica Acta* **1991**, *36*, 225.
- (90) Wen, T.-C.; Hu, C.-C. *Journal of The Electrochemical Society* **1992**, *139*, 2158.
- (91) Cheng, J.; Zhang, H.; Chen, G.; Zhang, Y. *Electrochimica Acta* **2009**, *54*, 6250.
- (92) Baglio, V.; Blasi, A. D.; Denaro, T.; Antonucci, V.; Aricò, A. S.; Ornelas, R.; Matteucci, F.; Alonso, G.; Morales, L.; Orozco, G.; Arriaga, L. G. *Journal of New Materials for Electrochemical Systems* **2008**, *11*, 105.
- (93) Lee, Y.; Suntivich, J.; May, K. J.; Perry, E. E.; Shao-Horn, Y. *The Journal of Physical Chemistry Letters* **2012**, *3*, 399.
- (94) Kötz, R.; Stucki, S. *Electrochimica Acta* **1986**, *31*, 1311.

Chapter 1: Introduction

- (95) Li, G.; Yu, H.; Wang, X.; Sun, S.; Li, Y.; Shao, Z.; Yi, B. *Physical Chemistry Chemical Physics* **2013**, *15*, 2858.
- (96) Ardizzone, S.; Bianchi, C.; Borgese, L.; Cappelletti, G.; Locatelli, C.; Minguzzi, A.; Rondinini, S.; Vertova, A.; Ricci, P.; Cannas, C.; Musinu, A. *Journal of Applied Electrochemistry* **2009**, *39*, 2093.
- (97) Di Blasi, A.; D'Urso, C.; Baglio, V.; Antonucci, V.; Arico', A.; Ornelas, R.; Matteucci, F.; Orozco, G.; Beltran, D.; Meas, Y.; Arriaga, L. *Journal of Applied Electrochemistry* **2009**, *39*, 191.
- (98) Felix, C.; Maiyalagan, T.; Pasupathi, S.; Bladergroen, B.; Linkov, V. *International Journal of Electrochemical Science* **2012**, *7*, 12064.
- (99) Ardizzone, S.; Bianchi, C. L.; Cappelletti, G.; Ionita, M.; Minguzzi, A.; Rondinini, S.; Vertova, A. *Journal of Electroanalytical Chemistry* **2006**, *589*, 160.
- (100) Marshall, A. T.; Sunde, S.; Tsympkin, M.; Tunold, R. *International Journal of Hydrogen Energy* **2007**, *32*, 2320.
- (101) Pettersson, J.; Ramsey, B.; Harrison, D. *Journal of Power Sources* **2006**, *157*, 28.
- (102) Polonský, J.; Petrushina, I. M.; Christensen, E.; Bouzek, K.; Prag, C. B.; Andersen, J. E. T.; Bjerrum, N. J. *International Journal of Hydrogen Energy* **2012**, *37*, 2173.
- (103) Ma, L.; Sui, S.; Zhai, Y. *Journal of Power Sources* **2008**, *177*, 470.
- (104) Xu, J.; Liu, G.; Li, J.; Wang, X. *Electrochimica Acta* **2012**, *59*, 105.
- (105) Marshall, A. T.; Haverkamp, R. G. *Electrochimica Acta* **2010**, *55*, 1978.
- (106) Thomassen, M. S.; Mokkelbost, T.; Sheridan, E.; Lind, A. *ECS Transactions* **2011**, *35*, 271.
- (107) Mazúr, P.; Polonský, J.; Paidar, M.; Bouzek, K. *International Journal of Hydrogen Energy* **2012**, *37*, 12081.
- (108) Siracusano, S.; Baglio, V.; D'Urso, C.; Antonucci, V.; Aricò, A. S. *Electrochimica Acta* **2009**, *54*, 6292.
- (109) Chen, G.; Bare, S. R.; Mallouk, T. E. *Journal of The Electrochemical Society* **2002**, *149*, A1092.
- (110) Antolini, E.; Gonzalez, E. R. *Solid State Ionics* **2009**, *180*, 746.
- (111) Chhina, H.; Campbell, S.; Kesler, O. *Journal of Power Sources* **2006**, *161*, 893.

2. Experimental methods and techniques

The theoretical and practical aspects of the experimental work carried out in this project are detailed in this chapter. This includes descriptions of the physicochemical and electrochemical characterisation techniques. The procedure of preparation of the electrocatalysts will be described in **Chapters 3 and 4**.

2.1 Reagents and materials

The reagents and materials used in this study, along with the suppliers, are listed below in table 1.

Chapter 2: Experimental methods and techniques

Table 1 List of the reagents and materials used along with suppliers

Reagent (purity/grade)	Supplier
Dihydrogen hexachloroiridate hydrate (38 – 42 % Ir) ($\text{H}_2\text{IrCl}_6 \cdot x\text{H}_2\text{O}$)	Alfa Aesar
Dispex® N40 dispersing agent	BASF
Ethanol	Fisher
Formaldehyde (37 % in H_2O , contains 10-15 % methanol as stabiliser)	Fisher
Indium tin oxide (nanopowder, < 50 nm particle size) (ITO)	Sigma Aldrich
Isopropanol (IPA)	Fisher
Nafion 115 membrane (thickness 0.005 inch)	Sigma Aldrich
Nafion perfluorinated resin solution (5 wt. % in mixture of lower aliphatic alcohols and water, contains 45 % water)	Sigma Aldrich
Nafion® perfluorinated resin solution (5 wt. % in lower aliphatic alcohols and water, contains 15-20 % water)	Sigma Aldrich
Nitrogen (oxygen free)	BOC
Ruthenium (III) chloride hydrate (38 % Ru min) ($\text{RuCl}_3 \cdot x\text{H}_2\text{O}$)	Alfa Aesar
Sodium hydrogen carbonate	Fisher
Sodium nitrate (NaNO_3)	Sigma Aldrich
Sulfuric acid (> 95 %)	Fisher
Purified water (18.2 M Ω cm)	Pure1te system
Purified water for PEM cell testing (18.2 M Ω cm)	Merck Millipore system

2.2 Electrochemical techniques

Electrochemical methods are imperative to determine the performance of electrocatalysts. Techniques such as cyclic voltammetry may be used to probe the processes that occur at the catalyst surface, whilst the catalytic activity is measured by steady state polarization.

2.2.1 Cyclic voltammetry

Cyclic voltammetry is a potential sweep technique used to characterise the redox processes that occur at the electrode surface. It may also be used to give an indication of the electrochemical active area and capacitance of an electrode. A cyclic voltammetry experiment proceeds by sweeping the potential (E) of the working electrode from an initial limit (E_1) to a second limit (E_2) at a constant sweep rate. Upon reaching the second limit the potential sweep is reversed and swept back to the initial value. A typical waveform for this process is presented in figure 1. The current is recorded as a function of the potential and plotted as a voltammogram.

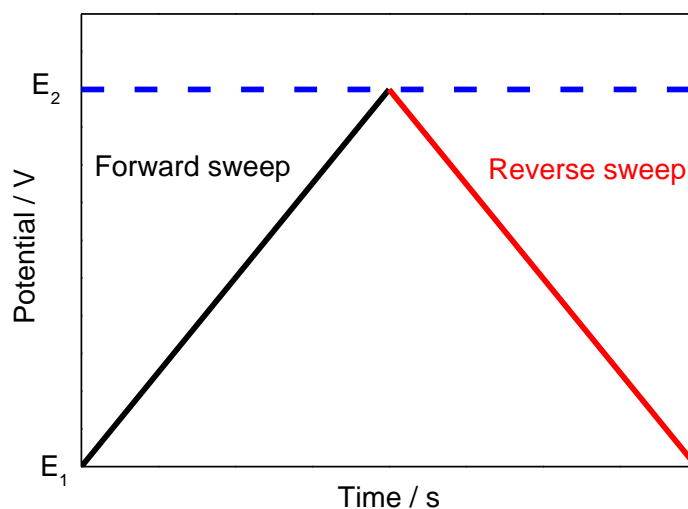


Figure 1 Typical applied potential waveform of a cyclic voltammetry experiment

Noble metal oxides such as IrO_2 and RuO_2 have characteristic cyclic voltammograms in acid, as shown by the voltammogram of an IrO_2 electrode in figure 2. The current response of the voltammetry is a combination of the capacitance of the electric double layer, in addition to Faradaic current due to electron transfer.

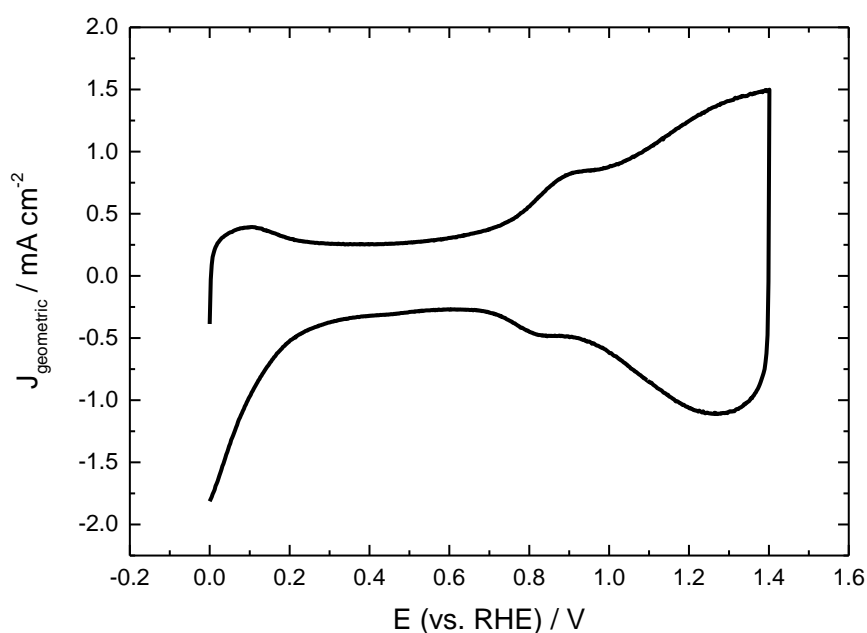
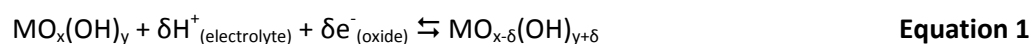


Figure 2 Cyclic voltammetry of an IrO₂ nanoparticulate catalyst (catalyst loading = 0.5 mg cm⁻²) deposited on a glassy carbon electrode (surface area = 0.1963 cm²) at a scan rate of 50 mV s⁻¹ in 0.5 M H₂SO₄.

The wide peaks that occur in the potential region between about 0.6 and 1.4 V vs. RHE of figure 2 are attributed to solid state redox transitions that involve the exchange of protons between the electrolyte and metal oxide surface sites^{1,2}. These transitions are described as a pseudocapacitive process, as the adsorbed species essentially store charge on the electrode surface. However in contrast to the double layer capacitance, the pseudocapacitance is a Faradaic process as electrons cross the double layer interface. A general scheme for these solid state redox transitions is given by equation 1²



where M represents an Ir or Ru atom. The large width of these peaks reflects the energetic heterogeneity of the surface oxide sites. The large cathodic peak that starts at about -0.20 V and continues to 0.0 V is the adsorption of hydrogen that occurs prior to the onset of H₂ evolution at potentials negative to 0.0 V vs. RHE.

The electrochemically active surface area of RuO₂ and IrO₂ electrodes can be characterised by measuring the voltammetric charge (Q*) in the potential region 0.4 to 1.4 V vs. RHE³. This is based on the assumption that Q* is a measure of the number of sites exchanging protons with

the solution⁴, as represented by equation 1, and that these sites are also the same sites that are involved in the catalytic evolution of O₂. However the conversion of Q* to surface area is not possible as the exact nature of the surface reactions is unknown. The magnitude of Q* has been shown to decrease as the potential scan rate increases³. The dependence of Q* on the scan rate is explained by the slow diffusion of protons through various regions of the oxide electrode structure⁵. At low scan rates, there is sufficient time for the protons to penetrate the surface and diffuse through pores, cracks and grain boundaries of the oxide to reach “inner”, less accessible sites. This results in an increase in the measured charge. At higher scan rates, less Q* is measured as there is less time for the protons to diffuse and only the “outer”, more accessible sites are active.

Ardizzone et al. developed a method to linearize Q* as a function of $v^{1/2}$ so as to extrapolate values of Q* to $v = 0$ and $v = \infty$ and determine the inner, outer and total charge⁵. At high scan rates, Q* is proportional to the inverse square root of the scan rate (equation 2)

$$Q^* = Q_o^* + A\left(\frac{1}{\sqrt{v}}\right) \quad \text{Equation 2}$$

where Q*_o is the outer surface charge, A is a constant and v is the scan rate. At low scan rates the inverse of the voltammetric charge is proportional to the square root of the scan rate (equation 3)

$$\frac{1}{Q^*(v)} = \frac{1}{Q_T^*} + B\sqrt{v} \quad \text{Equation 3}$$

where Q*_T is the total surface charge and B is a constant. The total charge can be determined by plotting Q* vs. $v^{-1/2}$ and extrapolating to $v = \infty$, while the outer charge is determined by plotting 1/Q* vs. $v^{-1/2}$ and extrapolating to $v = 0$. The inner charge can then be calculated by subtracting the outer charge from the total charge.

2.2.2 Steady state polarization

The activity of an electrocatalyst may be assessed by examining how the steady state current density for the catalysed reaction under study, varies with the potential. To ensure that the reaction is operating under steady state conditions, polarization curves are obtained by either (i) stepping the potential manually from point-to-point and measuring the current density (j , mA cm⁻²) after a defined period (e.g. 60 s), or (ii) voltammetry using a very slow potential sweep rate (i.e. 1 – 10 mV s⁻¹). In this work the former method has been used to measure

Chapter 2: Experimental methods and techniques

polarisation curves of PEM electrolyser cells, whilst the latter method has been used to characterise catalyst samples deposited on glassy carbon electrodes in 0.5 M H₂SO₄.

The catalytic performance can be evaluated by plotting j vs. E and comparing samples at a given potential or current density. Determination of the reaction mechanism is also possible by analysing plots of $\log(j)$ vs. E , which will have a linear range where the data follows the Tafel equation (Chapter 1, equations 12 and 13). Comparison of the experimental Tafel slope with those calculated for theoretical reaction mechanisms is used to differentiate between plausible mechanisms.

2.2.3 Electrochemistry experimental details

2.2.3.1 Thin film rotating disk electrode half-cell

Initial electrochemical characterisation was carried out with catalyst samples prepared as thin film layers on glassy carbon rotating disk electrodes (RDE). Prior to applying catalyst, the RDE was polished to a mirror finish on *Buehler* microcloths using alumina slurries of 1.0 μm and then 0.05 μm particle size.

The thin film catalyst layers were made by depositing catalyst inks (10.0 μL) onto the RDE (area 0.1963 cm^2) tip and drying under a heat lamp for 5 min. Catalyst inks were prepared by mixing catalyst powder (10 mg), water (500 μL), ethanol (500 μL) and Nafion solution (34.3 μL) for 30 min in an ultrasonic bath, followed by 1 min with a Fisher Powergen 125 Homogenizer. The Nafion content was set to 15 wt. % with respect to the mass of catalyst when dry. The volume of ink deposited on the RDE was set so as to give a catalyst loading of 0.50 mg cm^{-2} , as described by equation 4

$$\text{Volume ink } (\mu\text{L}) = \frac{\text{Catalyst loading } (\text{mg cm}^{-2}) \times \text{Electrode area } (\text{cm}^2)}{\text{Catalyst concentration of ink } (\text{mg } \mu\text{L}^{-1})} \quad \text{Equation 4}$$

The thin-film RDE was attached to a Pine AFMSRX rotator and mounted into an electrochemical beaker cell (volume 100 ml) filled with N₂ purged 0.5 M H₂SO₄, as depicted in figure 3. High surface area Pt gauze was used as the counter electrode and a mercury mercurous sulfate (MMS) electrode (calibrated prior to measurements to the reversible hydrogen electrode (RHE)) as the reference electrode. Electrochemical measurements were carried out at room temperature using an Autolab PGSTAT101 potentiostat or an Autolab PGSTAT 30 potentiostat using the NOVA and GPES software packages.

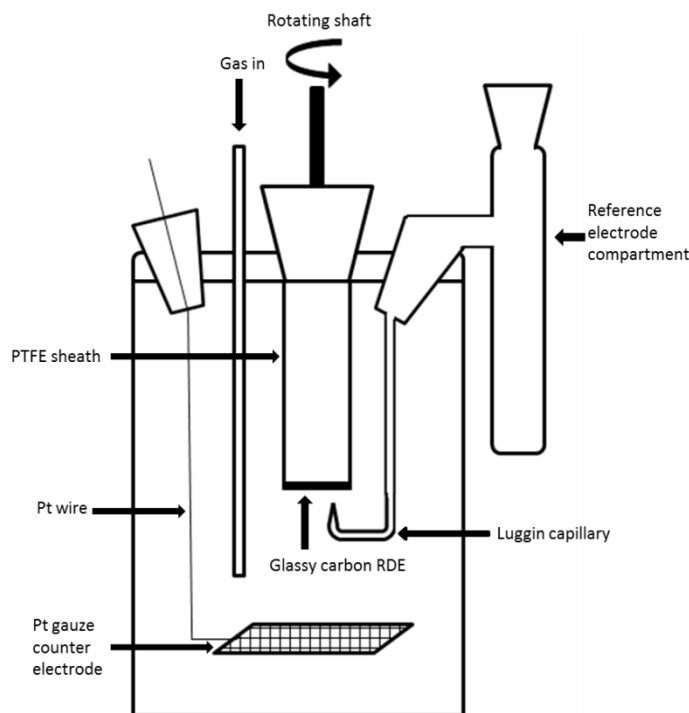


Figure 3 Electrochemical beaker cell used for RDE half-cell studies

2.2.3.2 PEM water electrolyser cell

The electrocatalysts developed in this project were tested as anodes in a single-cell PEM water electrolyser designed and built by *ITM Power*.

2.2.3.2.1 CCM preparation

Catalyst coated membranes (CCM's) were prepared by spraying catalyst inks directly onto Nafion® 115 membranes. Prior to spraying, the Nafion® 115 membranes were cleaned in 5 vol. % H₂O₂ at 90 °C for 3 h, before being rinsed with water and placed in 1 M NaOH at 60 °C for 12 h in order to convert the membranes into their sodium-form by ion exchange. This conversion was performed to improve the glass transition temperature and lower the expansion coefficient of the Nafion® material, making it easier to handle for ink spraying at high temperatures.

Catalyst inks comprising catalyst powder, water, Dispex® dispersing agent and 5 wt. % Nafion® perfluorinated resin solution were mixed on a magnetic stirrer plate for 24 h. The inks were sprayed using an *Iwata* airbrush, with the Nafion® membranes placed on a vacuum plate at 80 °C. The catalyst loading was checked by weighing the CCM periodically between sprayings. After spraying, the CCM's were placed between two Kapton® sheets and hot pressed at 190 °C and 100 kg m⁻² for 1 min. The CCM's were then immersed in 1 M H₂SO₄ at 60 °C for 4 h so as to

Chapter 2: Experimental methods and techniques

convert the Nafion® back to the protonated form. Finally, the CCM's were rinsed and stored in water until required. The active area of each electrode was 8 cm². A commercial Pt black (Ceimig Ltd) electrocatalyst was used as the cathode catalyst.

2.2.3.2.2 PEM electrolyser cell

The CCM's were assembled within a single cell PEM water electrolyser as shown in figures 4 and 5. In the electrolyser assembly the CMM sat between two porous titanium sinters (pore size 10 µm), which acted as a distributor for the current and the water. The sinter used on the anodic side of the cell was Pt-coated so as to prevent passivation of the Ti during O₂ evolution. Ti meshes were placed on top of the Ti sinters, and the entire assembly was compressed by two Ti pistons. The pistons sat in polymethyl methacrylate (PMMA) cell halves that come together to form the body of the cell. The compression of the cell was achieved by tightening bolts used to hold the two PMMA cell halves together. To ensure uniform compression, the bolts were tightened with a torque wrench set to 1 N m. Figure 4 and table 2 show the various cell parts used in the assembly of the PEM electrolyser cell. Figure 5 shows a fully assembled cell with water and gas connections.

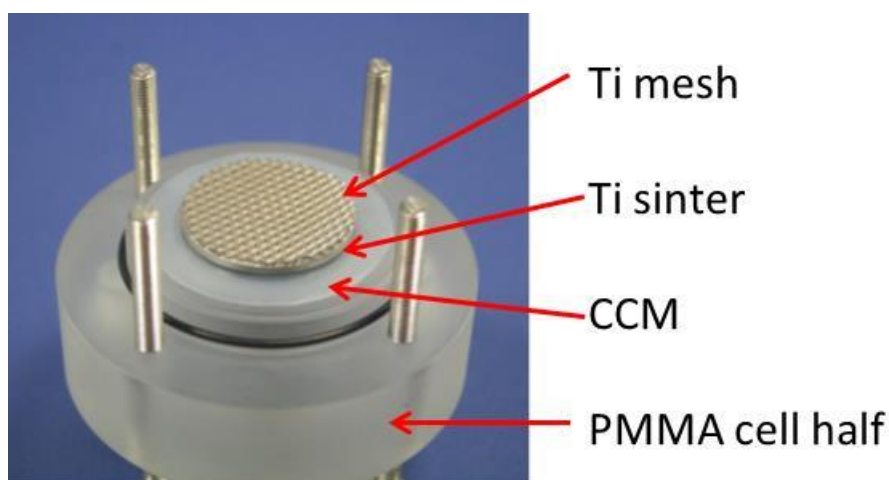
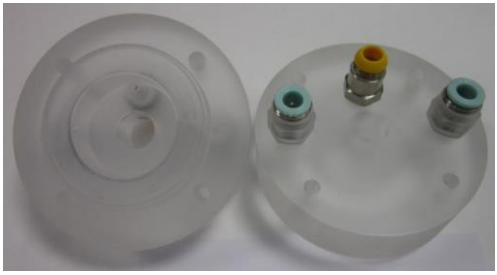


Figure 4 Part assembled PEM cell showing arrangement of cell components (top PMMA cell half removed)

Table 2 PEM electrolyser cell parts

Description	Part
PMMA cell half	
Ti piston	
Ti mesh	
Ti sinter / Pt-coated Ti sinter	

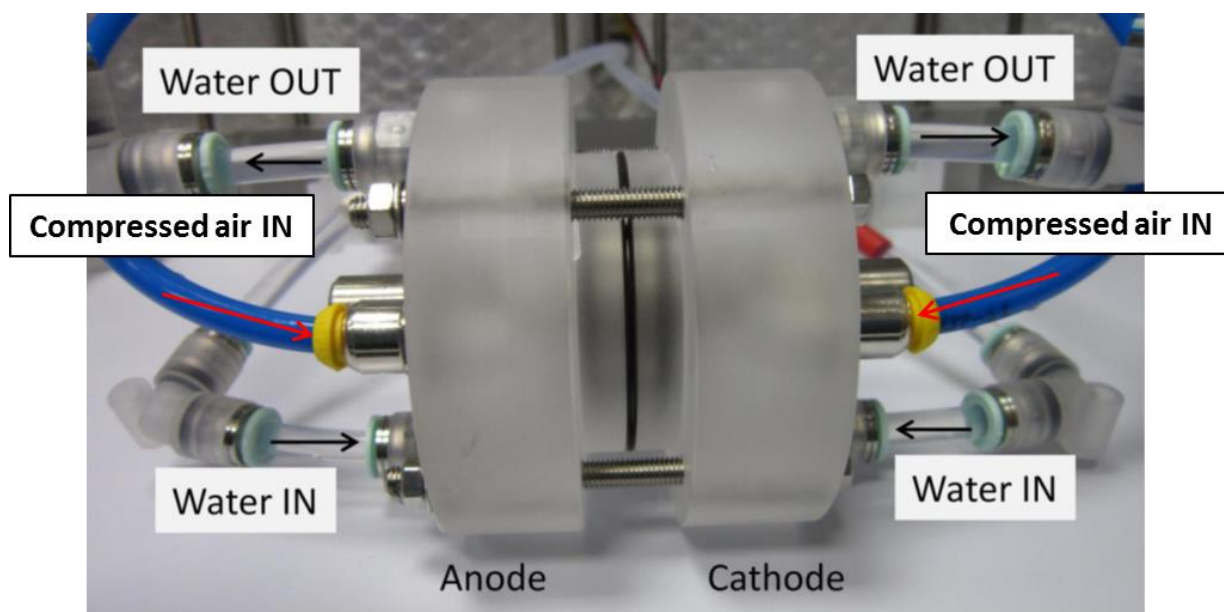


Figure 5 Fully assembled PEM electrolyser cell with labelled water and gas connections

A constant supply of purified Millipore water (Resistivity = $18.2 \text{ M}\Omega \text{ cm}$) was pumped to the anode and cathode sides of the cell at $60 \text{ }^\circ\text{C}$ and at a flow rate of 40 mL min^{-1} . The water was heated by a heat exchanger. In order to facilitate the removal of O_2 and H_2 gas bubbles, the cell was pressurised to 20 bar by blowing compressed air into the back of both sides of the cell. After ensuring the system was leak proof, the cell was left at open circuit potential for 30 min to allow it to heat up to the required temperature ($60 \text{ }^\circ\text{C}$). Setting the anode as the positive terminal and the cathode as the negative terminal, an ISO-TECH IPS-603 DC power supply unit was used to slowly step the current density up to 1 A cm^{-2} . Cells were left at 1 A cm^{-2} for 30 min before any further testing, with the voltage across the cell monitored with a digital voltmeter. Steady state polarisation curves and AC impedance experiments were performed with a Bio-Logic VMP3 potentiostat coupled to a High Current Booster using the EC-Lab software package, with the anode set as the working electrode and the cathode set as the counter/reference electrode. Stability tests were performed with the ISO-TECH IPS-603 DC power supply unit set to 1 A cm^{-2} .

2.3 BET surface area analysis

Gas adsorption measurements are used to determine the surface area of powdered materials. One such method is the Brunauer-Emmet-Teller (BET) isotherm, a model which describes the monolayer formation of an adsorbate species via multilayer physisorption⁶. The technique

enables the volume of a gas required to form a monolayer to be determined, from which the surface area can be calculated. The BET equation is given by equation 5

$$\frac{P}{V(P_0-P)} = \frac{1}{V_m C} + \frac{(C-1)}{V_m C} \left(\frac{P}{P_0}\right) \quad \text{Equation 5}$$

where P is the equilibrium pressure, P_0 is the vapour pressure of the adsorbate gas at standard conditions, V is the volume of gas adsorbed at a particular relative pressure $\left(\frac{P}{P_0}\right)$, V_m is the volume of gas required to cover a monolayer of the surface and C is a temperature dependent constant related to the enthalpies of adsorption of the monolayer and the multilayers. A plot of $\frac{P}{V(P_0-P)}$ vs. $\left(\frac{P}{P_0}\right)$ should therefore be a straight line with an intercept of $\frac{1}{V_m C}$ and a slope of $\frac{(C-1)}{V_m C}$, from which C and V_m can be determined. In practice however, the BET isotherm is only linear for values of $\left(\frac{P}{P_0}\right)$ between 0.05 and 0.3 and so BET plots are constructed between these limits. The surface area of the sample may then be calculated from equation 6

$$\text{Surface area (m}^2\text{)} = V_m \text{ (m}^3\text{)} \times \frac{N_A}{V_A} \text{ (molecules m}^{-3}\text{)} \times A \text{ (m}^2\text{)} \quad \text{Equation 6}$$

Where $\frac{N_A}{V_A}$ is the Avogadro number per unit volume of gas and A is the area of the adsorbate molecule. To compare surface areas of different samples, the surface area is reported relative to the mass of sample used in the measurement, as given by equation 7

$$\text{Specific surface area (m}^2 \text{ g}^{-1}\text{)} = \frac{\text{Surface area (m}^2\text{)}}{\text{Mass of sample (g)}} \quad \text{Equation 7}$$

2.3.1 Experimental details

A Micromeritics Gemini 2375 Surface Area Analyser instrument was used to collect the isotherm data at 77 K, using N_2 as the adsorbate gas (molecular area 16.2 \AA^2). Prior to measurements, weighed samples were dried in glass sample holders for several hours at $180 \text{ }^\circ\text{C}$ under flowing N_2 . Samples were loaded into the BET instrument which automatically collects the isotherm data, performs the required calculations and presents the results.

2.4 Thermogravimetric analysis

Thermogravimetric analysis (TGA) is a thermal analysis technique that explores the properties of a material as a function of temperature. In a TGA experiment, the change in mass of a sample is measured as it is heated with a programmed temperature profile such as a linear

Chapter 2: Experimental methods and techniques

increase or decrease. The technique is useful for examining various chemical and physical processes such as the thermal stability of a material, the mass decreases that occur with the dehydration of a sample, or the mass increases that occur on the uptake of oxygen during an oxidation reaction.

2.4.1 Experimental details

Thermogravimetric analysis was carried out with a Mettler Toledo TGA instrument that was placed in a glove-box under an O₂ atmosphere (O₂ flow rate 50 mL min⁻¹). Samples were heated in ceramic crucibles from 25 to 700 °C with the rate of temperature increase set to 10 °C min⁻¹.

2.5 X-ray diffraction

X-ray diffraction (XRD) is a versatile, non-destructive technique for the identification and quantitative determination of various crystalline phases present in powdered and solid materials. The X-ray diffraction patterns that arise from XRD measurements can provide information on the crystal phases present and the size of any crystallites. Diffraction occurs when the dimensions of the diffracting object are of a similar size to the wavelength of the radiation. X-ray wavelengths are of the order of a few angstroms, a similar magnitude to interatomic distances, and so are scattered by the atoms in a periodic crystal lattice.

Crystal lattices are arranged so that they form a series of parallel planes separated from one another by a distance, d , which varies according to the nature of the material. The planes occur in a number of different orientations, each with its own d -spacing. When a monochromatic X-ray beam with wavelength λ is incident on a lattice plane in a crystal at an angle θ , diffraction occurs when the distance travelled by the rays from successive planes differs by an integer number, n , of wavelengths. This condition for diffraction is expressed by Bragg's Law (equation 8), which is represented schematically in figure 6.

$$n\lambda = 2d \sin \theta$$

Equation 8

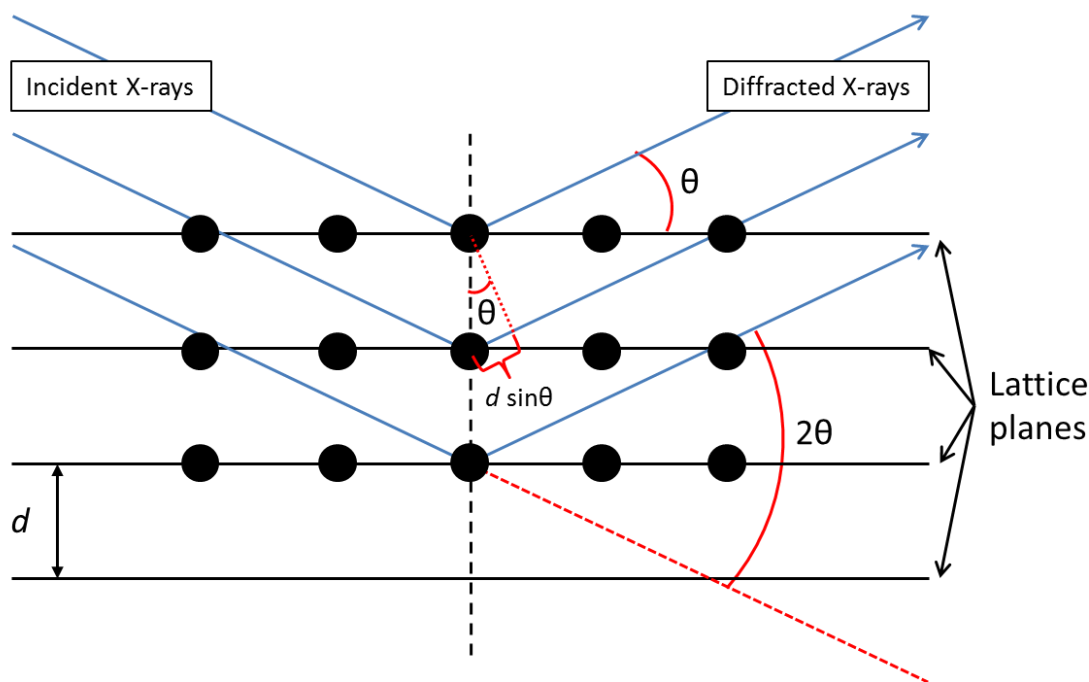


Figure 6 Schematic representation of Bragg's Law

By variation of the angle θ , the Bragg's Law conditions can be satisfied by different d -spacings in polycrystalline materials. A plot of the angular positions versus the intensities of the resultant diffraction peaks produces a pattern, or diffractogram, that is characteristic of the sample. If the sample contains a mixture of different phases, the diffractogram will be formed from the addition of the individual patterns. Identification may be achieved by comparing the diffractogram of the unknown sample with a reference pattern from a database. XRD of powdered materials is carried out by the analysis of diffraction circles, as the crystallite orientation around the glancing angle is random.

The widths of the diffraction peaks provide an indication of the average crystallite size. Narrow peaks are observed for large crystals with long range order while broad peaks are observed for crystallite sizes below 100 nm. Very small crystals and amorphous materials show very broad peaks or none at all, as the X-rays are scattered in many directions. The size of the crystal may be estimated from the width of a peak by the use of the Scherrer equation (equation 9)

$$L = \frac{0.9\lambda}{B_{2\theta} \cos \theta} \quad \text{Equation 9}$$

where L is the average crystallite size, λ is the X-ray wavelength, $B_{2\theta}$ is the full width half maximum of the diffraction peak and θ is the Bragg angle.

Chapter 2: Experimental methods and techniques

2.5.1 Experimental details

XRD for was carried out using an Agilent SuperNova diffractometer with a Cu K α radiation source. XRD patterns were collected over a scan range of 10 ° to 120 ° 2 θ with a 300 s exposure time and the detector set 52 mm from the sample. XRD was also carried out using a Bruker D2 Phaser diffractometer with a Cu K α X-ray source ($\lambda = 1.5418 \text{ \AA}$). XRD patterns were recorded over a scan range of 10 ° to 120 ° 2 θ , with a 0.02° step size and a 0.50 s step time.

The average size of the crystallites was determined with the Scherrer equation using the Rigaku PDXL software package. The instrumental contribution to the broadening of the diffraction peaks was measured by recording the XRD pattern of lanthanum hexaboride (LaB₆). This contribution was subtracted from the measured XRD patterns prior to determining the crystallite size using equation 10

$$\beta = B - b \quad \text{Equation 10}$$

where β is the peak broadening due to lattice strain and crystallite size alone, B is the measured peak width of the test sample and b is the peak width of a sample with no strain and large crystallite size (i.e. LaB₆).

2.6 Electron microscopy and energy dispersive X-ray analysis

In electron microscopy, a beam of electrons is used to illuminate a specimen and produce a magnified image⁷. The effective wavelength of an electron (0.001 – 0.01 nm) is many orders of magnitude shorter than the wavelength of visible light (400 – 700 nm). As the resolution of a microscope is limited by diffraction, a property that increases with wavelength, electron microscopes have much higher magnifications and resolving power than optical light microscopes. Energy dispersive X-ray (EDX) analysis is a technique coupled to electron microscopy that may be used to determine the identity and respective proportions of the elements present in a sample.

2.6.1 Transmission electron microscopy (TEM)

Information regarding the shape and size distribution of nanoparticle catalysts can be obtained from TEM. In a TEM instrument a beam of electrons is transmitted through a very thin sample

(< 0.1 μm) under high vacuum. The image is formed by the interaction of the electrons with the sample and focused onto a fluorescent screen or a digital camera.

2.6.2 EDX analysis

Whenever a material is bombarded with high energy electrons, X-rays of wavelengths characteristic to the elements in the specimen will be emitted. The X-rays relate to the ejection of core-shell electrons from the sample atom, with the subsequent release of energy in the form of X-ray radiation caused by electrons from higher shells relaxing to fill the core-shell vacancy. EDX analysis provides a spectrum of the energy versus the relative counts of the X-rays detected, which can be used to determine the proportion of each element present. EDX analysis may be carried out with TEM samples and with scanning electron microscope (SEM) samples.

2.6.3 Experimental details

TEM images reported in this work were obtained with a JOEL JEM 2100 instrument and a FEI Technai12 system. Specimen samples were prepared by dusting catalyst powders onto carbon coated Cu grids. Area scan EDX was used to determine the relative proportions of the elements present in bulk catalyst samples using a Thermo-Scientific UltraDry EDX system equipped to a Philips XL30 SEM. Specimen samples were prepared for SEM by attaching catalyst powders to adhesive carbon pads on stainless steel sample studs. Linear scan EDX analysis was also performed with TEM samples using the FEI Technai12 TEM system.

2.7 X-ray absorption spectroscopy (XAS)

XAS is a spectroscopic technique that may be used to study the local atomic geometry and chemical state of a selected element within a material. It is a very powerful tool as it is not restricted to crystalline materials, and can be applied to a wide range of highly disordered samples including amorphous phases, liquids and gases. Furthermore, XAS experiments do not require any strict environmental conditions that are needed for other analytical methods (e.g. the use of high vacuum in TEM). The term XAS covers both X-ray Absorption Near Edge Structure (XANES) and Extended X-ray Absorption Fine Structure (EXAFS). XANES provides information on the electronic structure of the sample, while EXAFS provides near-neighbour structural information about the sample.

2.7.1 Theory of XAS

When X-rays pass through a sample, the incident intensity (I_0) of the X-rays will be decreased by an amount that is determined by the adsorption characteristics of the material. The intensity of the X-rays transmitted (I_t) depends on both the thickness (x) and the absorption coefficient (μ) of the sample material. This relationship is described by the Beer-Lambert law (equation 11)

$$I_t = I_0 e^{-\mu x} \quad \text{Equation 11}$$

The absorption coefficient is a function of the photon energy and is proportional to the probability for the absorption of a photon according to Fermi's golden rule^{8,9}. This states that the likelihood of the photon being absorbed depends on the similarity between the initial state of the absorbing atom and the proposed final state¹⁰. The more similar the two states, the more likely absorption will occur.

In an XAS experiment the change in the absorbance (or fluorescence) of a sample is measured as the X-ray energy is scanned through a pre-defined range. In general, the absorbance smoothly decreases with increasing energy as the X-rays become more penetrative, however at specific energies, sharp rises in the absorbance are observed, termed absorption edges. Such edges occur when the X-ray energy, $h\nu$, is absorbed by a core electron of binding energy, E_b , and emitted as a photoelectron with kinetic energy, E_k , equal to equation 12. This process is called the photoelectric effect.

$$E_k = h\nu - E_b \quad \text{Equation 12}$$

The ejected photoelectron is excited into an empty higher valence state or into the continuum, leaving behind an empty core electron orbital known as a core hole. The absorption edges are termed K, L₁, L₂, L₃, etc. based on the principal quantum number of the orbital from which the photoelectron was ejected. The K absorption edge corresponds to an excitation from the 1s orbital, while the L absorption edges, L₁, L₂, L₃, correspond to excitation from the 2s, 2p_{1/2} and 2p_{3/2} orbitals, respectively, as illustrated in figure 7. At energies above an absorption edge, the absorption decreases until the next binding energy is reached.

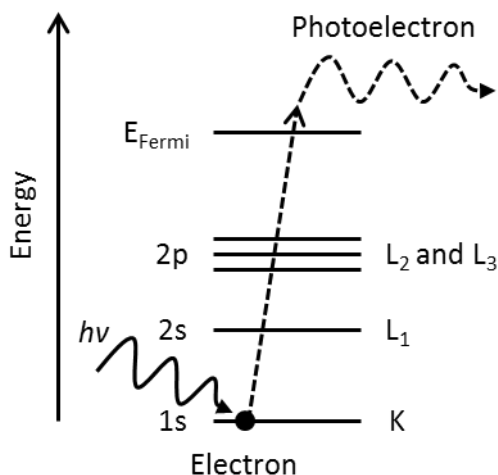


Figure 7 Schematic of the photoelectric effect depicting the excitation of a 1s electron by X-ray energy ($h\nu$) to the continuum, giving rise to a K adsorption edge

The outgoing photoelectron may be thought of as a spherical wave with a wave vector, k that is related to the energy of the incident photon by equation 13

$$k = \sqrt{\left(\frac{8\pi^2 m_e}{h^2}\right)} (h\nu - E_b) \quad \text{Equation 13}$$

where m_e is the mass of an electron. The outgoing photoelectron wave scatters off all surrounding neighbouring atoms. The scattering may be a single scattering event in which the photoelectron scatters off a nearby atom and then returns directly to the absorbing atom. Alternatively, the photoelectron may scatter off one nearby atom and then another nearby atom before returning to the absorbing atom. This is known as multiple scattering.

A typical XAS spectrum is shown in figure 8. The XAS spectrum may be divided into two regions, the XANES and the EXAFS regions, as shown in figure 9. The XANES region includes the pre-edge, where the energy of the incident X-rays is not sufficient to excite a core electron of the studied element, and extends to about 50 – 100 eV above the absorption edge. The EXAFS region extends from the absorption edge up to around 1000 eV above the edge.

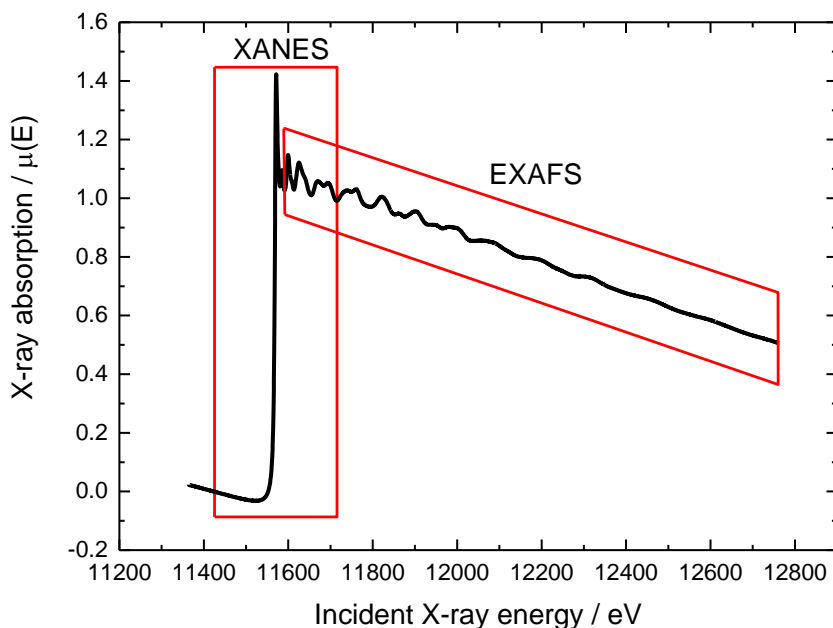


Figure 8 XAS spectrum of a Ru foil at the Ru K-edge highlighting the XANES region and the EXAFS regions

2.7.2 EXAFS

EXAFS analysis interprets the oscillations in the XAS spectra at incident X-ray energies above the absorption edge. The photoelectrons in this region have high kinetic energy and single scattering by nearest neighbour atoms dominates. The oscillations contain structural information about the local geometry around the absorbing atom such as the near-neighbour distances, coordination number and the level of disorder in the system. The oscillations are caused by interference between the outgoing photoelectron wave and the backscattered waves from neighbouring atoms, as illustrated by figure 9. At energies where scattering results in positive interference the absorption increases, and at energies where there is negative interference the absorption decreases. The oscillatory behaviour of the absorption can be defined in terms of the wave vector of the photoelectron, k , as given by equation 14

$$\chi(k) = \frac{\mu_{tot}(k) - \mu_0(k)}{\mu_0(k)} \tag{Equation 14}$$

where $\mu_{tot}(k)$ is the total absorption, $\mu_0(k)$ is the background absorption and $\chi(k)$ is the extracted EXAFS signal.

Information about the local geometry around the absorbing atom is determined by curve fitting the experimental data to a theoretical standard, utilising the EXAFS equation¹¹. In this work, quantitative EXAFS analysis has not been carried out and thus further explanation is not within the scope of this thesis.

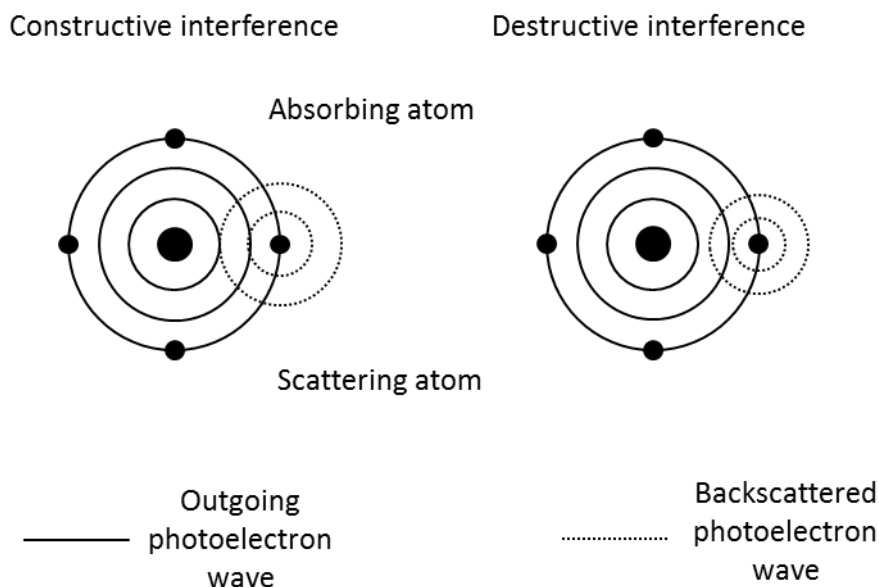


Figure 9 Schematic of constructive and destructive interference of an outgoing photoelectron. The circles represent the maxima of the photoelectron waves

2.7.3 XANES

The absorption features observed in the XANES region are mainly due to electronic transitions from core level electrons to higher unfilled or partially filled orbitals. Interpretation of this region is complicated by the absence of a simple physical description of the process. In contrast to EXAFS, modelling the region is very difficult as the region is dominated by multiple scattering effects¹². The majority of XANES analysis is therefore semi-quantitative. Despite this limitation the XANES region still provides significant chemical information, in particular the oxidation state of the absorbing atom and the coordination environment.

The position of the absorption edge is determined by the coulombic interaction between the nucleus of the absorbing atom and the electron involved in the photoelectronic transition. This interaction is in turn screened by all the other electrons around the absorbing atom. With increasing oxidation state of the absorbing atom, the absorption edge energy is therefore increased by a few electronvolts^{13,14}. This is because the core electron requires more energy to excite as the nucleus is less shielded and carries a higher effective charge. The oxidation state

Chapter 2: Experimental methods and techniques

of an unknown sample can be determined by comparison with model systems that have known oxidation states. Such an approach has been adopted previously for both Ir and Ru oxides¹⁵⁻¹⁷, however these studies were not recorded under O₂ evolution conditions. The first XANES study of IrO₂ under O₂ evolution conditions was carried out recently using an electrodeposited IrO₂ film¹⁸.

In some XANES spectra such as the Ir L₃ spectra shown in figure 10, the absorption edge features a sharp intense peak at the top of the edge that is called a “white line”. White lines arise from selection rule allowed electric dipole transitions to unoccupied final states. For example at the Ir L₃ edge, a white line is observed due to the excitation of electrons from the 2p_{3/2} level to unoccupied *nd* states¹⁹. The intensity of the white line may also be enhanced by multiple scattering effects and/or from transitions into a large number of partially filled orbitals²⁰.

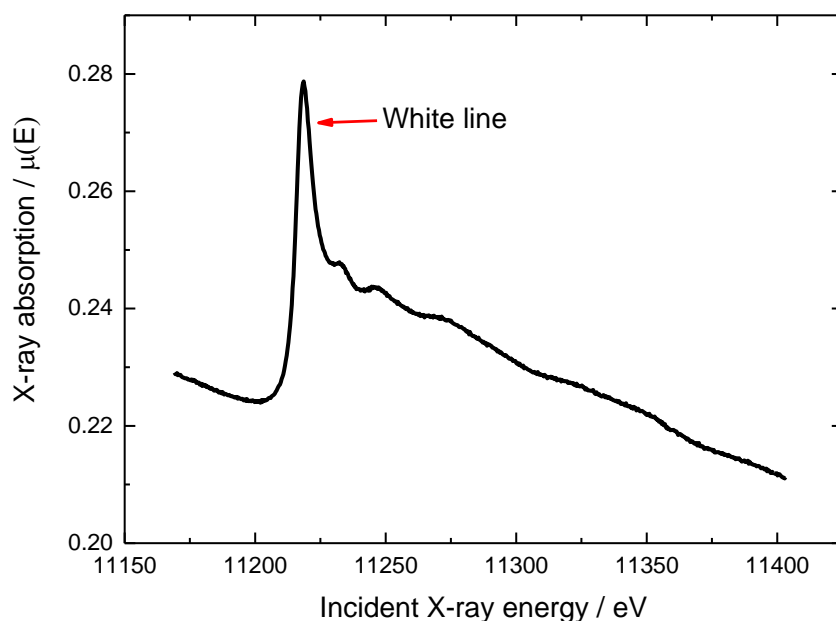


Figure 10 XAS spectrum of an IrO₂ pellet at the Ir L₃-edge highlighting the white line at about 11218 eV

2.7.4 Experimental aspects of XAS

2.7.4.1 Synchrotron

XAS measurements are usually made at synchrotron radiation facilities. The facility used in this study was the Diamond Light Source, Harwell Science and Innovation Campus, UK. Synchrotron radiation is emitted by charged particles that are travelling close to the speed of light and contained within a storage ring defined by bending magnets. At Diamond Light Source, bunches of electrons from an electron gun are accelerated by a linear accelerator, and fed into a booster ring which further accelerates them to their final energy (3 GeV at Diamond Light Source). Electrons are then injected from the booster ring into the storage ring, which keeps them travelling in a closed loop using a series of dipole bending magnets. The bending of the electrons causes them to lose energy, which is emitted as synchrotron (X-ray) radiation at tangents to the electron beam path. The storage ring is kept under ultra-high vacuum to ensure a long lifetime of the circulating beam. The emitted X-rays are highly intense, collimated and cover a wide range of energies²¹, and are conveyed through to beamlines which tune the radiation to the desired energy and profile via a series of X-ray optics.

2.7.4.2 Beamline B18

B18 has an energy range of 2 – 35 keV, with the X-rays supplied by a bending magnet source. XAS measurements at the Ru edge were carried out using a Si(311) crystal monochromator, with a Pt coated mirror used to reject higher harmonics. XAS measurements at the Ir edge were collected using a Si(111) crystal monochromator, with a chromium coated mirror used to reject higher harmonics. A nine element germanium detector was used for fluorescence detection. The beamline scientist was Diego Gianolio (Diamond Light Source) and the experiments were conducted by Peter Richardson (University of Southampton), Andrea E. Russell (University of Southampton), Steve Thompson (University of Southampton), Svein Sunde (Norwegian University of Science and Technology) and Anita Reksten (Norwegian University of Science and Technology).

2.7.4.3 XAS transmission measurements

Transmission mode XAS uses three X-ray detectors that are positioned sequentially in the beamline, as shown by figure 11. A transmission XAS experiment measures the difference in X-ray absorption between two detectors as the energy is changed. The X-ray absorption edge (μx) of a sample is determined by measuring the X-rays transmitted before (I_0) and after (I_t) the sample and rearranging equation 15

$$\mu x = \ln\left(\frac{I_0}{I_t}\right) \quad \text{Equation 15}$$

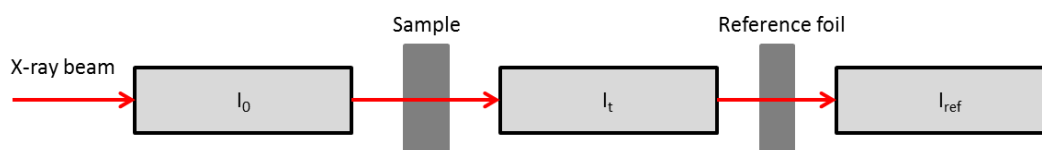


Figure 11 Schematic of the X-ray detector set-up for transmission XAS experiments showing the incident (I_0), transmission (I_t) and reference (I_{ref}) ionisation chambers

The X-ray detectors are ionisation chambers that consist of a pair of electrodes held at a constant potential, with an inert gas (or a mixture of gases) between them. When the X-ray beam passes through a chamber, some of the X-rays are absorbed by the gas forming electron/positive ion pairs. The electrons migrate to the anode and the positive ions migrate to the cathode, with the resulting current being directionally proportional to the number of X-ray photons entering the chamber. The gas in each chamber is set so that it only absorbs a specific amount of the X-ray beam, typically 5 – 15 % for I_0 and 70 – 80 % for I_t and I_{ref} , so that enough of the beam passes through the sample, reference foil and all detectors.

Transmission experiments are typically used for concentrated samples. For dilute samples, the X-ray absorption is low resulting in a poor signal-to-noise ratio. In such cases fluorescence measurements should be used (described in section 7.2.4). If the sample is too concentrated, all of the X-rays will be absorbed and no beam will pass through to the detectors. For multi-elemental samples, the absorption characteristics of the other elements must therefore be considered. An ideal adsorption edge (μx) of the probed element is between 0.3 and 1.0, with the total sample absorption being less than 2.5. The appropriate mass of sample required for a transmission experiment may be calculated from equation 16

$$mass = \frac{(\mu x)(sample\ area)}{(\mu_p)} \quad \text{Equation 16}$$

where μ_p is the mass absorption coefficient of the element under study. Values of mass absorption coefficient for the transmission experiments done in this work have been taken from the McMasters tables²².

The homogeneity of the sample is also important for transmission experiments, as any small holes in the sample causes X-ray leakage that results in increased noise in the data. All

transmission samples for this work were prepared as pellets mixed with boron nitride or cellulose, as these materials have low X-ray absorption coefficients at the Ir L₃ and Ru K edge. The pellets were compacted using a purpose built press.

2.7.4.4 XAS fluorescence measurements

For dilute samples, XAS fluorescence measurements are used. X-ray fluorescence occurs when an electron from a higher energy orbital relaxes to fill the core hole left by the ejected photoelectron. This may result in either an Auger electron or a fluorescence X-ray with energy equal to the difference between the two orbitals, being emitted. The emitted X-ray can be detected by a fluorescence detector positioned at 90 ° to the incident beam, with the sample positioned at 45 °, as shown by figure 12.

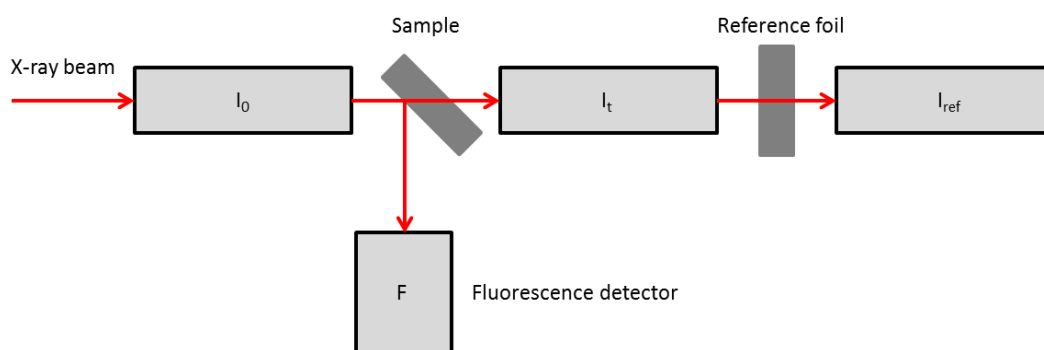


Figure 12 Schematic of the X-ray detector set up for fluorescence XAS measurements. I_0 , I_t and I_{ref} are the incident, transmission and fluorescence detectors, respectively, and F is the fluorescence detector

Solid state fluorescence detectors are the most common type and in this work, a nine element germanium detector was used. Each fluorescence photon emitted from the sample is absorbed by one of the Ge elements, which generates a pulse of charge the magnitude of which is proportional to the energy of the X-ray photon. The pulses are counted, providing an energy spectrum that is sent through to a computer.

All fluorescence XAS samples in this study were prepared as electrocatalyst layers on teflonated carbon paper discs (see section 7.2.5.1 for details).

2.7.4.5 In-situ electrochemical XAS measurements

An in-situ electrochemical cell was developed specifically for the XANES and EXAFS measurements collected in this work. The cell was designed by Peter Richardson, Andrea E. Russell and Konstant Venter (University of Southampton) and built by Konstant Venter. The

Chapter 2: Experimental methods and techniques

design of the cell was based on a design of a half cell for testing MEA's by Mayousse et al²³. For in situ XAS characterisation the cell was required to; (i) be transparent to X-rays; (ii) display good electrochemistry; (iii) be leak tight; (iv) have a short X-ray path length; and (v) efficiently remove gas O₂ and H₂ gas bubbles from the surface of the electrode.

A picture of the cell is shown in figure 13. The working electrode was held in place by a 0.5 mm Au contact wire. The counter electrode consisted of a Pt wire and the reference electrode was a MMS electrode that was connected to the cell by a PTFE capillary tube. A Masterflex C/L 77120-62 peristaltic pump was used to introduce electrolyte solution into the cell and fill the reference electrode tube. Gas bubbles were swept away from the surface of the electrode by constantly pumping electrolyte solution throughout the entire XAS measurements. The electrodes were connected to an Autolab PGSTAT30 using the GPES software programme.

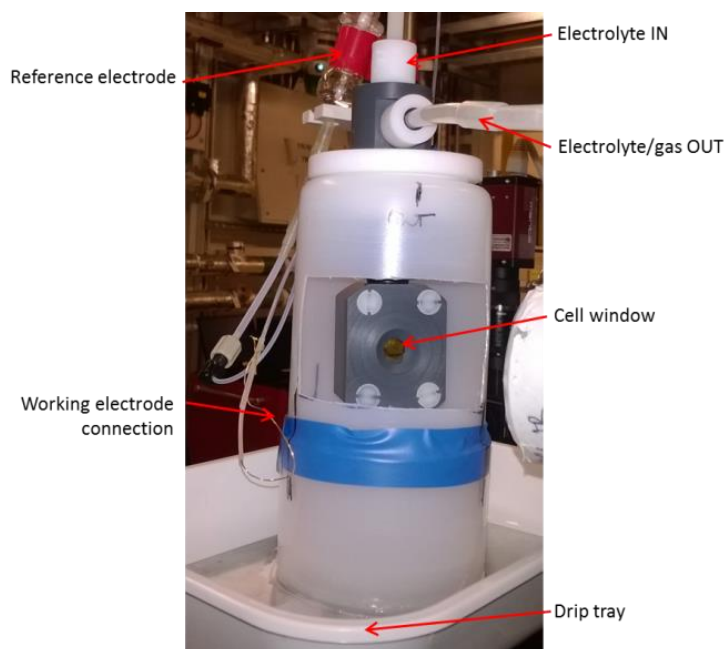


Figure 13 In-situ electrochemistry XAS cell

Figure 14 shows the quality of the cyclic voltammetry obtained using the in-situ cell. Cyclic voltammetry at a sweep rate of 50 mV s⁻¹ was used to check a good working electrode connection, prior to the start of each in-situ XAS experiment. In order to investigate the effect of potential on the oxidation state and structure of the electrocatalysts, the potential of the working electrode was held at a constant value whilst the XAS measurements were performed. The potentials used in this study were 1.00, 1.40, 1.70 and 1.80 V vs. RHE.

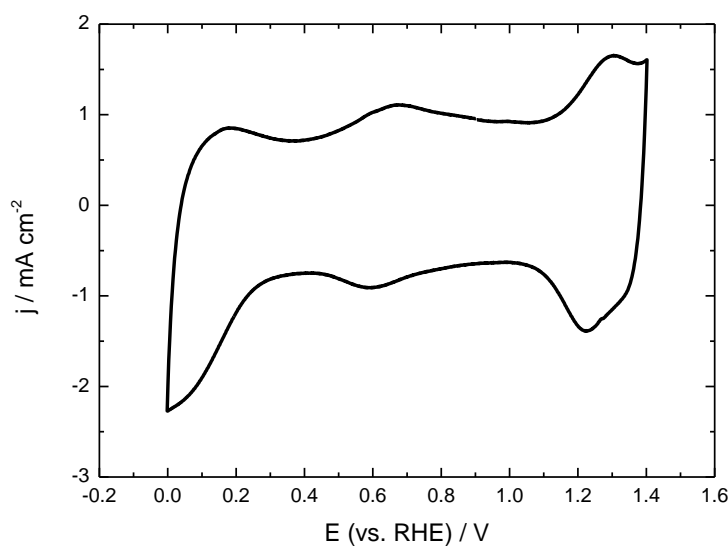


Figure 14 Cyclic voltammetry of a RuO₂ painted carbon paper electrode (surface area 1.247 cm²) obtained in the in-situ electrochemistry XAS cell, in 0.5 M H₂SO₄ at a scan rate of 50 mV s⁻¹

2.7.4.5.1 Electrode preparation

Catalyst electrode samples for in-situ XAS experiments were prepared by brush coating catalyst inks onto teflonated carbon paper. The required amount of catalyst (20 mg) and activated carbon (Vulcan XC-72R) (4 mg) was dispersed in a mix of water (1 ml) and IPA (0.2 ml). The activated carbon was added to improve the ink consistency and to facilitate brush coating. A required amount of 5 wt % Nafion perfluorinated resin solution was added (228 μ L), to prepare a dry catalyst layer with 50 wt. % Nafion solids with respect to the mass of catalyst. The ink mixture was dispersed for 30 min in a Fisher Ultrasonic Bath followed by 3 min with a Fisher PowerGen 125 homogeniser. Thin layers of ink were painted onto teflonated carbon paper disks with an area of 5.31 cm². The disks were dried on a hot plate and rotated 90 ° between coats to ensure an even distribution of ink on the electrode. The process was repeated until a total catalyst loading of about 0.2 mg cm⁻² was obtained. The electrodes were hot-pressed at 1 bar and 180 °C for 3 min. Electrodes of appropriate size (1.247 cm²) were cut out of the larger sheet and hydrated prior to electrochemical testing by boiling in purified water.

2.7.4.6 Data processing

The raw XAS data files data were processed using the ATHENA software programme, which is part of the IFEFFIT software suite²⁴.

The raw data files were imported into ATHENA where they were normalised and calibrated. To improve the signal-to-noise ratio, several XAS scans for each measurement were merged using the same processing parameters. XAS spectra were normalised to set the absorption edge to 1, as shown in figure 15. This allows data from different experiments at the same edge to be compared. Normalisation was achieved by (i) fitting a linear pre-edge extrapolated to maximum energy; (ii) fitting a quadratic post-edge function to the data that passed through the middle of all oscillations in the data; and then (iii) subtracting both from the raw data.

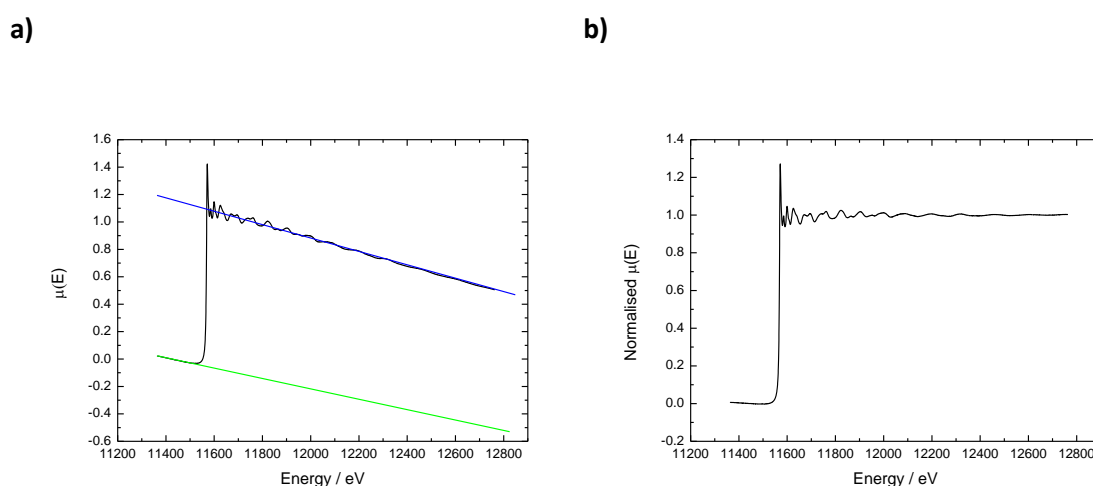


Figure 15 Normalisation of Pt foil EXAFS data: a) Raw $\mu(E)$ data (black line) showing pre-edge (green line) and post-edge (blue line) functions; b) normalised $\mu(E)$ data

The energy scale was calibrated to a reference foil measured at each absorption edge. The first peak of the first derivative of the reference foil was set to the tabulated absorption energy²², and the same shift in energy was then applied to the sample data. The absorption edge energy (E_0) of the sample data was then selected. Although E_0 is in principle related to the binding energy of the core electron, it is difficult in practice to determine this energy exactly as the absorption edge does not start abruptly. Common points at which E_0 may be chosen include the first peak in a plot of the first derivative of the spectrum, at the top of the white line or halfway up the absorption edge.

To isolate the EXAFS oscillations, background subtraction was required to remove the contribution to the total absorption from the absorption by a single atom. The background was subtracted by fitting a spline to the data that passed through all the nodes of the EXAFS oscillations, without following the oscillations themselves. The spline function was subtracted automatically using the AUTOBK algorithm present in ATHENA²⁵. The software was then used to convert the data from energy to wavenumber. The resulting $\chi(k)$ plot can be weighted to amplify the signal at higher values of k . The $\chi(k)$ plot was then Fourier transformed to plot the data in R space, as shown in figure 16.

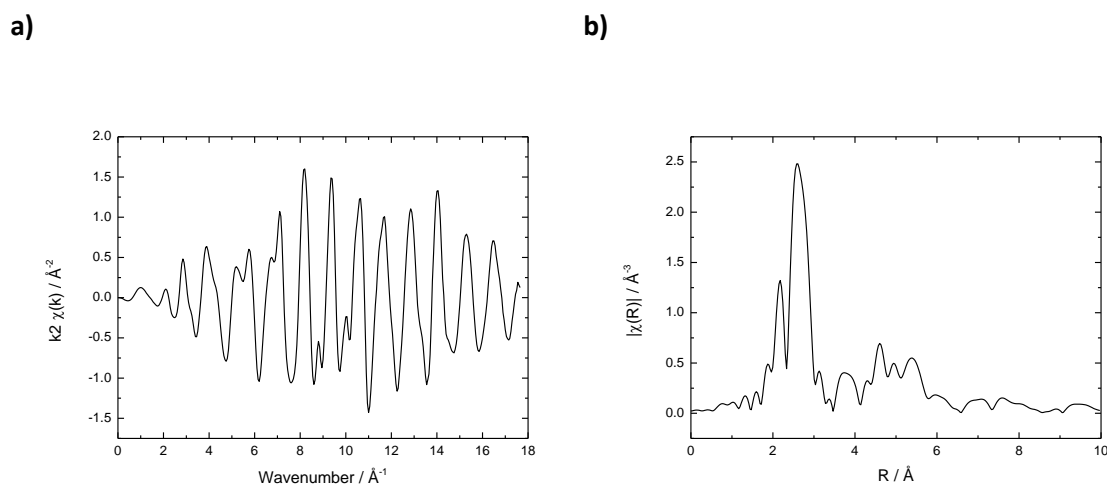


Figure 16 a) k^2 weight $\chi(k)$ data and b) corresponding Fourier transform

2.8 References

- (1) Trasatti, S.; Buzzanca, G. *Journal of Electroanalytical Chemistry and Interfacial Electrochemistry* **1971**, *29*, A1.
- (2) Trasatti, S. *Electrochimica Acta* **1991**, *36*, 225.
- (3) Burke, L. D.; Murphy, O. J. *Journal of Electroanalytical Chemistry and Interfacial Electrochemistry* **1979**, *96*, 19.
- (4) Lodi, G.; Sivieri, E.; Battisti, A.; Trasatti, S. *Journal of Applied Electrochemistry* **1978**, *8*, 135.
- (5) Ardizzone, S.; Fregonara, G.; Trasatti, S. *Electrochimica Acta* **1990**, *35*, 263.
- (6) Atkins, P.; Paula, J. d. *Physical Chemistry*; Oxford University Press: Oxford, 2002.
- (7) Watt, I. *The principles and practice of electron microscopy*; 2nd ed.; Cambridge University Press: Cambridge, 1997.
- (8) Dirac, P. A. M. *Proceedings of the Royal Society of London. Series A* **1927**, *114*, 243.

Chapter 2: Experimental methods and techniques

- (9) Rehr, J. J.; Albers, R. C. *Reviews of Modern Physics* **2000**, *72*, 621.
- (10) Calvin, S. *XAFS for Everyone*; Taylor and Francis Group: Boca Raton, Florida, 2013.
- (11) Stern, E. A. *Contemporary Physics* **1978**, *19*, 289.
- (12) Rehr, J. J.; Ankudinov, A. L. *Coordination Chemistry Reviews* **2005**, *249*, 131.
- (13) Cramer, S. P.; Eccles, T. K.; Kutzler, F. W.; Hodgson, K. O.; Mortenson, L. E. *Journal of the American Chemical Society* **1976**, *98*, 1287.
- (14) Arčon, I.; Benčan, A.; Kodre, A.; Kosec, M. *X-Ray Spectrometry* **2007**, *36*, 301.
- (15) McKeown, D. A.; Hagans, P. L.; Carette, L. P. L.; Russell, A. E.; Swider, K. E.; Rolison, D. R. *The Journal of Physical Chemistry B* **1999**, *103*, 4825.
- (16) Mo, Y.; Stefan, I. C.; Cai, W.-B.; Dong, J.; Carey, P.; Scherson, D. A. *The Journal of Physical Chemistry B* **2002**, *106*, 3681.
- (17) Hillman, A. R.; Skopek, M. A.; Gurman, S. J. *Physical Chemistry Chemical Physics* **2011**, *13*, 5252.
- (18) Minguzzi, A.; Lugaresi, O.; Achilli, E.; Locatelli, C.; Vertova, A.; Ghigna, P.; Rondinini, S. *Chemical Science* **2014**, *5*, 3591.
- (19) Choy, J.-H.; Kim, D.-K.; Demazeau, G.; Jung, D.-Y. *The Journal of Physical Chemistry* **1994**, *98*, 6258.
- (20) Bunker, G. *Introduction to XAFS*; Cambridge University Press: Cambridge, 2010.
- (21) Bunnker, G. *Introduction to XAFS; A Practical Guide to X-ray Absorption Fine Structure Spectroscopy*; Cambridge University Press: Cambridge, UK, 2010.
- (22) McMaster, M.; Kerr Del Grande, N.; Mallett, J. H.; Hubbell, J. H. *Compilation of X-ray Cross Sections*, Lawrence Livermore National Laboratory Report UCRL-50144 Section II Revision I, 1969.
- (23) Mayousse, E.; Maillard, F.; Fouda-Onana, F.; Sicardy, O.; Guillet, N. *International Journal of Hydrogen Energy* **2011**, *36*, 10474.
- (24) Ravel, B.; Newville, M. *Journal of Synchrotron Radiation* **2005**, *12*, 537.
- (25) Newville, M.; Liviņš, P.; Yacoby, Y.; Rehr, J. J.; Stern, E. A. *Physical Review B* **1993**, *47*, 14126.

3. Mixed iridium-ruthenium oxide electrocatalysts for O₂ evolution

3.1 Introduction

IrO₂ and RuO₂ are the two most active materials for the O₂ evolution reaction in acidic media¹. The precise mechanism of O₂ evolution on these metal oxides is not fully understood. However it is believed that the key catalytic step involves the electrochemical generation of an unstable and reactive higher oxidation state of the metal centres at the electrode/electrolyte interface, Ru(VI)/Ru(VIII) in the case of RuO₂ and Ir(IV)/Ir(VI) for IrO₂²⁻⁴. The evolution of O₂ occurs with the regeneration of the lower oxidation state.

Although RuO₂ is more active than IrO₂, its inherent instability at operational electrolysis potentials renders it unsuitable for commercial electrolyzers². IrO₂ is a more practical choice of catalyst because it is stable and almost as active as RuO₂. A composite catalyst containing both active materials is an attractive proposition because of the potential optimum of activity and stability. The replacement of the more expensive Ir with the cheaper Ru would be of additional economic benefit.

Mixtures of IrO₂ and RuO₂ have been investigated previously in the literature⁵⁻¹⁰. Several of these studies have shown that the stability of RuO₂ during O₂ evolution is significantly enhanced by the addition of Ir, while the activity of the composites is improved compared to pure IrO₂. However, although the importance of intimate atomic mixing for exploiting any synergic effects has been established⁵, the precise interaction between Ir and Ru during O₂ evolution has yet to be determined.

Thin films of IrO₂-RuO₂ mixtures were prepared via reactive sputtering by Kötz et al⁷. It was demonstrated that the addition of even small amounts of IrO₂ (≥ 20 mol %) reduced the corrosion rate of the catalyst during O₂ evolution a 1 A cm⁻² to about 4 % of the rate measured for RuO₂. The redox peaks in the cyclic voltammetry and the O₂ evolution potentials at 0.1 mA cm⁻² shifted with the catalyst composition in a way that did not correspond to a linear combination of the properties of the pure oxides, implying an interaction between the Ir and the Ru. XPS analysis suggested that a common valence band existed, with electrons on IrO₂ sites shared with RuO₂ sites. It was hypothesised that the common band prevents the Ru from being oxidised to the soluble RuO₄, which suppresses the corrosion rate but also reduces the

Chapter 3: Mixed iridium-ruthenium oxide electrocatalysts for O_2 evolution

activity of the Ru sites. A similar peak shift in the cyclic voltammetry was also observed by Kodintsev et al. for thin films of IrO_2 - RuO_2 oxides prepared by thermal decomposition¹¹.

Thin film catalyst layers, however, are not ideal for PEM water electrolyzers as they cannot be satisfactorily integrated with the PEM electrolyte. Instead, metal oxide powders are more convenient to use. Mixed IrO_2 - RuO_2 metal oxide powders have been prepared by a number of different routes including the Adams fusion, hydrolysis and Pechini-Adams methods.

The Adams fusion method proceeds via the pyrolysis of a metal chloride precursor in molten sodium nitrate¹². Cheng et al. prepared nanoparticle $Ir_xRu_yO_2$ powders by this method across the entire composition range⁹. The synthesised $Ir_xRu_yO_2$ were shown to be more active than IrO_2 and more stable than RuO_2 . An $Ir_{0.4}Ru_{0.6}O_2$ anode catalyst in a single cell PEM electrolyser at 500 mA cm^{-2} was stable for over 100 h. However cyclic voltammetry of these samples in $0.5 \text{ M H}_2\text{SO}_4$ was too ambiguous to show a trend in redox peak positions with composition. Song et al. used repetitive cyclic voltammetry at potentials below the onset of O_2 evolution to investigate the stability of $Ir_{0.50}Ru_{0.50}O_2$ ¹⁰. It was found that although the voltammetric capacitance of the mixed electrocatalyst decreased with increasing number of potential cycles, the decrease was significantly less than pure RuO_2 or metallic Ru.

In the Pechini-Adams method polymeric precursors containing metallic cations in the polymeric chain are thermally decomposed, and then calcined in oxygen to obtain the oxide species. Mamaca et al. reported that $Ir_xRu_yO_2$ prepared in this way showed good activity and stability in a PEM cell⁶. However XRD analysis revealed that the synthesised powders consisted of separate oxide phases, with metallic Ir and Ru also present.

The hydrolysis method involves the formation of a metal hydroxide or hydrated oxide precipitate by the reaction of the precursor metal salt with aqueous sodium hydroxide solution. The precipitate is oxidised by subsequent heat treatment. Marshall et al. prepared both $Ir_xRu_yO_2$ and $Ir_xRu_yTa_zO_2$ oxides with this method^{13,14}. The cell voltage of single cell PEM electrolyzers was found to increase with the increase in tantalum content in the anode catalyst, as Ta oxides have low O_2 evolution activities. The best PEM cell performance was achieved with an $Ir_{0.6}Ru_{0.4}O_2$ anode catalyst with a cell voltage of 1.58 V at 1 A cm^{-2} .

The importance of intimate atomic mixing in exploiting synergic effects for powder $Ir_xRu_yO_2$ catalysts, was investigated by Owe et al.⁵. High resolution XRD was used to show that single phase oxides were formed for samples with Ir contents $\leq 50 \text{ mol}\%$. As both IrO_2 and RuO_2 have the same rutile crystal structure, similar ionic radii¹⁵ (Ir^{4+} 0.625 \AA , Ru^{4+} 0.615 \AA), a similar

Chapter 3: Mixed iridium-ruthenium oxide electrocatalysts for O₂ evolution

electronegativity and the same valency, the formation of substitutional Ir_xRu_yO₂ solid solutions is favourable, according to Hume-Rothery theory¹⁶. However, although the formation of solid solutions for mixtures of IrO₂ and RuO₂ has been demonstrated several times¹⁷⁻¹⁹, the surface segregation of one of the components is also possible^{5,11,20}. In their work, Owe et al. found that the electrochemical activities for the O₂ evolution reaction of the single phase Ir_xRu_yO₂ were very similar to physically mixed samples of the pure oxides in the same molar ratios. It was proposed that any synergic interaction between the Ir and Ru was therefore weaker than what had been suggested for the sputtered thin films in the earlier work of Kötz et al.

The structure and electronic state of Ir_xRu_yO₂ materials may also be investigated by XAS measurements. XANES provides information of the average valency of the metal species as the position of the absorption edge shifts to higher energies with increasing oxidation state. EXAFS provides structural information of the environment around the absorbing atom such as the number and type of surrounding atoms, and the distances between them.

The structure of dry Ir_xRu_yO₂ catalysts may be elucidated with ex situ XAS measurements. Bestaoui et al. investigated dry IrO₂ powders prepared by a hydrolysis method²¹. It was shown that the Ir existed in an octahedral environment with six neighbouring O atoms, consistent with rutile geometry. The structural disorder was also found to decrease with calcination temperature, as the material became more crystalline. McKeown et al. demonstrated that the local structure of anhydrous RuO₂ is similar, with the long range order consisting of a three dimensional network of octahedral chains²². In contrast, hydrous RuO₂.xH₂O was shown to be more disordered with no evidence of a three dimensional network. An EXAFS study of mixed IrO₂-RuO₂ films was carried out by Arikawa et al¹⁹. It was found that the radial distribution function showed a continuous change with the oxide composition, which was suggested to be evidence of solid solution formation. Possible solid solution formation for Ir_xRu_yO₂ powders prepared by the hydrolysis method was also found in EXAFS analysis by Marshall¹⁷.

In situ XAS analysis allows the effect of potential on the electronic state and structure of metal oxide catalysts to be followed. Pauporté found a reduction in the Ir-O bond length from 2.01 to 1.96 Å for sputtered IrO₂ films, with an increase in the potential from 0 to 1 V vs. a saturated calomel reference electrode (approx. 0.24 to 1.24 V vs. RHE)²³. This corresponded with a change in the Ir oxidation state from 3.03 to 3.85 as measured from the position of the Ir L₃ white line position, based on the assumption that the Ir was in the III valence state at a potential just prior to the onset of H₂ evolution at -0.2 V vs. SCE. A similar change in bond length from 2.02 Å at 0.40 V to 1.94 Å at 1.20 V vs. RHE, was observed for electrodeposited

Chapter 3: Mixed iridium-ruthenium oxide electrocatalysts for O₂ evolution

RuO₂ films²⁴. Hüppauff et al. used the white line energy position of Ir oxalate and Ir oxide as references for Ir +3 and Ir +4 to estimate, based on a linear regression, the oxidation state of an anodically formed Ir oxide film (AIROF) at various potentials between -0.24 and 1.21 V vs. Ag/AgCl (approx. 0 and 1.4 V vs. RHE) in 1 M H₂SO₄²⁵. It was shown that the Ir reached an oxidation state of 4.8 immediately preceding the onset of O₂ evolution at about 1.4 V vs. RHE.

In this chapter, Ir_xRu_yO₂ electrocatalyst powders for the O₂ evolution reaction have been synthesised across the composition range by the Adams fusion method. Physical characterisation of the oxides has been performed by EDX, XRD, TEM and BET surface area analysis. Electrochemical measurements have been carried out with the oxides as thin film electrodes in 0.5 M H₂SO₄ and as the anode catalysts in single cell PEM electrolyzers. Ex and in situ XANES analyses have been employed to characterise the oxidation states of the Ir and Ru metal components of the catalysts under potential control, with an aim to establishing the compositional dependency of the activity and stability of the electrocatalysts during O₂ evolution.

3.2 Experimental details

3.2.1 Preparation of Ir_xRu_yO₂ electrocatalysts

IrO₂, Ir_{0.75}Ru_{0.25}O₂, Ir_{0.50}Ru_{0.50}O₂, Ir_{0.25}Ru_{0.75}O₂ and RuO₂ catalyst powders were prepared by the Adams fusion method. H₂IrCl₆·xH₂O and RuCl₃·xH₂O precursors were added to isopropanol and stirred for 2 h. The total metal concentration of the solution was 0.08 M. A large excess of NaNO₃ (~150X molar excess) was added and the mixture stirred and then dried overnight at 60 °C. The dry mixture was ground with a pestle and mortar and placed in a preheated box furnace at 500 °C for 1.5 h, before the heating element was turned off and the mixture allowed to cool slowly to room temperature. The fused salt-oxide mixture was rinsed into a beaker of water and warmed overnight at 40 °C so as to dissolve any residual salts. The metal oxide powders were separated and washed several times by centrifuge at 5000 rpm, replacing the colourless supernatant with water each time. The recovered powders were dried in an oven at 110 °C and ground until fine with a pestle and mortar.

3.2.2 EDX analysis

A Phillips XL30 SEM equipped with a Thermo-Scientific UltraDry EDX system was used to examine the composition of the catalyst samples. Area scan EDX analysis was performed at an accelerating voltage of 20 kV and working distance of 10 mm.

3.2.3 XRD

XRD was carried out on a Bruker D2 Phaser diffractometer with a step size of 0.02°, a step time of 0.50 s and a Cu K α X-ray source ($\lambda = 1.5418 \text{ \AA}$).

3.2.4 TEM

TEM imaging was performed using a JOEL JEM 2100 microscope with specimen samples prepared by dusting powders onto holey carbon coated Cu grids.

3.2.5 BET

BET measurements were carried out with a Micromeritics Gemini 2375 Surface Area Analyser at 77 K with N₂ used as the adsorbate gas.

3.2.6 Electrochemical characterisation

Electrochemical characterisation was carried out in N₂ purged 0.5 M H₂SO₄ at room temperature using an Autolab PGSTAT30 potentiostat. Thin film catalyst layers on glassy carbon electrodes prepared from catalyst inks were used as the working electrode in the RDE cell. Pt gauze was used as the counter electrode and an MMS electrode (0.69 V vs. RHE) as the reference electrode.

Chapter 3: Mixed iridium-ruthenium oxide electrocatalysts for O_2 evolution

3.2.6.1 Cyclic voltammetry

Cyclic voltammograms were recorded between 0.00 and 1.40 V vs. RHE at a sweep rate of 20 mV s^{-1} with the electrode stationary. Voltammetric charge experiments were recorded between 0.40 and 1.40 V vs. RHE at sweep rates of 2, 5, 10, 20, 30, 40, 50, 60, 80, 100, 150, 200, 300 and 500 mV s^{-1} , and were performed by Emma Barley (University of Southampton).

3.2.6.2 Steady state polarisation

Steady state polarisation was carried out between 1.00 and 1.70 V vs. RHE at a sweep rate of 1 mV s^{-1} . The working electrode was rotated at 900 rpm throughout the measurements in order to remove trapped O_2 bubbles from the surface of the electrode.

3.2.6.3 PEM electrolyser tests

Single cell PEM electrolyser tests were performed using the PEM electrolyser cell described in Chapter 2, section 2.4.2.2. Tests were carried out using Nafion 115 CCM's with the $\text{Ir}_x\text{Ru}_y\text{O}_2$ samples as the anode catalyst and Pt black as the cathode catalyst. The active area of each electrode was 8 cm^2 . Tests were carried out with type 1 water supplied to the anode and cathode at $60 \text{ }^\circ\text{C}$ and a flow rate of 40 mL min^{-1} . The cell was pressurised to 20 bar by blowing compressed air into the back sides of both the anode and cathode. Prior to testing, the cells were held at 1 A cm^{-2} for 30 min using an ISO-TECH IPS-603 DC power supply unit with the cell voltage monitored with a digital voltmeter.

3.2.6.3.1 Steady state polarisation curves

Steady state polarisation curves were obtained with a Bio-Logic VMP3 potentiostat coupled to a High Current Booster, with the current stepped every 60 s from 8.00 to 0.05 A.

3.2.6.3.2 Stability test

The stability of the electrolyser cells was examined using an ISO-TECH IPS-603 DC power supply unit with the cell voltage monitored and recorded every 5 min with a digital voltmeter. The cells were held at constant current of 8.00 A (current density 1.00 A cm^{-2}) for the duration of the test period.

3.2.7 XANES

XANES measurements were carried out on B18, Diamond Light Source, Harwell Science and Innovation Campus, UK. Spectra were collected at both the Ru K edge (22117 eV) and Ir L_3

Chapter 3: Mixed iridium-ruthenium oxide electrocatalysts for O₂ evolution

edge (11215 eV) absorption edges. Higher harmonics were rejected by using a Si(311) crystal monochromator equipped with a Pt coated mirror (Ru K edge) and a Si(111) crystal monochromator with a chromium coated mirror (Ir L₃ edge).

Catalyst electrodes (surface area 1.247 cm²) were prepared as detailed in Chapter 2, section 7.2.5.1. Ex situ measurements were carried out on dry catalyst electrodes. In situ measurements were carried out on the catalyst electrodes in 0.5 M H₂SO₄ using the in situ electrochemical XAS cell as described in Chapter 2, section 7.2.5. Prior to in situ measurements, the catalyst electrodes were hydrated by boiling in water. Once the loaded cell was filled and connected to the potentiostat, three cyclic voltammograms were recorded between 0.00 and 1.40 V vs. RHE at a sweep rate of 50 mV s⁻¹, to ensure that the electrode was fully wetted and connected to the potentiostat. In situ experiments were then carried out with the following procedure:

- Potential swept from open cell voltage to 1.00 V vs. RHE at a sweep rate of 1 mV s⁻¹
- XANES spectra collected
- Potential swept from 1.00 to 1.40 V vs. RHE at a sweep rate of 1 mV s⁻¹
- XANES spectra collected
- Potential swept from 1.40 to 1.70 V vs. RHE at a sweep rate of 1 mV s⁻¹
- XANES spectra collected
- Potential swept from 1.70 to 1.80 V vs. RHE at a sweep rate of 1 mV s⁻¹
- XANES spectra collected
- Potential swept from 1.80 to 1.00 V vs. RHE at a sweep rate of 1 mV s⁻¹
- XANES spectra collected

The measurements were carried out whilst constantly pumping electrolyte solution across the surface of the electrode using a peristaltic pump. The XANES spectra were collected in fluorescence mode with 5-10 scans collected for each potential in order to improve the signal to noise ratio and to check that the sample was not changing throughout the measurement. Due to the positioning of the electrochemical cell, it was not possible to measure reference foils simultaneously with the sample data. Instead, to ensure the monochromator remained stable throughout the measurements, the reference foils were measured periodically.

3.3 Results and discussion

3.3.1 EDX analysis

Elemental analysis of the prepared catalysts was carried out by EDX analysis. The nominal and experimental compositions of the mixed $Ir_xRu_yO_2$ samples are shown in table 1. The experimental compositions are an average of three EDX measurements made on different parts of the sample with the error determined from the standard deviation. The assays of the $Ir_xRu_yO_2$ samples show a good agreement with the nominal values, indicating that the synthesis method was successful in preparing catalysts with the desired Ir/Ru ratio.

Table 1 EDX elemental analysis of the mixed $Ir_xRu_yO_2$ catalyst samples

Sample	Nominal composition / mol %		Experimental composition / mol %	
	Ir	Ru	Ir	Ru
$Ir_{0.75}Ru_{0.25}O_2$	75	25	73 ± 1	27 ± 1
$Ir_{0.5}Ru_{0.5}O_2$	50	50	49 ± 1	51 ± 1
$Ir_{0.25}Ru_{0.75}O_2$	25	75	24 ± 1	76 ± 1

3.3.2 XRD

XRD was used to identify the phases present in the samples and to determine the average crystallite size of the particles. XRD patterns of the $Ir_xRu_yO_2$ samples are presented in figure 1. The peak positions of the IrO_2 (ICSD 84577)²⁶ and RuO_2 (ICSD 172178)²⁷ body-centred tetragonal phases are represented by the vertical solid blue and dashed red lines, respectively. All of the peaks in the XRD patterns of the pure oxide samples IrO_2 and RuO_2 match the tetragonal IrO_2 and/or RuO_2 reference patterns as indexed. No peaks are observed for the metallic phases of Ir or Ru.

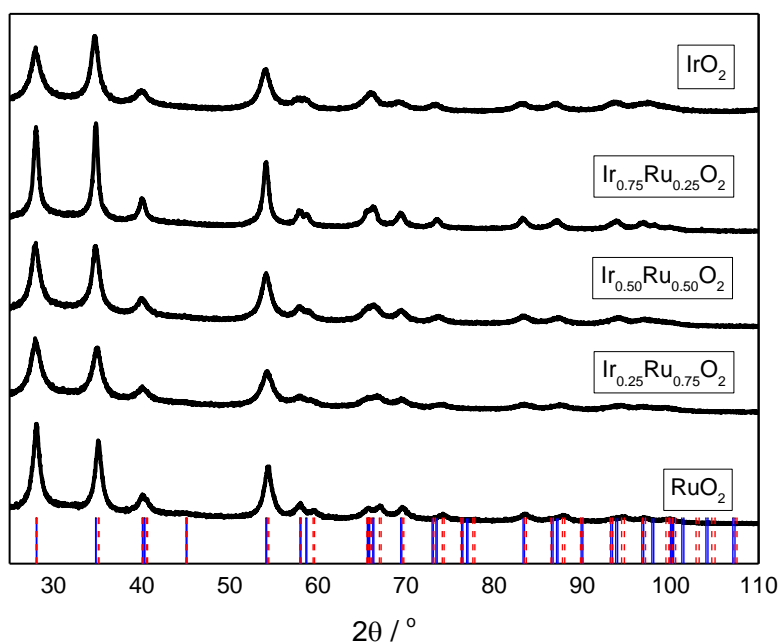


Figure 1 XRD patterns of $Ir_xRu_yO_2$ samples. Peak positions of IrO_2 reference (ICSD 84577)²⁶ are indicated by the blue line. Peak positions of RuO_2 (ICSD 172178)²⁷ are indicated by the dashed red line.

The mixed oxide catalysts have XRD patterns in between of IrO_2 and RuO_2 . The peaks at 2θ values of about 28° , 40° and 70° are similar for all of the catalysts. However the peaks at 35° and 54° and 83° shift with the change in composition from RuO_2 to IrO_2 . Figure 2 highlights the shift of the 101 reflection peaks at $35^\circ 2\theta$ of the $Ir_xRu_yO_2$ catalysts with increasing Ir content. These observations are consistent with IrO_2 and RuO_2 both having reflection peaks at 28° , 40° and 70° , and slightly different values for other peaks. Mixtures of IrO_2 and RuO_2 have been shown to form a single oxide phase over a wide compositional range^{5,8,18} Peak shifts such as those observed are suggestive of the lattice expansion which occurs on forming a solid solution.

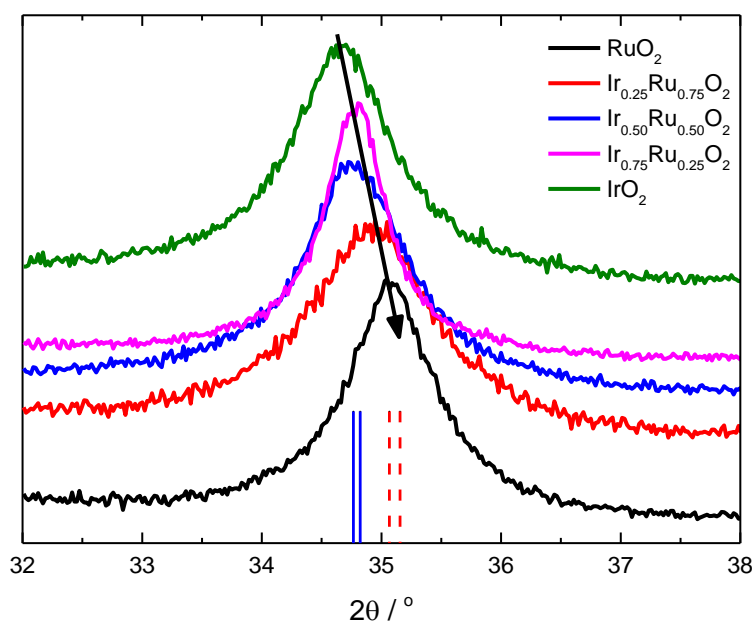


Figure 2 Expanded XRD patterns of $Ir_xRu_yO_2$ samples highlighting the 101 reflection peak. The arrow indicates the shift in the peak position with increasing Ir content. Peak positions of IrO_2 reference (ICSD 84577)²⁶ are indicated by the blue line. Peak positions of RuO_2 (ICSD 172178)²⁷ are indicated by the dashed red line.

The average crystallite size of the $Ir_xRu_yO_2$ catalysts was estimated from the three principal reflection peaks at about 28, 35 and 54° using the Scherrer equation. Table 2 shows that the while the average size of the catalysts is broadly similar across the composition range, the size of the RuO_2 crystallites is slightly larger than the Ir-containing samples. An increase in the average crystallite size has been observed previously for $Ir_xRu_yO_2$ catalysts prepared by the Adams fusion method⁹. The increase was attributed to the lower crystallisation temperature of RuO_2 in comparison to IrO_2 . However the $Ir_{0.75}Ru_{0.25}O_2$ sample is a clear anomaly to this trend as it is approximately twice the size of the rest of the composition range.

Table 2 Crystallite size of $Ir_xRu_yO_2$ catalysts determined from XRD using the Scherrer equation

Sample	Size / nm
IrO_2	6 - 8
$Ir_{0.75}Ru_{0.25}O_2$	12 - 14
$Ir_{0.5}Ru_{0.5}O_2$	7 - 8
$Ir_{0.25}Ru_{0.75}O_2$	5 - 7
RuO_2	9 - 11

3.3.3 TEM

The morphology and particle size of the $Ir_xRu_yO_2$ electrocatalysts was examined by TEM. Micrographs of the $Ir_xRu_yO_2$ samples are shown in figure 3. The scale bar in all images corresponds to 20 nm.

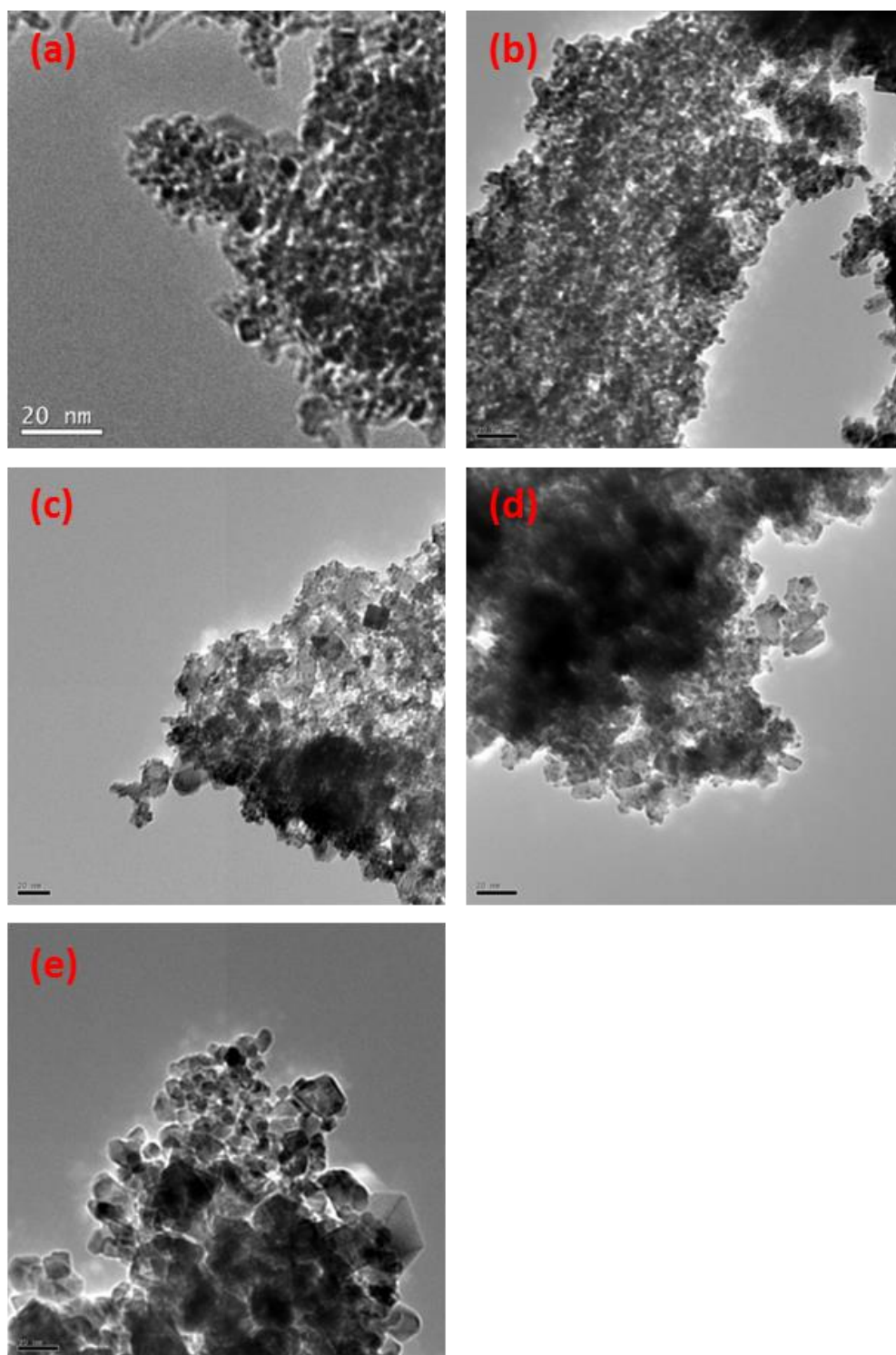


Figure 3 TEM of (a) IrO_2 , (b) $Ir_{0.75}Ru_{0.25}O_2$, (c) $Ir_{0.5}Ru_{0.5}O_2$, (d) $Ir_{0.25}Ru_{0.75}O_2$ and (e) RuO_2 . The scale bar in each image represents 20 nm.

The TEM micrographs show that the $Ir_xRu_yO_2$ samples consist of nano-sized crystallites of irregular, polygonal shapes. The size of the IrO_2 particles are observed to be about 5 – 10 nm, while the RuO_2 has a greater range of sizes of about 5 – 20 nm. The RuO_2 crystallites also have

more defined crystal faces. These observations are likely to be a consequence of RuO₂ crystallising at a lower temperature than IrO₂ which leads to the formation of stoichiometric crystal surfaces with fewer defects, in addition to sintering of the RuO₂ particles at 500 °C^{13,28}. The particle size of the Ir_{0.75}Ru_{0.25}O₂ appears similar to the pure IrO₂, while the TEM of the Ir_{0.50}Ru_{0.50}O₂ and Ir_{0.25}Ru_{0.75}O₂ composites show a greater range of sizes in the range 5 - 20 nm.

The particle sizes observed by TEM are a little larger than the crystallite sizes determined by XRD. There are two explanations for this discrepancy. Firstly, the crystallite size determined by XRD is an average measurement and the range of particle sizes may vary around this value. Secondly, the TEM imaging is complicated by the tendency of the Ir_xRu_yO₂ nanoparticles to agglomerate. This means that the images may not give a reliable representation of the majority of the oxide samples as the smaller particulates are hidden by the larger particles.

3.3.4 BET surface area

The specific surface area of the Ir_xRu_yO₂ catalysts was assessed by BET measurements. The surface areas of the oxides listed in table 3 are similar in magnitude to IrO₂/RuO₂ catalysts reported in other studies²⁹⁻³¹. The measurements show that IrO₂ has a much larger surface area than RuO₂. This may be related to the smaller size of the IrO₂ particles compared to RuO₂ as suggested by the TEM and XRD analysis. It is also possible that the IrO₂ is more porous than the RuO₂, as RuO₂ crystallises at a lower temperature than IrO₂. The surface areas of the mixed catalysts are intermediate of those of the pure oxides.

Table 3 BET surface area of the Ir_xRu_yO₂ catalyst samples

Sample	BET specific surface area / m ² g ⁻¹
IrO ₂	168
Ir _{0.75} Ru _{0.25} O ₂	94
Ir _{0.50} Ru _{0.50} O ₂	110
Ir _{0.25} Ru _{0.75} O ₂	109
RuO ₂	69

3.3.5 Electrochemical characterisation

3.3.5.1 Cyclic voltammetry

Initial electrochemical investigations of the $Ir_xRu_yO_2$ catalysts were performed on thin-film electrodes in 0.5 M H_2SO_4 . The voltammetry is presented normalised to the geometric surface area of the glassy carbon disk (0.1963 cm^2). Figure 4 shows the cyclic voltammetry of the pure oxides, IrO_2 and RuO_2 .

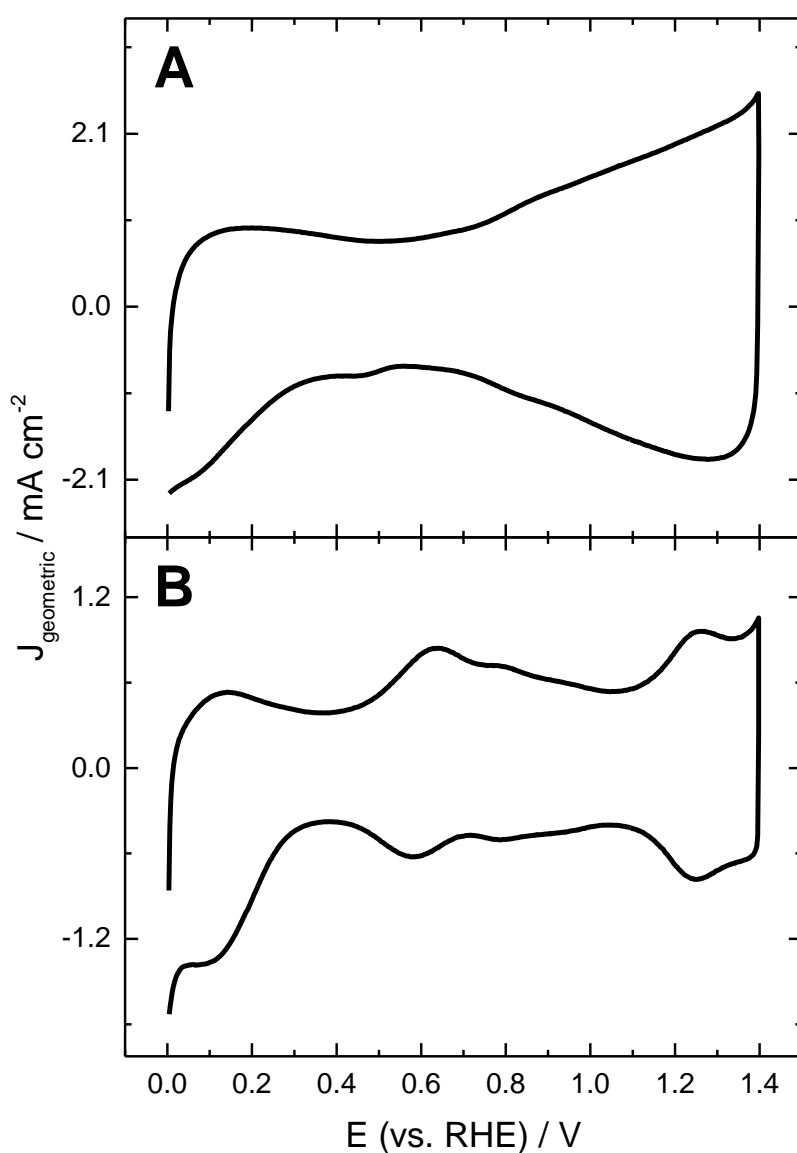


Figure 4 Cyclic voltammetry of IrO_2 (A) and RuO_2 (B) (catalyst loading 0.5 mg cm^{-2}) on a glassy carbon RDE (area 0.1963 cm^2) in 0.5 M H_2SO_4 at 20 mV s^{-1}

Chapter 3: Mixed iridium-ruthenium oxide electrocatalysts for O_2 evolution

The voltammetry in figure 4 is very similar to that previously reported for IrO_2 and RuO_2 catalysts prepared by the Adams fusion method^{9,32} and by other synthesis routes^{4,5,11}. The wide peaks observed in the potential window between 0.40 and 1.40 V of the voltammograms are associated with changes in the surface oxidation state of the Ir and Ru. The large width of these peaks reflects the polycrystalline structure of the samples. For the IrO_2 catalyst (figure 4A) two very wide peaks are observed at about 0.90 V and 1.25 V, which are assigned to the Ir(III)/Ir(IV) and Ir(IV)/Ir(VI) transitions, respectively⁴. Three peaks are observed in the cyclic voltammetry of the RuO_2 catalyst (figure 4B), at about 0.61 V, 0.80 and 1.25 V. These may be attributed to the Ru(II)/Ru(III), Ru(III)/Ru(IV) and Ru(IV)/Ru(VI) transitions, respectively^{33,34}. However other studies have observed only two peaks for RuO_2 at about 0.65 and 1.25 V, which have been assigned to the Ru(III)/Ru(IV) and Ru(IV)/Ru(VI) transitions, respectively^{9,35}. It is possible that the large width of the peaks presented in these other studies may have led to the superimposition of the two distinct redox processes that are observed in this work. The cathodic peak observed between about 0.00 and 0.20 V in the voltammetry of both IrO_2 and RuO_2 is thought to be due to the incorporation of atomic hydrogen within the metal oxide crystal structure, prior to the onset of H_2 evolution that occurs at potentials negative to 0.00 V³⁶.

The voltammograms of the mixed $Ir_xRu_yO_2$ catalysts are shown in figure 5. The curves in this figure exhibit features of both IrO_2 and RuO_2 . The voltammograms of $Ir_{0.75}Ru_{0.25}O_2$ and $Ir_{0.50}Ru_{0.50}O_2$ are more similar to the IrO_2 curve in figure 4 than the RuO_2 , although the $Ir_{0.50}Ru_{0.50}O_2$ curve also shows very slight evidence of the Ru(II)/Ru(III) peak at 0.65 V. The voltammogram of the $Ir_{0.25}Ru_{0.75}O_2$ is more indicative of the RuO_2 catalyst although the peaks are less distinct than that obtained for the pure oxide.

In the literature, the position of the III/IV redox transition peak in the voltammetry of $Ir_xRu_yO_2$ catalysts has been observed to shift with the composition^{7,11}. This potential shift has been interpreted as evidence of an interaction between the Ir and Ru components, either in the bulk of the material or at the surface. The voltammograms of the mixed $Ir_xRu_yO_2$ oxides in figure 5 show a small shift in the position of the III/IV peak, from 0.85 V for $Ir_{0.25}Ru_{0.75}O_2$ to 0.90 V for $Ir_{0.75}Ru_{0.25}O_2$. However the change is very slight and is not conclusive due to the broadness of the peaks. Compared with the voltammetry of sputtered $Ir_xRu_yO_2$ films prepared by Kötter et al., the shift in this work is not as perceptible and the peak potentials do not show a linear dependence on the composition⁷. Previous voltammetry of $Ir_xRu_yO_2$ oxides prepared by the Adams fusion method by Cheng et al. showed no discernible peak shifts with composition⁹. However these samples were prepared by heating in a nitrate melt at 490 °C for 30 min, a

shorter time than the oxide catalysts prepared in this work, which may explain why less pronounced peaks were observed.

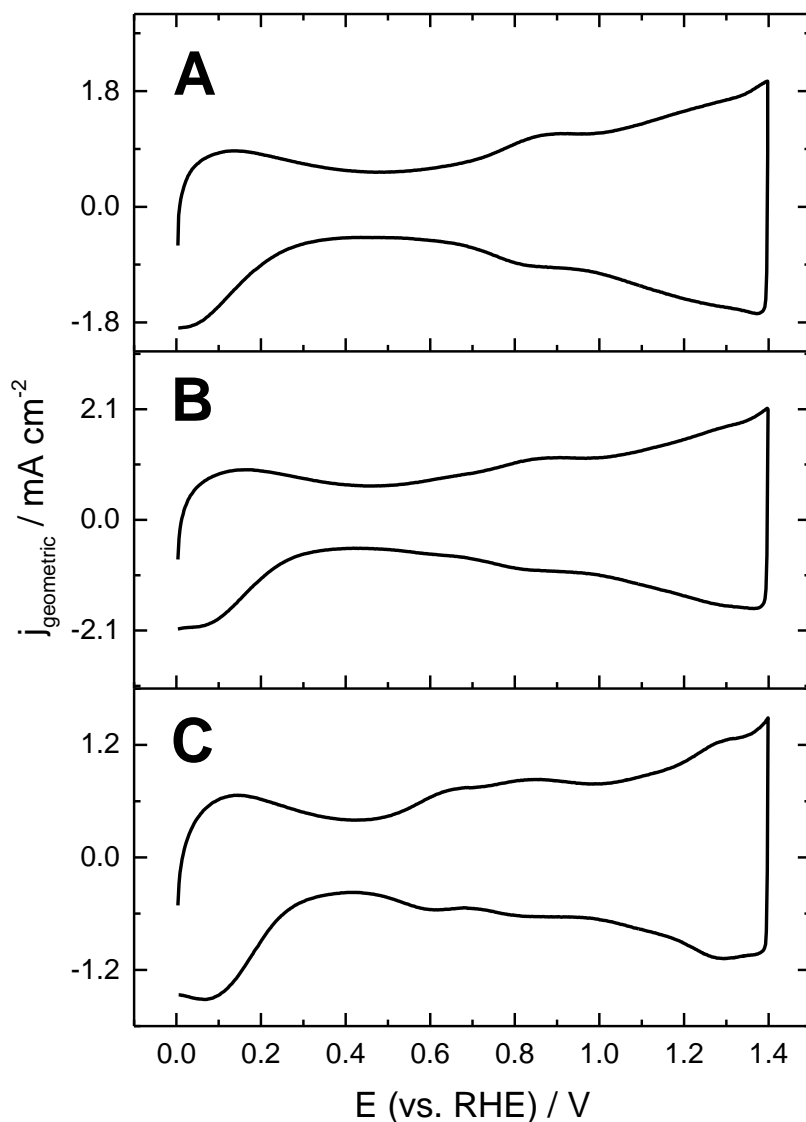


Figure 5 Cyclic voltammetry of (A) $Ir_{0.75}Ru_{0.25}O_2$, (B) $Ir_{0.5}Ru_{0.5}O_2$ and (C) $Ir_{0.25}Ru_{0.75}O_2$ (catalyst loading 0.5 mg cm^{-2}) on a glassy carbon RDE (area 0.1963 cm^2) in $0.5 \text{ M H}_2\text{SO}_4$ at 20 mV s^{-1}

Figure 6 shows the voltammograms of the $Ir_xRu_yO_2$ oxides compared to voltammograms of physical mixtures of the pure IrO_2 and RuO_2 powders in the same molar ratios and prepared as thin film electrodes. Voltammograms of the pure IrO_2 and RuO_2 samples are also include in the figure for reference. The physical mixtures differ from the $Ir_xRu_yO_2$ samples in the order of

magnitude of the mixing. In the $Ir_xRu_yO_2$ composites the mixing of the Ir and Ru in is on the atomic scale, whereas the physical mixtures consist of micro or nano size particulates of the pure oxides. Comparison between the two types of oxide mixtures can give an indication as to whether the observed voltammetric response of the $Ir_xRu_yO_2$ catalysts is due to the formation of common structures or the superimposition of isolated phases⁵.

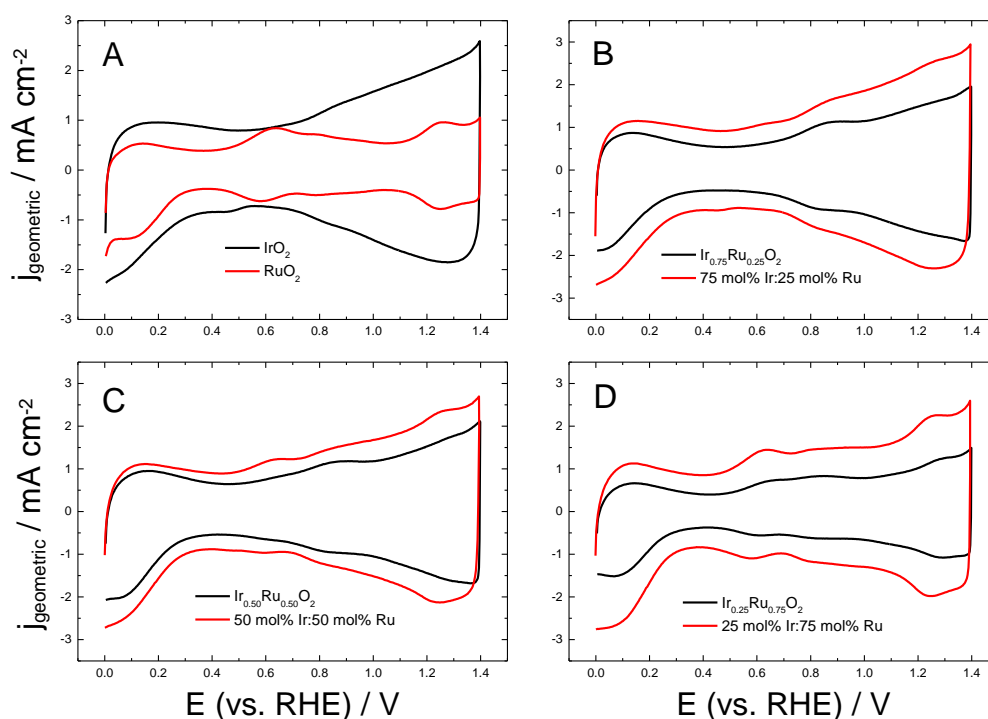


Figure 6 Cyclic voltammograms of (A) IrO_2 (black line) and RuO_2 (red line); (B) $Ir_{0.75}Ru_{0.25}O_2$, (black line) and a physical mixture of 75 mol% Ir:25 mol% Ru (red line); (C) $Ir_{0.50}Ru_{0.50}O_2$ (black line) and a physical mixture of 50 mol% Ir:50 mol% Ru (red line); and (D) $Ir_{0.25}Ru_{0.75}O_2$ (black line) and a physical mixture of 25 mol% Ir:75 mol% Ru (red line). Voltammetry performed in 0.5 M H_2SO_4 at 20 mV s^{-1} . The total catalyst loading was 0.50 mg cm^{-2} .

The voltammetry of both the mixture with 75 mol% Ir: 25 mol% Ru and the mixture with 50 mol% Ir: 50 mol% Ru, strongly resemble the voltammetry of the pure IrO_2 . However there is also clear evidence of the Ru II/III peak at 0.61 V vs. RHE. In contrast, the voltammetry of the sample with 25 mol% Ir: 75 mol% Ru is more characteristic of the pure RuO_2 . Comparison of the voltammetry of the physical mixtures and the $Ir_xRu_yO_2$ composites shows that any differences between the shapes of the curves are small. The voltammograms of the samples with 75 and 50 mol% Ir are very similar, although the Ru II/III peak at 0.61 V is more apparent

Chapter 3: Mixed iridium-ruthenium oxide electrocatalysts for O₂ evolution

in the voltammograms of the physically mixed samples. The voltammograms of the samples with 25 mol% Ir are also similar although the peaks in the physical mixture have greater definition. Similar analysis performed by Owe et al. for Ir_xRu_yO₂ catalysts prepared by a hydrolysis method also found little difference in the voltammetry of composite catalysts and physically mixed powders of the pure oxides⁵. It is also observed that the physical mixtures of the molecular ratios all have a greater capacitance than the corresponding Ir_xRu_yO₂ oxides. This is probably due to the pure IrO₂ having a greater specific surface area than the as prepared mixed oxides, as determined by the BET analysis. This causes the electrode surface area of the physically mixed oxides to be greater than the Ir_xRu_yO₂ oxides, thus increasing the double layer capacitance.

Using the approach outlined in Chapter 2 section 2.1, the voltammetric charge (Q*) of the oxide catalysts in the potential range 0.40 and 1.40 V vs. RHE was determined at various scan rates, in order to provide a measure of the total number of active sites (total charge) and most accessible active sites (outer charge). The number of least assessable sites (inner charge) is calculated by subtracting the outer charge from the inner charge. Figure 7 shows typical voltammograms obtained between 0.40 and 1.40 V vs. RHE at different sweep rates for the IrO₂ sample. The increase in current with potential scan rate (ν) is indicated by the arrow.

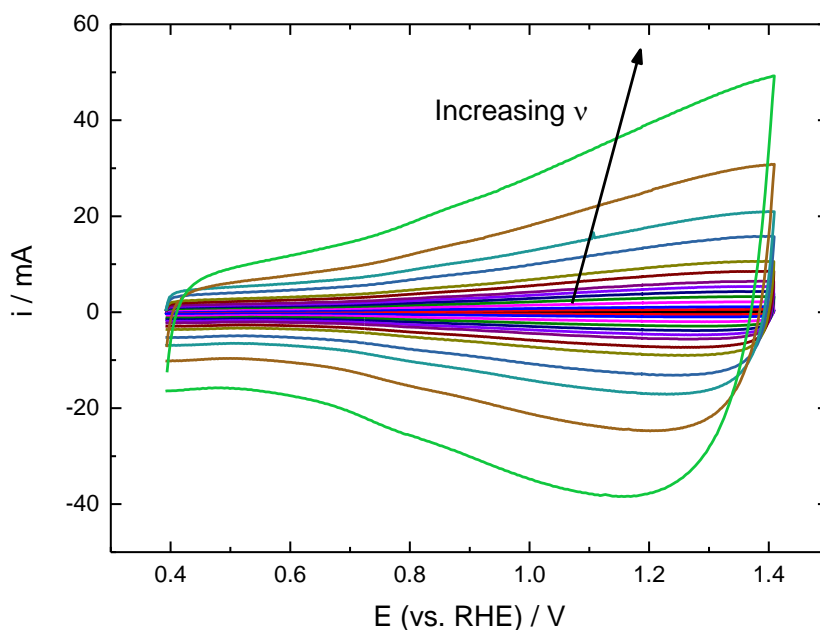


Figure 7 Cyclic voltammetry of IrO_2 (catalyst loading 0.5 mg cm^{-2}) on a glassy carbon RDE (area 0.1963 cm^2) in $0.5 \text{ M H}_2\text{SO}_4$ at variable sweep rates, v . The arrow indicates the effect of the increase sweep rate on the voltametric response

The Q^* was measured from the sum of the anodic and cathodic charges. Figure 8 shows plots of Q^* as a function of the square root of the potential sweep rate of the $Ir_xRu_yO_2$ catalysts, while figure 9 shows plots of the inverse of Q^* as a function of the square root of the sweep rate. Although both plots are satisfactorily linear, there is deviation in linearity at both high and low potential sweep rates. Figure 10 presents the voltammetry of the IrO_2 catalyst normalised by the sweep rate. The normalised voltammetry shows that at low sweep rates deviation from linearity occurs because the anodic O_2 evolution peak and the cathodic wave begin at lower overpotentials and so the Q^* includes some contribution from both of these. Deviation at high scan rates may be due to a combination of distortion of the curves due to uncompensated ohmic resistance and distortion due to some irreversibility of the surface redox transitions³⁷. Nonetheless, comparison between the voltametric charge at a sweep rate of 200 mV s^{-1} and the outer charge as presented in table 4 shows good agreement.

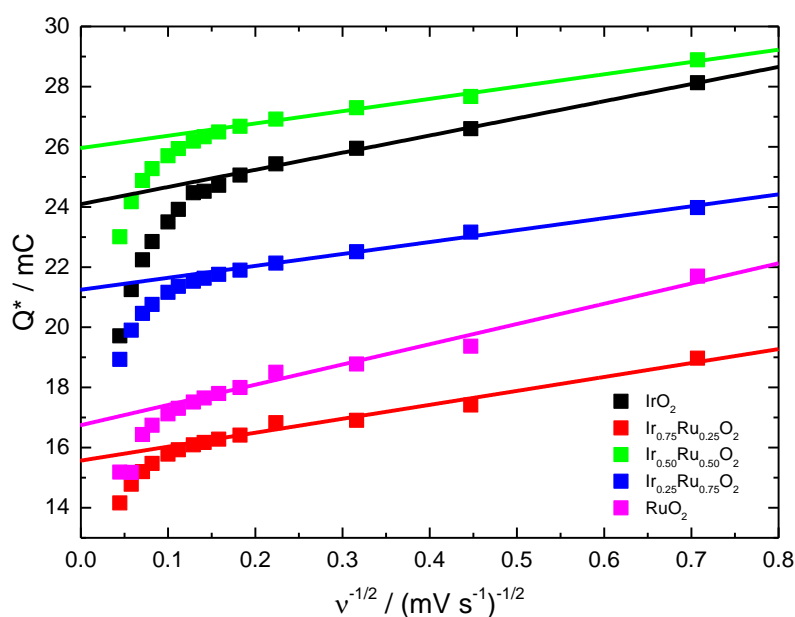


Figure 8 Extrapolation of outer charge from a plot of voltametric charge (Q^*) as a function of the inverse square root of the sweep rate for IrO_2 (black), $\text{Ir}_{0.75}\text{Ru}_{0.25}\text{O}_2$ (red), $\text{Ir}_{0.50}\text{Ru}_{0.50}\text{O}_2$ (green), $\text{Ir}_{0.25}\text{Ru}_{0.75}\text{O}_2$ (blue) and RuO_2 (pink).

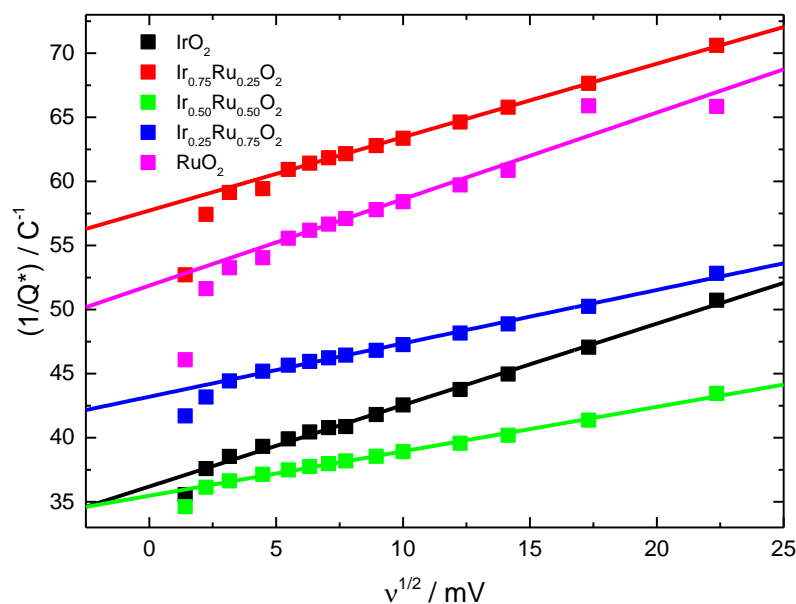


Figure 9 Extrapolation of total charge from a plot of voltametric charge (Q^*) as a function of the inverse square root of the sweep rate for IrO_2 (black), $\text{Ir}_{0.75}\text{Ru}_{0.25}\text{O}_2$ (red), $\text{Ir}_{0.50}\text{Ru}_{0.50}\text{O}_2$ (green), $\text{Ir}_{0.25}\text{Ru}_{0.75}\text{O}_2$ (blue) and RuO_2 (pink)

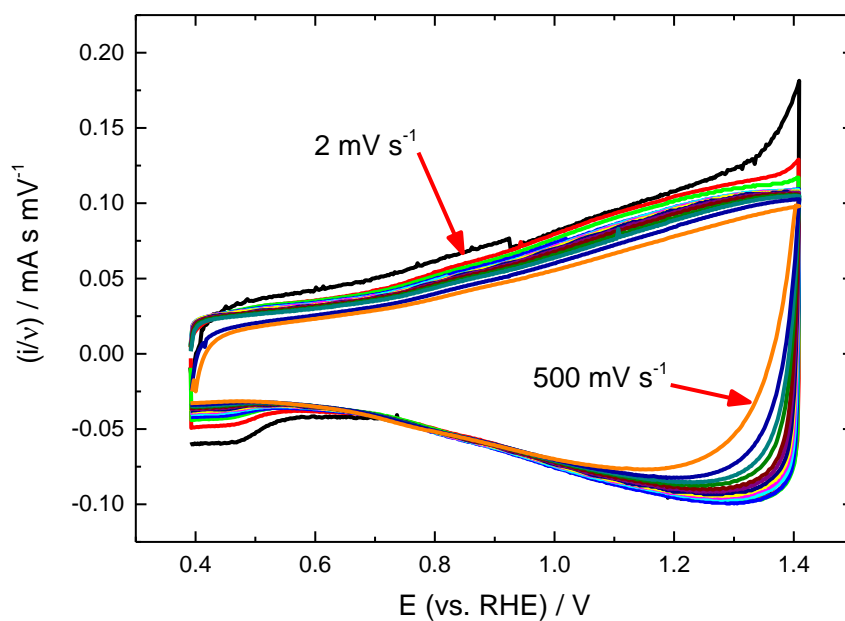


Figure 10 Cyclic voltammetry of IrO_2 (catalyst loading 0.5 mg cm^{-2}) on a glassy carbon RDE (area 0.1963 cm^2) in $0.5 \text{ M H}_2\text{SO}_4$ at variable sweep rates. The voltammetric curves have been normalised by the sweep rate. The voltammetry recorded at 2 mV s^{-1} and 500 mV s^{-1} are highlighted.

Table 4 Outer charge and voltammetric charge measured at 200 mV s^{-1} as a function of Ir mol % of $Ir_xRu_yO_2$ catalysts

Ir mol %	Outer charge / mC	Voltammetric charge at 200 mV s^{-1} / mC
100	24.1 ± 0.2	22.2
75	15.6 ± 0.7	15.2
50	26.0 ± 0.3	24.9
25	21.1 ± 0.3	20.5
0	16.8 ± 0.9	16.4

Chapter 3: Mixed iridium-ruthenium oxide electrocatalysts for O_2 evolution

The total, outer and inner charges of the $Ir_xRu_yO_2$ catalysts as a function of the Ir mol % are presented in figure 11. The plot shows that in general, the Q^*_{total} and Q^*_{outer} increase from RuO_2 with the Ir content, with a maximum observed for the $Ir_{0.50}Ru_{0.50}O_2$ sample. Similar trends have been observed in the literature with $Ir_xRu_yO_2$ catalysts prepared by a variety of methods^{9,20,35}. The increase in active surface area with Ir content may be a reflection of the decrease in particle size as suggested by the TEM and XRD analysis. The trend also correlates with the BET surface area analysis which showed RuO_2 to have the lowest specific surface area. The $Ir_{0.75}Ru_{0.25}O_2$ sample is the obvious anomaly to this trend. This may be a reflection of the larger average crystallite size of this sample as determined by XRD measurements and a decreased specific surface area as suggested by the BET analysis. The inner charge is relatively constant across the composition range.

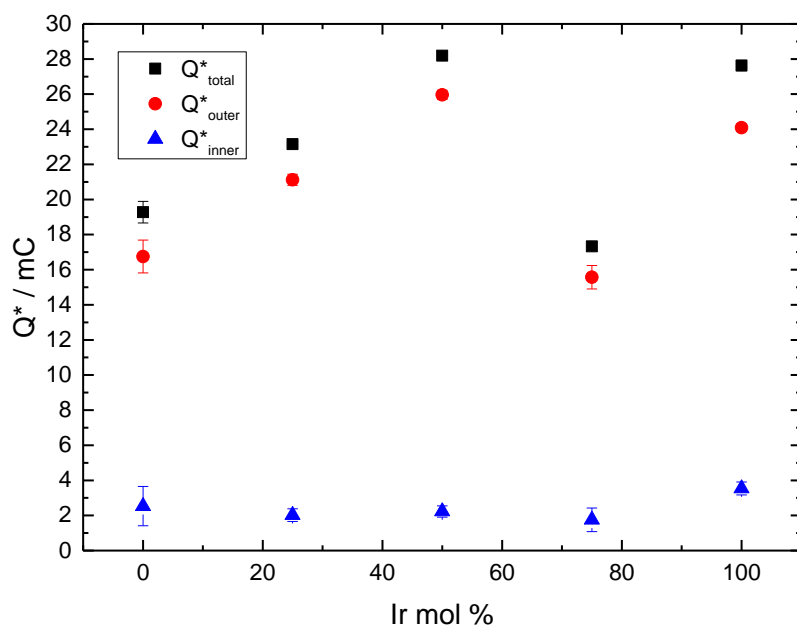


Figure 11 Total charge (black), outer charge (red) and inner charge (blue) as a function of Ir mol % for $Ir_xRu_yO_2$ catalysts

3.3.5.2 Steady state polarisation

The catalytic activity of the $Ir_xRu_yO_2$ catalysts was assessed by performing steady polarisation. Figure 12 shows the polarisation curves for the O_2 evolution on the oxide samples in 0.5 M H_2SO_4 at a sweep rate of 1 mV s^{-1} with the electrode rotating at 900 rpm. RuO_2 is the most active sample with a lower corresponding onset potential of O_2 evolution than the other samples. The onset potential of the catalysts decreases with increasing Ir content, as IrO_2 is less

electrocatalytically active than RuO_2 for the O_2 evolution reaction. The inferior performance of the $Ir_{0.75}Ru_{0.25}O_2$ oxide compared to the IrO_2 is possibly due to the larger particle size of the $Ir_{0.75}Ru_{0.25}O_2$, which would result in fewer active sites. This conclusion is also supported by the diminished charge measurements of the $Ir_{0.75}Ru_{0.25}O_2$ oxide compared to the IrO_2 from the cyclic voltammetry analysis.

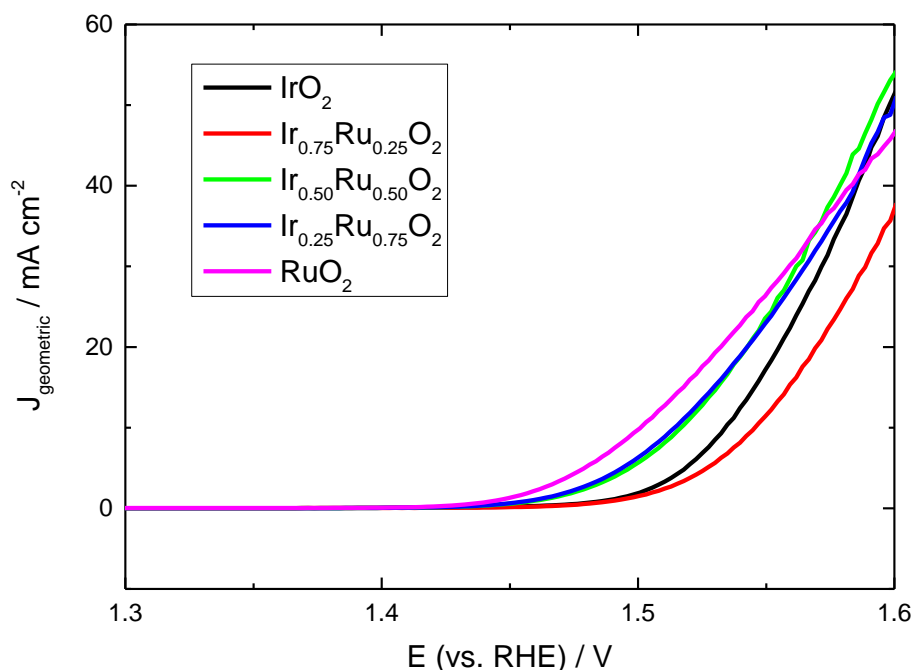


Figure 12 O_2 evolution steady state polarisation of $Ir_xRu_yO_2$ catalysts (catalyst loading 0.5 mg cm^{-2}) in $0.5 \text{ M H}_2\text{SO}_4$ at a sweep rate of 1 mV s^{-1} with the electrode rotating at 900 rpm

To investigate the mechanism of O_2 evolution occurring at the $Ir_xRu_yO_2$ catalysts, Tafel analysis was performed on the experimental polarisation curves. All curves showed deviation from linear Tafel behaviour at high current densities due to uncompensated ohmic resistance associated with the electrolyte and electrode. To correct for this distortion the uncompensated resistance was determined using a method outlined several times in the literature for anodic metal oxides^{5,38-41}. Briefly, uncompensated ohmic resistances were estimated graphically from the experimental data by extending the linear portion of the Tafel curve from the low to high current regions, as shown in figure 13. The deviation of the experimental curve from the straight line, ΔE , was plotted as a function of the corresponding current. Linear plots passing through the origin confirmed that the curvature of the plots was due to ohmic resistance only. An example plot is shown in figure 14. The deviation from linear

Chapter 3: Mixed iridium-ruthenium oxide electrocatalysts for O_2 evolution

behaviour at high potentials in figure 14 is due to gas evolution, which causes the current to be unstable in this region. An example of the correction procedure is given in figure 15 which shows the data before and after the ohmic resistance correction.

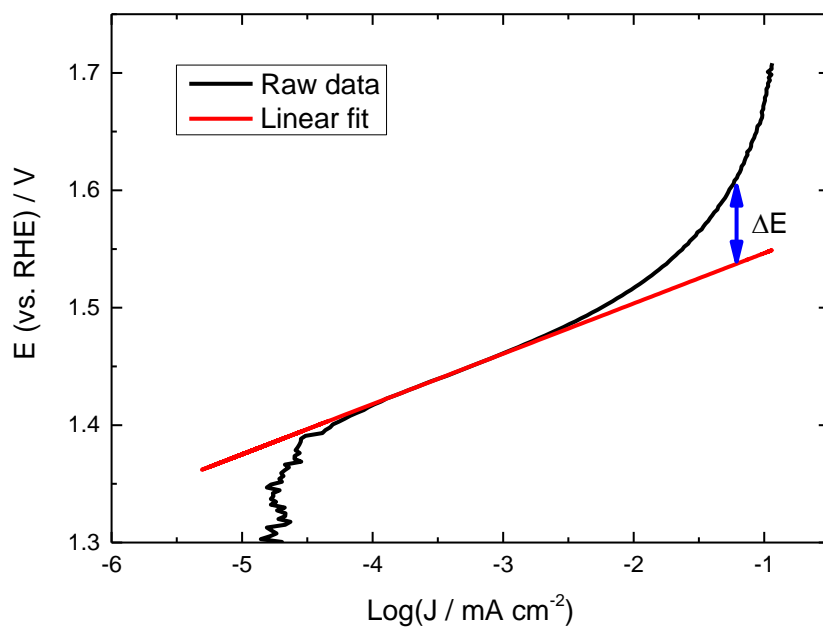


Figure 13 Tafel plot of a $\text{Ir}_{0.5}\text{Ru}_{0.5}\text{O}_2$ catalyst (loading 0.5 mg cm^{-2}) highlighting the extension of the linear region to the high current density region (red line) and the derivation of the experimental curve from the straight line (ΔE)

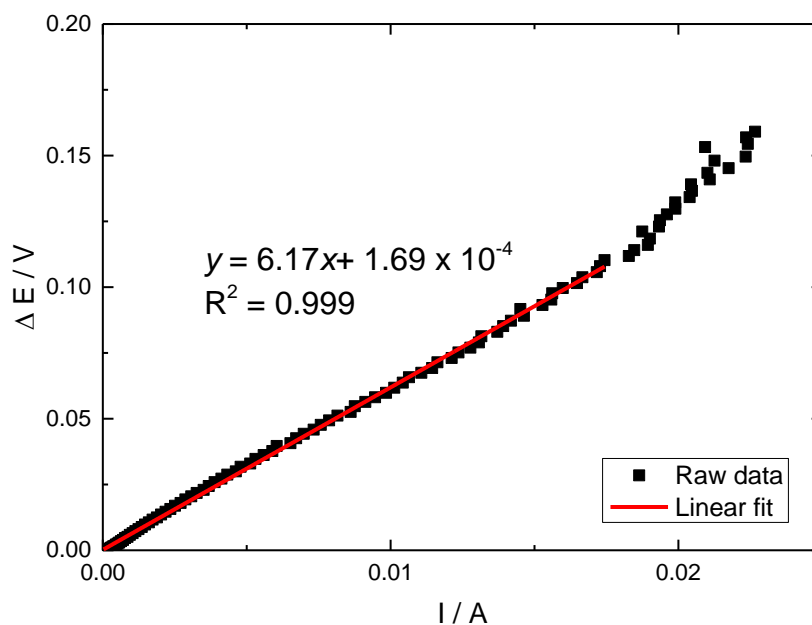


Figure 14 Plot of ΔE vs. I used to estimate the uncompensated resistance of a thin film $Ir_{0.5}Ru_{0.5}O_2$ (catalyst loading 0.5 mg cm^{-2}) catalyst

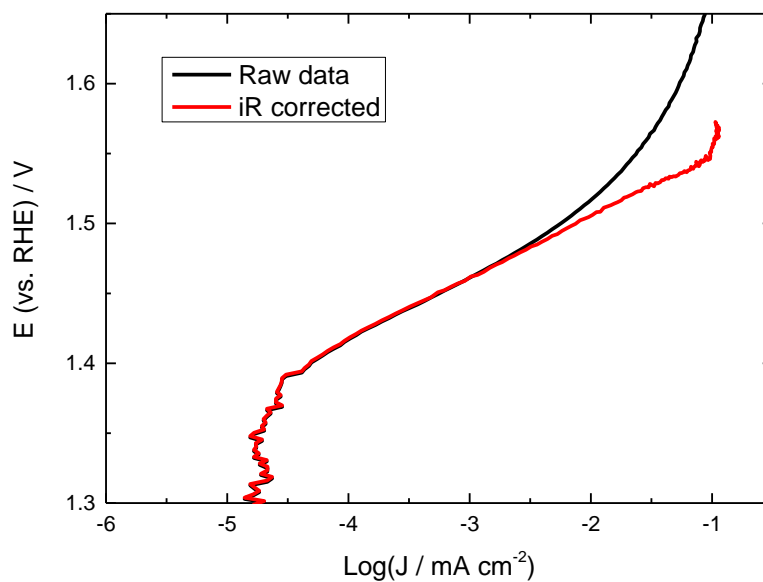


Figure 15 O_2 evolution steady state polarisation of the $Ir_{0.5}Ru_{0.5}O_2$ (loading 0.50 mg cm^{-2}) in $0.5 \text{ M H}_2\text{SO}_4$ at a sweep rate of 1 mV s^{-1} before (black line) and after (red line) iR correction

Chapter 3: Mixed iridium-ruthenium oxide electrocatalysts for O₂ evolution

The measured Tafel slopes of the Ir_xRu_yO₂ catalysts after iR correction are shown in table 5. RuO₂ exhibits the lowest Tafel slope of 36 ± 3 mV dec⁻¹ which corresponds with the high activity of RuO₂ for O₂ evolution. The magnitude of the slope increases from 41 to 45 mV dec⁻¹ with the increasing Ir content of the mixed Ir_xRu_yO₂ catalysts. The slope decreases again to 41 mV dec⁻¹ for the IrO₂ sample. This is in contrast to the change from 40 mV dec⁻¹ for pure RuO₂ to 60 mV dec⁻¹ for pure IrO₂, for samples prepared as thin films by thermal decomposition³², the sol-gel method²³ and reactive sputtering¹. However for Ir_xRu_yO₂ nanoparticles prepared by the Adams fusion⁴² and hydrolysis methods⁵ similar low values for IrO₂ to the one reported in this work, have also been reported. This suggests that the preparation of pure IrO₂ in nanoparticle form produces catalysts that are more active than thin films.

There are several proposed mechanisms for O₂ evolution in acidic media, two of which, the chemical oxide path and the electrochemical oxide path, were detailed in Chapter 1 section 3.3.3.1⁴³. For electrodes with Tafel slopes close to 40 mV dec⁻¹, such as the Ir-containing samples, the slope suggests that the second step of the electrochemical oxide path is rate determining. However in the case of the RuO₂ catalyst it is less clear whether it is the second step of the electrochemical oxide path or the chemical oxide path that is the limiting reaction. As the samples are polycrystalline, it is likely that there are several types of active site at each of which different mechanisms may occur. The measured Tafel slope therefore represents an average of these various active points.

Table 5 Tafel slope for Ir_xRu_yO₂ catalyst samples. The error is determined from three independent repeat measurements at a 95 % confidence limit

Sample	Tafel slope / mV dec ⁻¹
RuO ₂	36 ± 3
Ir _{0.25} Ru _{0.75} O ₂	41 ± 1
Ir _{0.50} Ru _{0.50} O ₂	45 ± 2
Ir _{0.75} Ru _{0.25} O ₂	45 ± 1
IrO ₂	41 ± 2

3.3.6 PEM electrolyser cell tests

The performance of the $Ir_xRu_yO_2$ oxides was assessed in single cell PEM water electrolyzers at 60 °C and 20 bar. Figure 16 shows steady state polarisation curves of the cells with $Ir_xRu_yO_2$ as the anodic catalysts and a Pt black cathode catalyst. The curves have been iR corrected using the cell resistances determined by electrical impedance spectroscopy carried out at 50, 100 and 200 $mA\ cm^{-2}$. The best performance was achieved with the pure RuO_2 oxide, with lower cell potentials measured at every applied current density. The potential of this cell at 1 $A\ cm^{-2}$ was 1.54 V. The performance of the electrolyser cells decreases with increasing Ir content of the $Ir_xRu_yO_2$ catalyst. This reflects the higher activity of Ru than Ir towards the O_2 evolution reaction. The potential of the cell with IrO_2 as the anode at 1 $A\ cm^{-2}$ was 1.63 V.

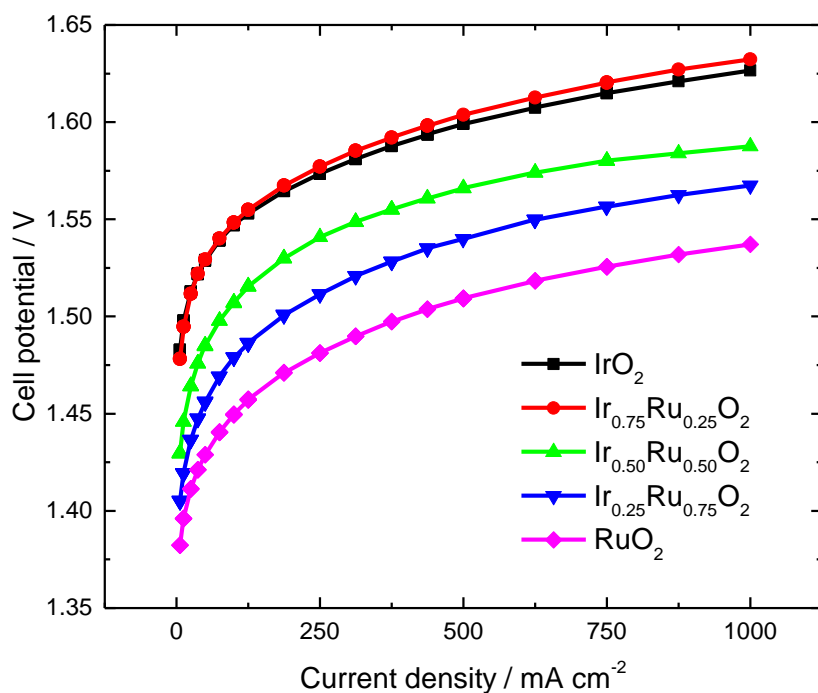


Figure 16 Polarisation curves of single cell PEM electrolyzers at 60 °C and 20 bar with IrO_2 (black squares), $Ir_{0.75}Ru_{0.25}O_2$ (red circles), $Ir_{0.50}Ru_{0.50}O_2$ (green triangles), $Ir_{0.25}Ru_{0.75}O_2$ (blue triangles) and RuO_2 (pink diamonds) as the anode catalysts and Pt black as the cathode catalyst. The catalyst loading at the anode and cathode was 3 $mg\ cm^{-2}$. The curves have been iR corrected using the cell resistances determined by electrical impedance spectroscopy at 50, 100 and 200 $mA\ cm^{-2}$.

Chapter 3: Mixed iridium-ruthenium oxide electrocatalysts for O₂ evolution

The stability of the single cell PEM electrolyzers was assessed by monitoring the change in cell voltage at a constant current density of 1 A cm⁻² for a period of 700 h. The cell potential vs. time curves of the cells with the Ir_xRu_yO₂ oxides as the anodic catalysts are presented in figure 17. The decrease in the cell potential over the first 50 – 100 h observed for all cells is due to the various cell components such as the membrane and catalyst layers, becoming more hydrated and conductive. The cell with the Ir_{0.75}Ru_{0.25}O₂ catalyst developed a catastrophic leak after about 350 h, and had to be removed from the test. The voltage spikes of the cells with Ir_{0.25}Ru_{0.75}O₂ and with Ir_{0.50}Ru_{0.50}O₂ at 350 h and 400 h respectively, were due to short periods when the cells had to be turned off due to unscheduled maintenance of the water supply system.

Figure 17 shows that the cell voltage with RuO₂ is stable at about 1.70 V until 250 h after which it starts to rise, with a fairly rapid increase observed over the final 100 h. This result indicates the instability of RuO₂ for the O₂ evolution reaction in PEM electrolyzers. Had the test continued for a longer time, it is predicted that the cell voltage would have continued to increase rapidly. In contrast, the cell voltage with IrO₂ remains stable at 1.81 V over the entire 700 h test period. The curves of the composite Ir_xRu_yO₂ oxides show that the addition of IrO₂ improves the stability of the catalyst. The cell voltage with Ir_{0.25}Ru_{0.75}O₂ displays a very gradual voltage rise from 1.78 after 100 h to 1.80 at 700. In comparison the cells with Ir_{0.50}Ru_{0.50}O₂ and Ir_{0.75}Ru_{0.25}O₂ both show similar stability to the IrO₂

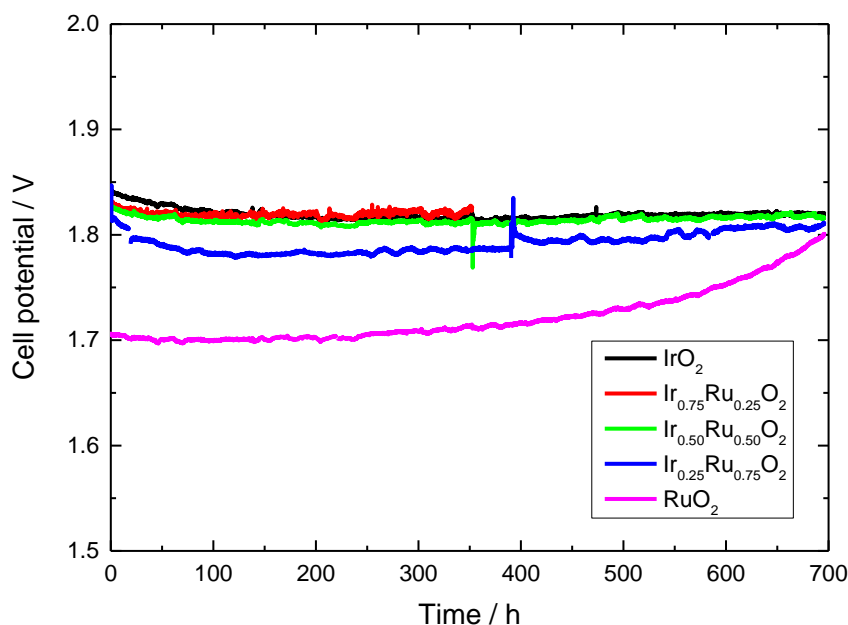


Figure 17 Cell potential vs. time curves of single cell PEM electrolyzers at 60 °C and 20 bar with IrO_2 (black line), $\text{Ir}_{0.75}\text{Ru}_{0.25}\text{O}_2$ (red line), $\text{Ir}_{0.50}\text{Ru}_{0.50}\text{O}_2$ (green line), $\text{Ir}_{0.25}\text{Ru}_{0.75}\text{O}_2$ (blue line) and RuO_2 (pink line) as the anode catalysts and Pt black as the cathode catalyst. The catalyst loading at the anode and cathode was 3 mg cm^{-2} .

3.3.7 XANES analysis

The average oxidation state of the Ir and the Ru in the $\text{Ir}_x\text{Ru}_y\text{O}_2$ catalysts as a function of the applied potential was investigated by in situ XANES measurements. Prior to collecting XANES spectra, cyclic voltammograms of the catalysts in the in-situ electrochemical cell were collected at 50 mV s^{-1} . The voltammograms in figure 18 show that all of the oxides display similar profiles to the voltammetry obtained with the thin film RDE experiments. The voltammograms also show a small amount of distortion due to uncompensated ohmic resistance. This is most likely due to the non-ideal geometry of the in situ cell.

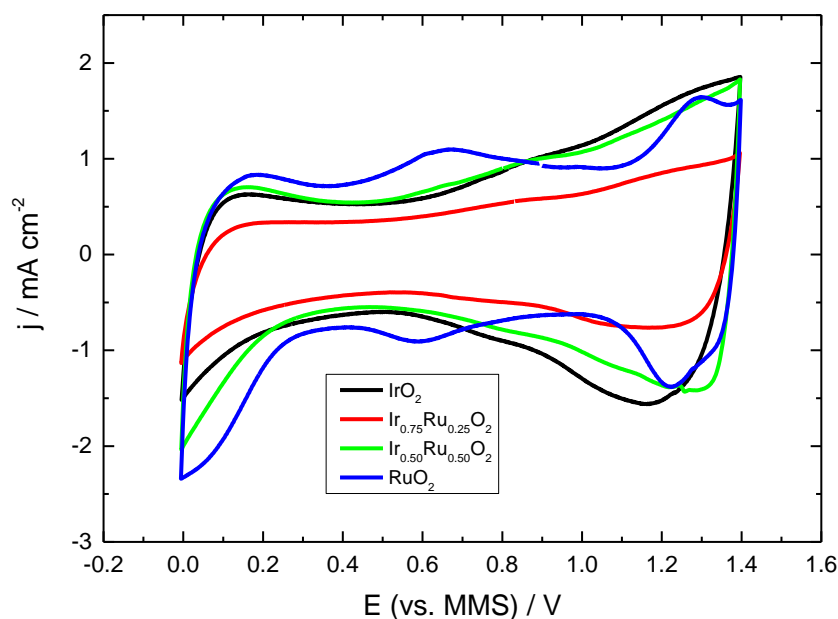


Figure 18 Cyclic voltammetry of the IrO_2 (black), $\text{Ir}_{0.75}\text{Ru}_{0.25}\text{O}_2$ (red), $\text{Ir}_{0.50}\text{Ru}_{0.50}\text{O}_2$ (green) and RuO_2 (blue) catalyst button electrodes in the in-situ XAS cell in 0.5 M H_2SO_4 at 50 mV s^{-1}

3.3.7.1 Ru K-edge

Ru K edge XANES spectra of the RuO_2 , $\text{Ir}_{0.50}\text{Ru}_{0.50}\text{O}_2$ and $\text{Ir}_{0.75}\text{Ru}_{0.25}\text{O}_2$ catalysts are presented in figures 19 through 21. XANES of the RuO_2 sample for a second time at 1.0 V vs. RHE was not possible due to severe degradation of the electrode after the potential hold at 1.8 V. This observation does however highlight the instability of RuO_2 catalysts at O_2 evolution potentials. The position of the Ru K edge was determined at 50 % of the edge step. Figure 22 shows the energy shift of the Ru K edge position of the $\text{Ir}_x\text{Ru}_y\text{O}_2$ catalysts from $\text{Ru}^0 E_0$ (22117 eV), as a function of the applied potential.

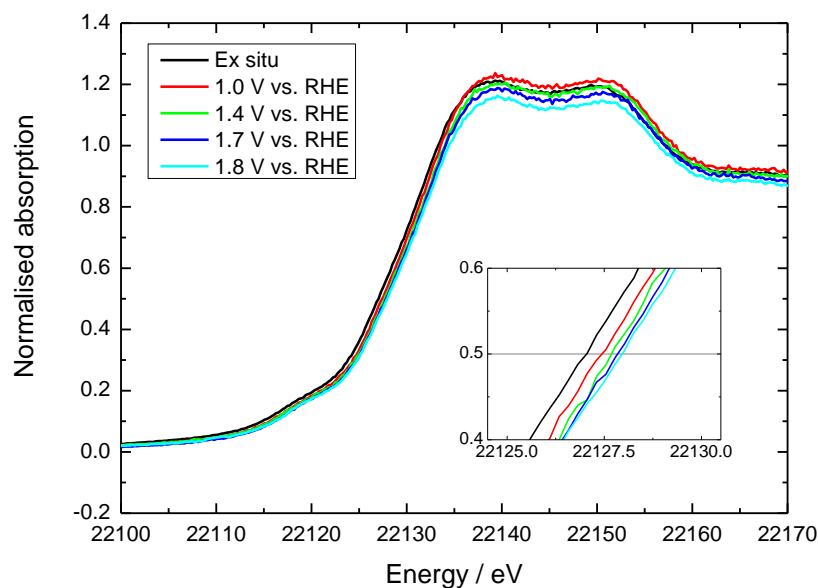


Figure 19 Ru K XANES of RuO_2 recorded ex situ (black line) and in situ at a potential of 1.0 (red line), 1.4 (green line), 1.7 (purple line) and 1.8 V (cyan line) vs. RHE. Insert shows the edge position as determined at 50 % of the edge step

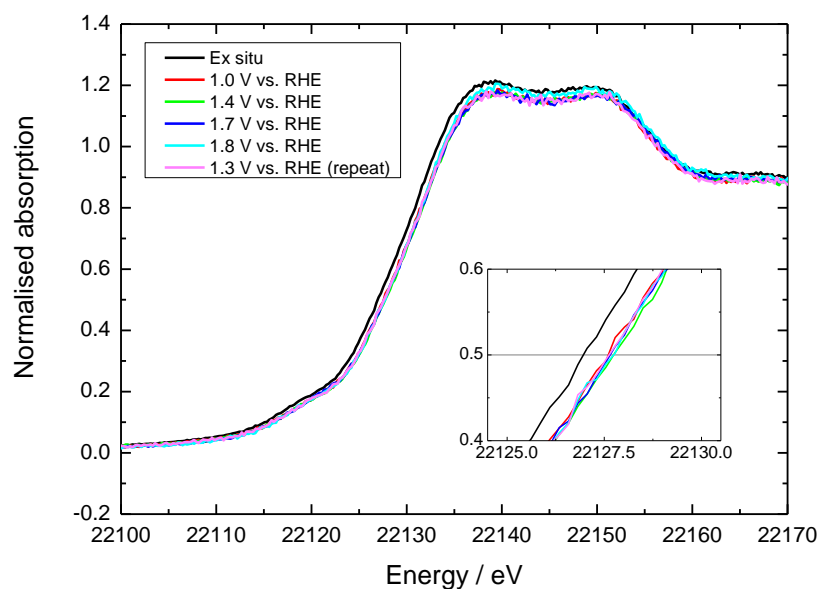


Figure 20 Ru K XANES of $Ir_{0.50}Ru_{0.50}O_{21}$ recorded ex situ (black line) and in situ at a potential of 1.0 (red line), 1.4 (green line), 1.7 (purple line), 1.8 (cyan line) and 1.0 V (repeat) (pink line) vs. RHE. Insert shows the edge position as determined at 50 % of the edge step

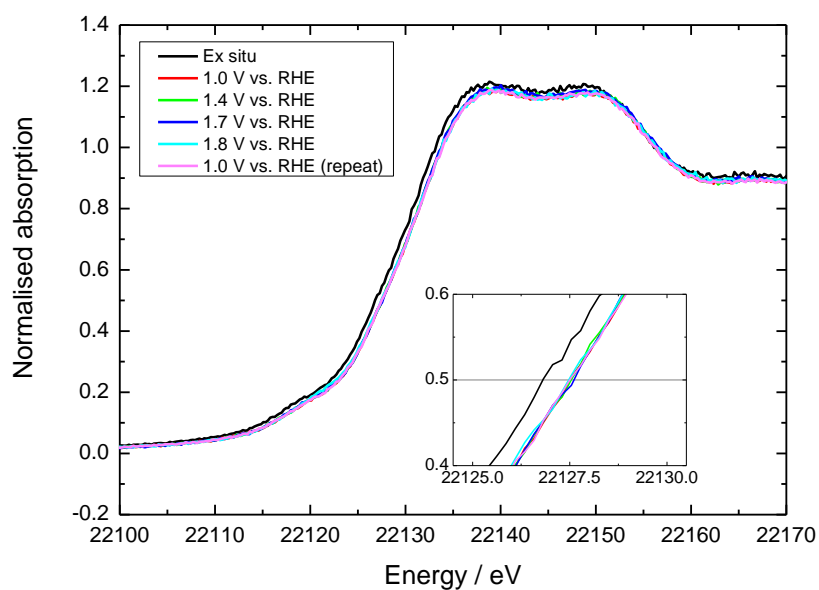


Figure 21 Ru K XANES of $Ir_{0.75}Ru_{0.25}O_2$ recorded ex situ (black line) and in situ at a potential of 1.0 (red line), 1.4 (green line), 1.7 (purple line), 1.8 (cyan line) and 1.0 V (repeat) (pink line) vs. RHE. Insert shows the edge position as determined at 50 % of the edge step

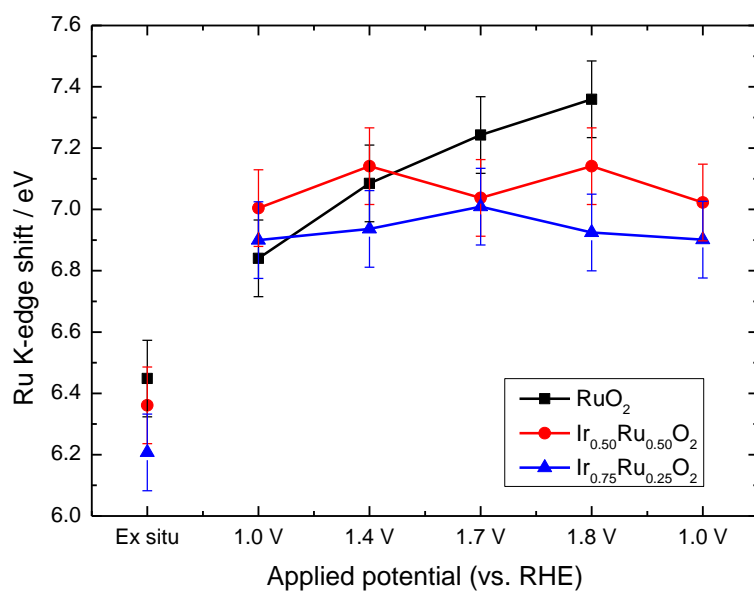


Figure 22 Ru K-edge energy shifts of RuO_2 (black), $Ir_{0.50}Ru_{0.50}O_2$ (red) and $Ir_{0.75}Ru_{0.25}O_2$ (blue) as a function of the applied potential

Chapter 3: Mixed iridium-ruthenium oxide electrocatalysts for O_2 evolution

The Ru K edge XANES of the catalysts in figures 19 through 21 show that the profile of the spectra do not change significantly from the ex situ to the in situ measurements. This suggests that the local environment of the Ru in the oxide structures is similar, irrespective of the electrolyte or electrode potential. However the spectra in addition to the plot of Ru K edge energy shift as a function of potential in figure 22 show that the position of the edge shifts to higher energies when the electrode is immersed in acid and held at potential. This indicates that the oxidation state of the Ru increases. This is as expected due to the known Ru II/III and III/IV transitions that occur at potentials around 0.60 – 0.90 V vs. RHE, as indicated by the cyclic voltammetry. It is also apparent that the edge energy shift of the RuO_2 catalyst continues to increase with the applied potential in O_2 evolution reaction region, whereas the shift of the composite catalysts is much less. This suggests that the oxidation state of the Ru is higher during O_2 evolution than the mixed $Ir_xRu_yO_2$ oxides. It is suggested that this indicates a stabilising effect of the Ir on the Ru as the Ir prevents the Ru from being oxidised to volatile higher states. Furthermore, the energy shift of the $Ir_{0.75}Ru_{0.25}O_2$ catalyst is slightly less than the $Ir_{0.50}Ru_{0.50}O_2$, which suggests that the stabilising effect increases with Ir content. These observations support the theory of the formation of a common valence band structure as suggested by Kötzt et al., which prevents the oxidation of Ru into the VIII state⁷.

To determine the actual Ru oxidation state as a function of potential, the XANES spectra of a number of Ru reference compounds with known oxidation states, were measured as dry powders. The reference samples were provided by Prof. Richard Walton (University of Warwick)⁴⁴. These spectra are presented in figure 23. To calculate the Ru oxidation state of the $Ir_xRu_yO_2$ catalysts, the Ru K edge position of the reference samples was plotted as a function of oxidation state and a calibration curve fitted to the data. Table 6 and figure 24 show the Ru K edge positions of the reference samples as a function of formal oxidation state. The error in the energy position was determined by the resolution of the XAS step size, which was 0.25 eV. Table 7 presents the oxidation states of the $Ir_xRu_yO_2$ catalysts determined from the calibration curve, as a function of applied potential.

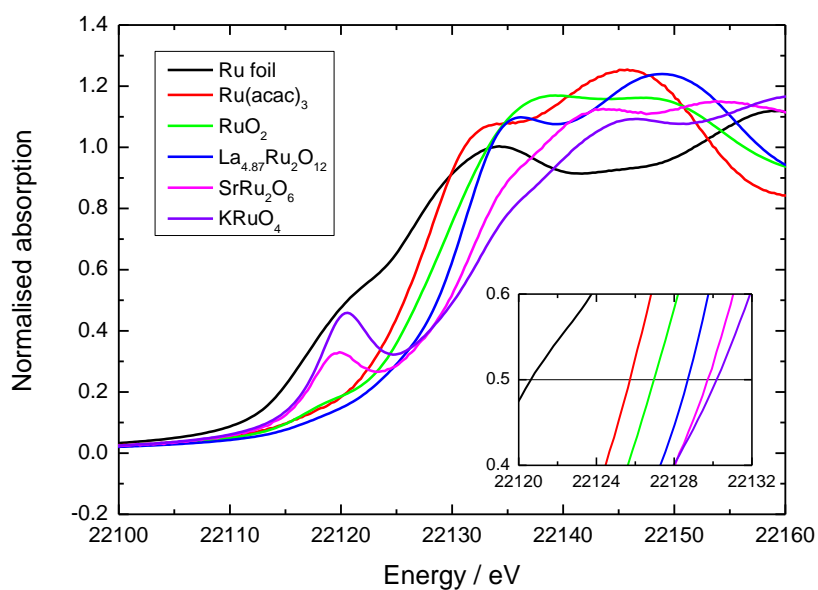


Figure 23 Ru K-edge XANES of Ru foil (black line), Ru(acac)₃ (red line), RuO₂ (green line), La_{4.87}Ru₂O₁₂ (blue line), SrRu₂O₆ (magenta line) and KRuO₄ (violet line) reference materials. The insert shows an expanded region of the XANES spectra, highlighting the 50 % of edge step from which the edge energy was defined.

Table 6 Ru K edge energies of Ru oxidation state reference samples

Sample	Formal oxidation state	Ru K edge energy / eV
Ru foil	0	22117.0 ± 0.1
Ru(acac) ₃	3	22122.1 ± 0.1
RuO ₂	4	22123.4 ± 0.1
La _{4.87} Ru ₂ O ₁₂	4.7	22125.1 ± 0.1
SrRuO ₄ ·2H ₂ O	5	22126.1 ± 0.1
KRuO ₄	6	22126.6 ± 0.1

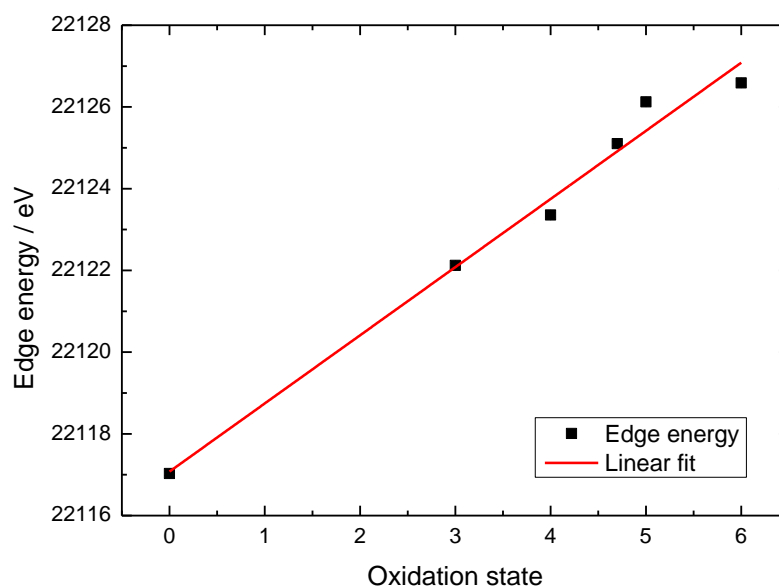


Figure 24 Calibration of Ru K-edge XANES data vs. oxidation state. Error bars are included on the plot but are not visible

Table 7 Calibrated oxidation states of Ir_xRu_yO₂ samples as a function of applied potential

Sample	Oxidation state					
	Ex situ	1.0 V	1.4 V	1.7 V	1.8 V	1.0 V (repeat)
RuO ₂	3.8 ± 0.4	4.1 ± 0.4	4.2 ± 0.4	4.3 ± 0.4	4.4 ± 0.4	-
Ir _{0.50} Ru _{0.50} O ₂	3.8 ± 0.4	4.2 ± 0.4	4.2 ± 0.4	4.2 ± 0.4	4.2 ± 0.4	4.2 ± 0.4
Ir _{0.75} Ru _{0.25} O ₂	3.7 ± 0.4	4.1 ± 0.4	4.1 ± 0.4	4.2 ± 0.4	4.1 ± 0.4	4.1 ± 0.4

Figure 23 shows that the shape of the Ru reference samples spectra is not consistent. The spectra of the SrRuO₄·2H₂O and K₂RuO₄ show a pre-peak at a similar energy to the initial rise in the XANES of the Ru foil. This may suggest the presence of metallic Ru in these samples. Despite this, figure 24 shows a satisfactorily linear relationship between the edge step energy of the Ru absorbing atom and the oxidation state, as has been previously established for Ru and other metals⁴⁵⁻⁴⁷. Table 7 shows that the ex situ oxidation state of the Ru in the Ir_xRu_yO₂

Chapter 3: Mixed iridium-ruthenium oxide electrocatalysts for O_2 evolution

catalysts is around 3.7-3.8, which suggests that the oxides are slightly substoichiometric as dry powders. On immersion in acid and at an applied potential of 1.0 V vs. RHE, the Ru oxidation state increases to 4.1-4.2. This is consistent with the Ru III/IV transition that occurs at about 0.8-0.9 V. At O_2 evolution potentials above 1.4 V, the Ru in the $Ir_xRu_yO_2$ composites remain in the same oxidation state as at 1.0 V, whereas the RuO_2 increases to an oxidation state of 4.4. This is not as high as might be expected based on the model of O_2 evolution on RuO_2 electrodes developed by various authors that involve the generation and subsequent relaxation of Ru VIII species^{2,4}. However as the measured XANES response is an average from all Ru centres in the catalyst materials, it is possible that a lower oxidation state is observed because of a larger number of Ru atoms in the centre of the particles being at a lower oxidation state than Ru at active sites at the surface of the catalysts. It must also be noted that the error in the calibrated oxidation state is large. This is due to the large error in the linear fit of the calibration curve. Absolute confidence in the Ru oxidation state is therefore somewhat limited. To reduce the error it would be beneficial to collect a wider range of Ru reference samples and/or to also independently verify the oxidation state of the reference samples by another technique, such as X-ray photoelectron spectroscopy.

3.3.7.2 Ir L_3 edge

Ir L_3 edge XANES spectra of the IrO_2 , $Ir_{0.50}Ru_{0.50}O_2$ and $Ir_{0.75}Ru_{0.25}O_2$ catalysts are presented in figures 25 through 27. The position of the Ir L_3 edge was defined as the peak maximum of the white line intensity, which was also found to correspond to the second minimum of a plot of the second derivative. Figure 28 shows the energy shift of the Ir L_3 K edge position of the $Ir_xRu_yO_2$ catalysts from $Ir^0 E_0$ (11215 eV), as a function of the applied potential.

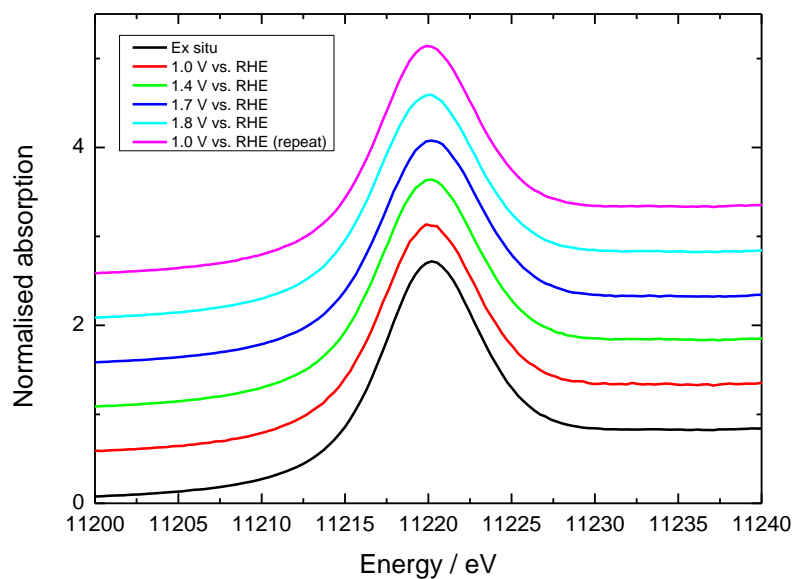


Figure 25 Ir L_3 edge XANES of IrO_2 recorded ex situ (black line) and in situ at a potential of 1.0 (red line), 1.4 (green line), 1.7 (blue line), 1.8 (cyan line) and 1.0 V (repeat) (pink line) vs. RHE.

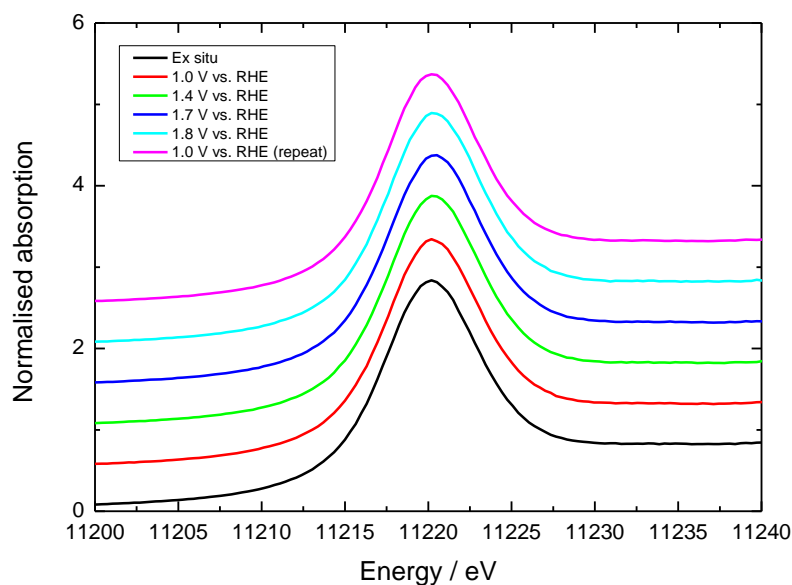


Figure 26 Ir L_3 edge XANES of $Ir_{0.75}Ru_{0.25}O_2$ recorded ex situ (black line) and in situ at a potential of 1.0 (red line), 1.4 (green line), 1.7 (blue line), 1.8 (cyan line) and 1.0 V (repeat) (pink line) vs. RHE.

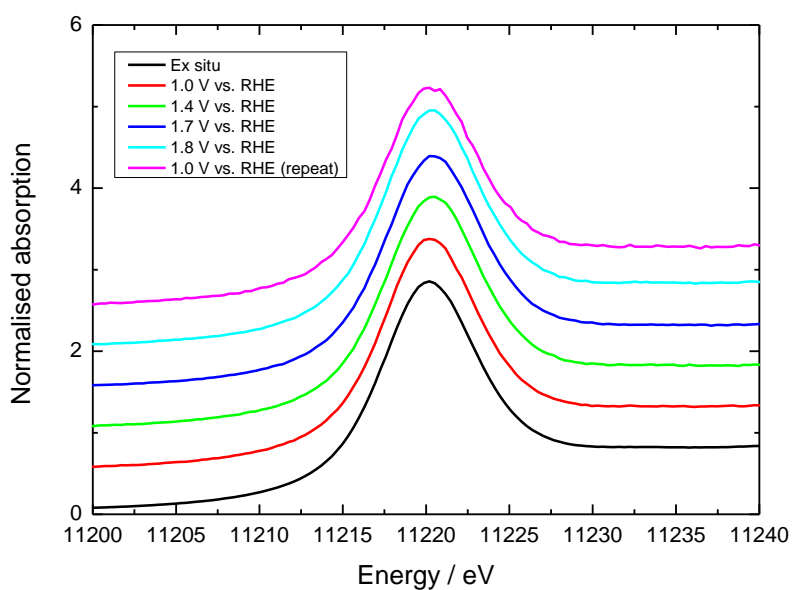


Figure 27 Ir L_3 edge XANES of $Ir_{0.50}Ru_{0.50}O_2$ recorded ex situ (black line) and in situ at a potential of 1.0 (red line), 1.4 (green line), 1.7 (blue line), 1.8 (cyan line) and 1.0 V (repeat) (pink line) vs. RHE.

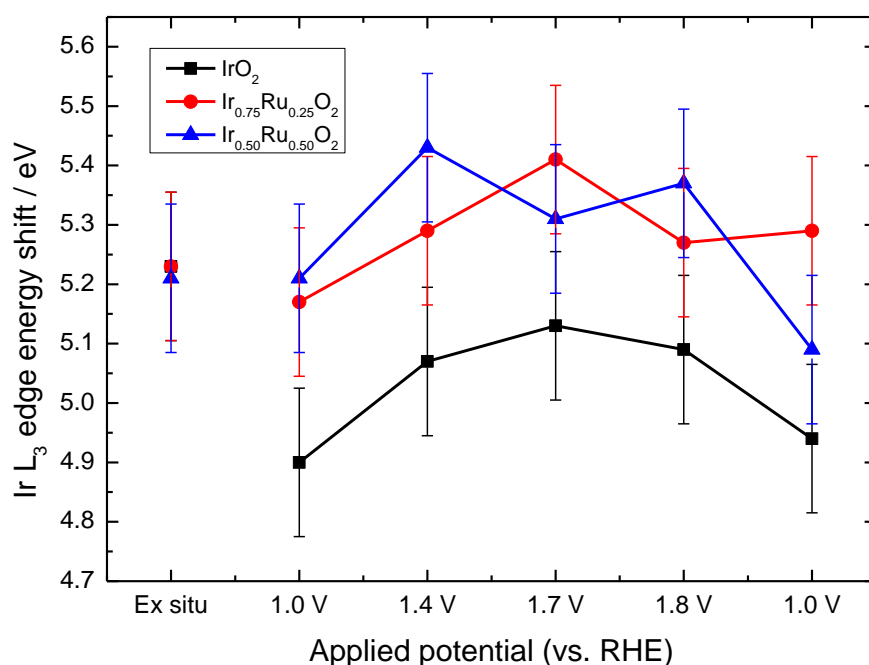


Figure 28 Ir L_3 edge energy shift of IrO_2 (black line), $Ir_{0.75}Ru_{0.25}O_2$ (red line) and $Ir_{0.50}Ru_{0.50}O_2$ (blue line) as a function of the applied potential

Chapter 3: Mixed iridium-ruthenium oxide electrocatalysts for O₂ evolution

The Ir L₃ edge XANES of the catalysts in figures 25 through 27 show that the shape of the curves do not change significantly from the ex situ to the in situ measurements. This suggests that the coordination of the Ir to the surrounding O atoms does not change significantly with the addition of electrolyte or with the change in potential. However the spectra, in addition to the plot of Ir L₃ edge energy shift as a function of potential in figure 28, show that there are slight changes in the position of the white line intensity. The IrO₂ sample shows a marked decrease in the energy shift from the ex situ measurement to the in situ measurement at 1.0 V. This suggests that the Ir in the IrO₂ at 1.0 V is reduced compared to the dry powder. In contrast, the two mixed Ir_xRu_yO₂ samples show no significant shift in the white line position from the ex situ to the in situ measurement. All samples show a shift to higher energies with increasing potential as the oxidation state increases during O₂ evolution.

To determine the actual Ir oxidation state as a function of potential, the XANES spectra of a number of Ir reference compounds with known oxidation states were measured as dry powders. The reference samples were provided by Prof. Richard Walton (University of Warwick). These spectra are presented in figure 29. To calculate the Ir oxidation state of the Ir_xRu_yO₂ catalysts, the Ir L₃ edge position of the reference samples were plotted as a function of oxidation state and a calibration curve fitted to the data. Table 8 and figure 30 show the Ir K edge positions of the reference samples as a function of formal oxidation state. The error in the energy position was determined by the resolution of the XAS step size of 0.25 eV. Table 9 presents the Ir oxidation states of the Ir_xRu_yO₂ catalysts determined from the calibration curve, as a function of applied potential.

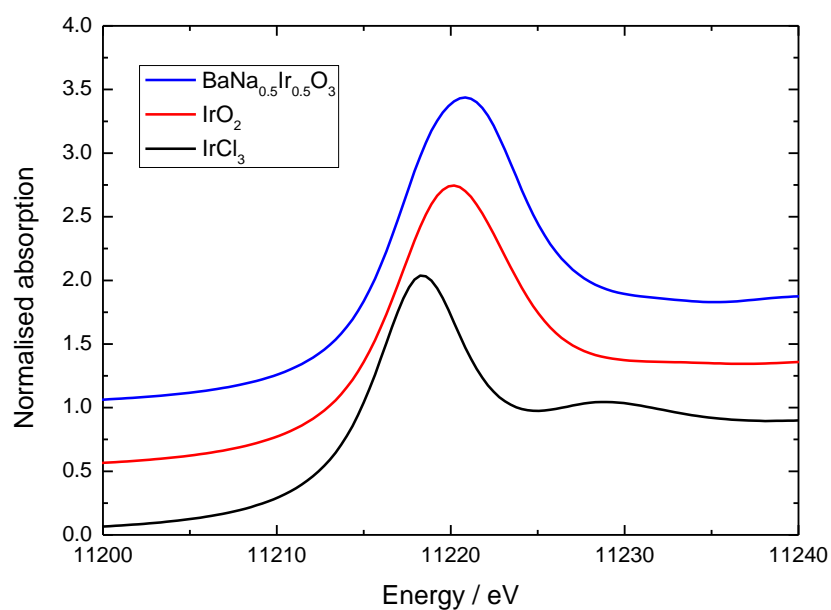


Figure 29 Ir L_3 edge XANES of $IrCl_3$ (black line), IrO_2 (red line) and $BaNa_{0.5}Ir_{0.5}O_3$ (blue line) reference materials.

Table 8 Edge energies of Ir L_3 edge reference samples

Sample	Oxidation state	Ir L_3 edge energy / eV
$IrCl_3$	3	11218.4 ± 0.1
IrO_2	4	11220.1 ± 0.1
$BaNa_{0.5}Ir_{0.5}O_3$	5	11220.8 ± 0.1

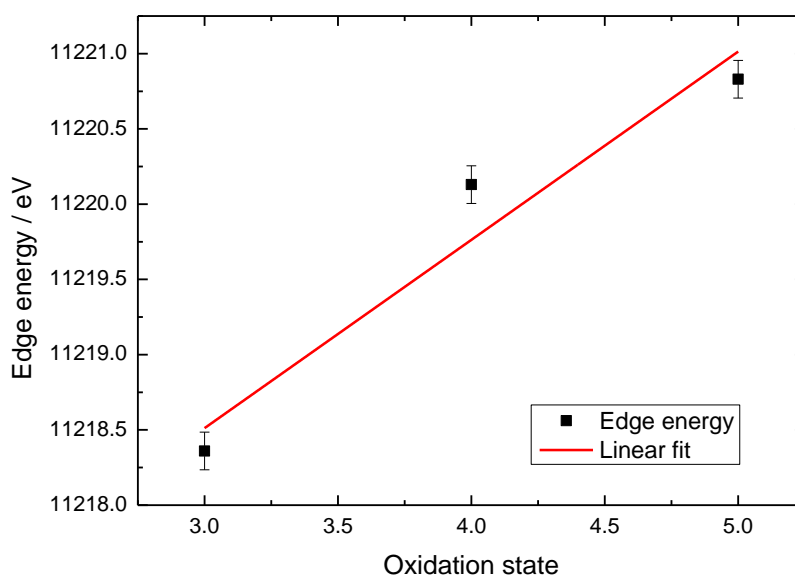


Figure 30 Calibration of Ir L_3 edge XANES data vs. oxidation state

Table 9 Calibrated Ir oxidation states of $Ir_xRu_yO_2$ samples as a function of applied potential

Sample	Oxidation state					
	Ex situ	1.0 V	1.4 V	1.7 V	1.8 V	1.0 V (repeat)
IrO_2	4.4 ± 0.9	4.1 ± 0.8	4.2 ± 0.9	4.3 ± 0.9	4.3 ± 0.9	4.1 ± 0.9
$Ir_{0.75}Ru_{0.25}O_2$	4.4 ± 0.9	4.3 ± 0.9	4.4 ± 0.9	4.5 ± 0.9	4.4 ± 0.9	4.4 ± 0.9
$Ir_{0.50}Ru_{0.50}O_2$	4.4 ± 0.9	4.4 ± 0.9	4.5 ± 0.9	4.4 ± 0.9	4.5 ± 0.9	4.3 ± 0.9

Figure 29 shows the shift in the white line energy with the increase in the Ir oxidation from Ir(III) ($IrCl_3$) to Ir(V) ($BaNa_{0.5}Ir_{0.5}O_3$). Table 8 and figure 30 show that this shift does not show ideal linearity. It is this unsatisfactory linearity that is the cause of the large errors associated with the calibrated Ir oxidation states of the $Ir_xRu_yO_2$ in table 9.

The Ir in all of the dry $Ir_xRu_yO_2$ oxides is in an oxidation state greater than 4. This suggests that there may be some inherent hydration of the Ir species in the $Ir_xRu_yO_2$ catalysts. The data in

Chapter 3: Mixed iridium-ruthenium oxide electrocatalysts for O₂ evolution

table 9 also shows that the oxidation state of the IrO₂ decreases from 4.4 for the ex situ measurement to 4.1 for the in situ measurement. This suggests that the Ir is reduced when immersed in the electrolyte and held at 1.0 V. All samples show a small increase in valency as the potential is increased into the O₂ evolution region however the oxidation states of the composite catalysts are slightly higher than the pure oxide. This may imply that there is the interaction with the Ru component that increases the oxidation state of the Ir centres, thereby enhancing the activity of the catalysts, as observed by the electrochemical studies.

The calibration analysis supports the theory that O₂ evolution proceeds on IrO₂ materials with the Ir in oxidation states > 4 ^{3,4,25}. However the oxidation states are lower than the high valencies that are believed to be key to the O₂ evolution mechanism, such as Ir(VI). It is suggested that this is because at O₂ evolution potentials, the population of oxidised Ir sites is likely to be low. This is due to two reasons. Firstly, the lifetime of any higher oxidation states is likely to be short as it is their inherent instability that leads to the evolution of the O₂. Secondly, as previously demonstrated by Fierro et al.⁴⁸, only a small fraction (1 - 2%) of the Ir is involved in the O₂ evolution reaction, which correspond to the available surface sites. A similar conclusion was reached in a recent study by Minguzzi et al., who developed a fixed energy X-ray absorption voltammetry (FEXRAV) technique to investigate highly hydrated electrodeposited IrO₂ films (EIROF) and IrO₂ nanoparticles prepared by a hydrolysis route⁴⁹. The absorption intensity was measured at a fixed incident X-ray energy, while the electrode potential was swept between 0.2 and 1.4 V vs. RHE at a constant rate. The incident X-rays were set to an energy that corresponded to the white line intensity of a Ir(IV) reference sample. Both samples showed an increase in the absorption intensity as the potential approached 1.0 V vs. RHE, corresponding to the Ir(III)/Ir(IV) transition in the cyclic voltammetry. The X-ray absorbance intensity of the EIROF sample decreased at potentials > 1.0 V, implying a further oxidation that was suggested to be Ir(IV)/Ir(V). In contrast the IrO₂ nanoparticles showed no evidence of a further transition in the Ir in oxidation state, as the absorption intensity remained constant up to 1.4 V.

3.4 Conclusions

In this chapter, a series of Ir_xRu_yO₂ oxides across the composition range have been prepared via the Adams fusion method. XRD indicated that the oxide powders consisted of a single rutile phase with some suggestion of solid solution formation. However definitive evidence of solid solution behaviour is complicated by the overlapping of the very similar diffraction patterns of IrO₂ and RuO₂. TEM and XRD analysis showed that the powders consisted of nanoparticles of around 5 - 20 nm in size.

The addition of Ru to Ir_xRu_yO₂ catalysts modifies the electrochemical response. Cyclic voltammetry in 0.5 M H₂SO₄ showed an increase in the Ru character of the voltammograms with increasing Ru content, although direct evidence of any synergic interactions in the electrochemistry was not as conclusive as the trends observed by Kotz et al⁷. The increase in Ru also caused an increase in the O₂ evolution activity of the Ir_xRu_yO₂ catalysts. The same trend in activity was also observed in the PEM cell. Moreover, the stability of the oxide catalyst in the PEM electrolyser was observed to increase with the addition of Ir to RuO₂.

In situ XANES analysis of the Ir_xRu_yO₂ electrocatalysts was performed as a function of electrode potential. The energy shift in the edge position from the Ru⁰ and Ir⁰ E₀ was used to determine the change in oxidation state with applied potential of the metal oxides. The analysis presented evidence of a direct interaction between the Ir and Ru components at O₂ evolution potentials. Comparison of the Ru K edge shift for RuO₂, Ir_{0.50}Ru_{0.25}O₂ and Ir_{0.75}Ru_{0.25}O₂ catalysts revealed that the Ir has a stabilising effect on the RuO₂ component, preventing the Ru from being oxidised to higher, unstable oxidation states. In contrast, in situ XANES at the Ir L₃ edge showed that the Ir oxidation state remains largely unchanged at O₂ evolution operating potentials. Although the increase in oxidation state from the IrO₂ to the mixed metal oxides suggests that the Ru may increase the activity of the Ir component. Determination of the actual oxidation state of the metal centres was attempted via calibration of the Ir and Ru edge position with a range of reference compounds. Although the error on the estimated values is large, the analysis suggested that O₂ evolution on Ir and Ru oxides occurs with the metals in oxidation states greater than 4, in agreement to what has been proposed previously^{2-4,25}.

3.5 References

- (1) Trasatti, S. *Journal of Electroanalytical Chemistry* **1980**, *111*, 125.
- (2) Kotz, R.; Lewerenz, H. J.; Stucki, S. *Journal of The Electrochemical Society* **1983**, *130*, 825.
- (3) Kotz, R.; Neff, H.; Stucki, S. *Journal of The Electrochemical Society* **1984**, *131*, 72.
- (4) Lyons, M. E. G.; Floquet, S. *Physical Chemistry Chemical Physics* **2011**, *13*, 5314.
- (5) Owe, L.-E.; Tsyppkin, M.; Wallwork, K. S.; Haverkamp, R. G.; Sunde, S. *Electrochimica Acta* **2012**, *70*, 158.
- (6) Mamaca, N.; Mayousse, E.; Arrii-Clacens, S.; Napporn, T. W.; Servat, K.; Guillet, N.; Kokoh, K. B. *Applied Catalysis B: Environmental* **2012**, *111–112*, 376.
- (7) Kötzt, R.; Stucki, S. *Electrochimica Acta* **1986**, *31*, 1311.
- (8) Hutchings, R.; Müller, K.; Kötzt, R.; Stucki, S. *Journal of Materials Science* **1984**, *19*, 3987.
- (9) Cheng, J.; Zhang, H.; Chen, G.; Zhang, Y. *Electrochimica Acta* **2009**, *54*, 6250.
- (10) Song, S.; Zhang, H.; Ma, X.; Shao, Z.; Baker, R. T.; Yi, B. *International Journal of Hydrogen Energy* **2008**, *33*, 4955.
- (11) Kodintsev, I. M.; Trasatti, S.; Rubel, M.; Wieckowski, A.; Kaufher, N. *Langmuir* **1992**, *8*, 283.
- (12) Adams, R.; Shriner, R. L. *Journal of the American Chemical Society* **1923**, *45*, 2171.
- (13) Marshall, A. T.; Sunde, S.; Tsyppkin, M.; Tunold, R. *International Journal of Hydrogen Energy* **2007**, *32*, 2320.
- (14) Marshall, A.; Børresen, B.; Hagen, G.; Tsyppkin, M.; Tunold, R. *Energy* **2007**, *32*, 431.
- (15) Shannon, R. D.; Prewitt, C. T. *Acta Crystallographica Section B* **1969**, *25*, 925.
- (16) Hume-Rothery, W. *Atomic theory for students of metallurgy*; 4th ed.; The Institute of Metals: London, 1962.
- (17) Marshall, A. PhD Thesis, Norwegian University of Science and Technology, 2005.
- (18) Balko, E. N.; Davidson, C. R. *Journal of Inorganic and Nuclear Chemistry* **1980**, *42*, 1778.
- (19) Arikawa, T.; Takasu, Y.; Murakami, Y.; Asakura, K.; Iwasawa, Y. *The Journal of Physical Chemistry B* **1998**, *102*, 3736.
- (20) Angelinetta, C.; Trasatti, S.; Atanososka, L. D.; Atanasoski, R. T. *Journal of Electroanalytical Chemistry and Interfacial Electrochemistry* **1986**, *214*, 535.
- (21) Bestaoui, N.; Prouzet, E. *Chemistry of Materials* **1997**, *9*, 1036.

Chapter 3: Mixed iridium-ruthenium oxide electrocatalysts for O₂ evolution

- (22) McKeown, D. A.; Hagans, P. L.; Carette, L. P. L.; Russell, A. E.; Swider, K. E.; Rolison, D. R. *The Journal of Physical Chemistry B* **1999**, *103*, 4825.
- (23) Pauporté, T.; Aberdam, D.; Hazemann, J.-L.; Faure, R.; Durand, R. *Journal of Electroanalytical Chemistry* **1999**, *465*, 88.
- (24) Mo, Y.; Stefan, I. C.; Cai, W.-B.; Dong, J.; Carey, P.; Scherson, D. A. *The Journal of Physical Chemistry B* **2002**, *106*, 3681.
- (25) Huppaufl, M.; Lengeler, B. *Journal of The Electrochemical Society* **1993**, *140*, 598.
- (26) Bolzan, A. A.; Fong, C.; Kennedy, B. J.; Howard, C. J. *Acta Crystallographica Section B* **1997**, *53*, 373.
- (27) Foo, M. L.; Huang, Q.; Lynn, J. W.; Lee, W.-L.; Klimczuk, T.; Hagemann, I. S.; Ong, N. P.; Cava, R. J. *Journal of Solid State Chemistry* **2006**, *179*, 563.
- (28) Battisti, A. D.; Lodi, G.; Nanni, L.; Battaglin, G.; Benedetti, A. *Canadian Journal of Chemistry* **1997**, *75*, 1759.
- (29) Mayousse, E.; Maillard, F.; Fouda-Onana, F.; Sicardy, O.; Guillet, N. *International Journal of Hydrogen Energy* **2011**, *36*, 10474.
- (30) Cruz, J.; Baglio, V.; Siracusano, S.; Ornelas, R.; Ortiz-Frade, L.; Arriaga, L.; Antonucci, V.; Aricò, A. *Journal of Nanoparticle Research* **2011**, *13*, 1639.
- (31) Cruz, J.; Baglio, V.; Siracusano, S.; Antonucci, V.; Arico, A. S.; Ornelas, R.; Ortiz-Frade, L.; Osorio-Monreal, G.; Duron-Torres, S. M.; Arriaga, L. *International Journal of Electrochemical Science* **2011**, *6*, 6607.
- (32) Xu, J.; Wang, M.; Liu, G.; Li, J.; Wang, X. *Electrochimica Acta* **2011**, *56*, 10223.
- (33) Terezo, A. J.; Pereira, E. C. *Materials Letters* **2002**, *53*, 339.
- (34) Wen, T.-C.; Hu, C.-C. *Journal of The Electrochemical Society* **1992**, *139*, 2158.
- (35) Mattos-Costa, F. I.; de Lima-Neto, P.; Machado, S. A. S.; Avaca, L. A. *Electrochimica Acta* **1998**, *44*, 1515.
- (36) Galizzioli, D.; Tantardini, F.; Trasatti, S. *Journal of Applied Electrochemistry* **1974**, *4*, 57.
- (37) Baronetto, D.; Krstajić, N.; Trasatti, S. *Electrochimica Acta* **1994**, *39*, 2359.
- (38) Da Silva, L. M.; Boodts, J. F. C.; De Faria, L. A. *Electrochimica Acta* **2001**, *46*, 1369.
- (39) Faria, L. A.; Boodts, J. F. C.; Trasatti, S. *Journal of Applied Electrochemistry* **1996**, *26*, 1195.
- (40) De Pauli, C. P.; Trasatti, S. *Journal of Electroanalytical Chemistry* **2002**, *538-539*, 145.
- (41) Shub, D. M.; Reznik, M. F.; Shalaginov, V. V. *Soviet Electrochemistry* **1985**, *21*, 878.
- (42) Rasten, E. PhD Thesis, Norwegian University of Science and Technology, 2001.

Chapter 3: Mixed iridium-ruthenium oxide electrocatalysts for O₂ evolution

- (43) Bockris, J. O. M. *The Journal of Chemical Physics* **1956**, *24*, 817.
- (44) Sardar, K.; Petrucco, E.; Hiley, C. I.; Sharman, J. D. B.; Wells, P. P.; Russell, A. E.; Kashtiban, R. J.; Sloan, J.; Walton, R. I. *Angewandte Chemie* **2014**, *in press*.
- (45) Arčon, I.; Benčan, A.; Kodre, A.; Kosec, M. *X-Ray Spectrometry* **2007**, *36*, 301.
- (46) Pantelouris, A.; Modrow, H.; Pantelouris, M.; Hormes, J.; Reinen, D. *Chemical Physics* **2004**, *300*, 13.
- (47) Wong, J.; Lytle, F. W.; Messmer, R. P.; Maylotte, D. H. *Physical Review B* **1984**, *30*, 5596.
- (48) Fierro, S.; Nagel, T.; Baltruschat, H.; Comninellis, C. *Electrochemistry Communications* **2007**, *9*, 1969.
- (49) Minguzzi, A.; Lugaresi, O.; Locatelli, C.; Rondinini, S.; D'Acapito, F.; Achilli, E.; Ghigna, P. *Analytical Chemistry* **2013**, *85*, 7009.

4. Ir/ITO electrocatalysts for the O₂ evolution reaction

4.1 Introduction

Supporting the active phase on another less expensive material is one approach that can be used to enhance the usage of the precious-metal catalysts. Support materials provide a surface for the dispersal of electrocatalyst particles, facilitating high active surface areas and reduced catalyst loadings. The use of a support in the synthesis of the catalyst may also favour the formation of smaller catalyst particles, as the support provides nucleation sites during the deposition stage of the catalyst precursor. It is also possible for the electrocatalytic characteristics of the active phase to be modified via synergic effects between the catalyst and the support¹.

An ideal support material for an electrocatalyst must have high electronic conductivity and a high surface area. Carbon is one such material and the development of carbon-supported platinum electrocatalysts for the O₂ reduction reaction has allowed significant reductions in Pt loadings for PEM fuel cell cathodes². However carbon is unsuitable as a support for O₂ evolution catalysts, as it corrodes rapidly via equation 1 at the high anodic potentials employed³



A number of metal oxide materials have been proposed as supports for the O₂ evolution reaction, such as TiO₂^{4,5} and SnO₂⁶. However, while TiO₂ and SnO₂ have a good resistance to corrosion, they are also poor electrical conductors⁷. Consequently, high catalyst loadings (≥ 60 wt. % Ir) are required to provide the electron conductive pathways^{4,6}. Lower loadings have however been reported on conductive metal oxide supports, such as substoichiometric metal oxides and doped metal oxides. For example, titanium sub-oxides with the general formula Ti_nO_{2n-1} have been shown to be promising catalyst support materials, with Siracsuno et al. demonstrating the performance of 30 wt. % IrO₂/Ti_nO_{2n-1} in a single cell PEM electrolyser⁸. However Chen et al. found that the long term stability of Ti_nO_{2n-1} supports may be unfavourable as they are oxidised to TiO₂ during extensive polarisation⁹. Niobium-doped titanium oxides (Nb-TiO₂) were instead shown to be as effective support materials as Ti_nO_{2n-1} but significantly more resistant to oxidation. Hu et al. prepared a series of IrO₂/Nb_{0.05}Ti_{0.95}O₂

Chapter 4: Ir/ITO electrocatalysts for the O₂ evolution reaction

catalysts with catalyst loadings from 17 to 33 wt. %¹⁰. It was found that an IrO₂ loading of 26 wt. % gave the optimal performance in terms of mass activity at 1.60 V vs. RHE (471 mA mg⁻¹), which was 2.4 times greater than unsupported IrO₂ (198 mA mg⁻¹).

Antimony-doped tin oxide (ATO) has received significant interest over the last 5 years as a potential support for O₂ evolution catalysts¹¹⁻¹⁷, due to its resistance to corrosion and good electronic conductivity (10¹ – 10² S cm⁻¹)⁷. Marshall et al. prepared 5, 10 and 20 wt. % Ir_xRu_yO₂/ATO catalysts¹⁵. The O₂ evolution performance of the 20 wt. % IrO₂/ATO catalyst in 0.5 mol dm⁻³ H₂SO₄ measured in terms of the voltage observed at 1 mA cm⁻² (1.48 V vs. RHE), was slightly superior to unsupported IrO₂ reported in his earlier work (1.50 V)¹⁸. Thomassen et al. prepared 20 wt. % Ir/ATO and tested its performance as the anode catalyst in a single cell PEM water electrolyser¹¹. A cell voltage of 1.65 V was reported at 1 A cm⁻² using 4 mg cm⁻² 20 wt. % Ir/ATO which corresponds to an Ir loading of 0.8 mg_{Ir} cm⁻². This compares very favourably to typical anode catalyst loadings (about 2 mg_{Ir} cm⁻²)¹⁹. The supported catalyst also showed good stability for 100 h during degradation testing.

Another attractive candidate support material for O₂ evolution catalysts is indium tin oxide (ITO), as it is also resistant to corrosion and has a high electronic conductivity (> 10³ S cm⁻¹)^{20,21}. It is formed by substitutional doping of indium oxide (In₂O₃) by Sn, with the Sn⁴⁺ replacing the In³⁺ atoms in the cubic bixbyite In₂O₃ lattice. The replacement of the In³⁺ by Sn⁴⁺ produces free electrons, which gives rise to the conductivity of the material. Chhina et al. studied a commercial ITO nanopowder (90 % In₂O₃, 10 % SnO₂) as a non-carbon alternative support for PEM fuel cell cathode electrocatalysts and found that 40 wt. % Pt/ITO was electrochemically stable in 1 M H₂SO₄ at potentials up to 1.8 V vs. RHE.²² In very recent work, Puthiyapura et al. published the first use of ITO as a support for O₂ evolution electrocatalysts²³. Samples with IrO₂ loadings from 20 to 90 wt. % were prepared using a modified Adams fusion method²⁴ and tested in a single cell PEM electrolyser at 80 °C. However, only the 90 wt. % IrO₂/ITO gave a comparable performance to unsupported IrO₂ with the performance decreasing significantly with IrO₂ loading. The optimal performance of the 90 wt. % sample was attributed to the better dispersion and lower particle size of the IrO₂ on the ITO observed at the highest loadings. It was hypothesised that the poor performance of the IrO₂/ITO with low loadings was due to agglomeration of the IrO₂ during the catalyst synthesis caused by poor precursor premixing.

In order to achieve more significant reductions in the Ir loading without compromising the catalyst performance, an alternative preparation method may be required. One route commonly used in the preparation of Pt/C fuel cell catalysts is the precipitation impregnation

method, whereby the active phase is precipitated onto the support in an aqueous solvent, by the addition of a reducing agent²⁵. Goodenough et al. demonstrated that this method produces Pt/C catalysts with small crystallites strongly adsorbed to the support²⁶. Goodenough also showed that the highest catalyst activities were obtained from Pt/C prepared by the reduction of the metal precursors with strong reducing agents such as formaldehyde and hydrazine rather than sodium formate. Thus in this work a formaldehyde reduction method has been used to synthesise Ir/ITO catalysts. The Ir/ITO samples have then been characterised, both physically and electrochemically, to assess their suitability as O₂ evolution electrocatalysts in PEM water electrolyzers. The effect of Ir loading on the performance of the catalysts has been examined by preparing catalysts with 5, 10, 20 and 40 wt. % Ir loadings. The effect of the heat treatment of 40 wt. % Ir/ITO in both oxidising and non-oxidising conditions has also been investigated.

4.2 Experimental details

4.2.1 Preparation of supported electrocatalysts by formaldehyde reduction

40, 20, 10 and 5 wt. % Ir was deposited onto ITO using a formaldehyde reduction method. The ITO support was suspended in 200 ml water in which NaHCO₃ had been dissolved in order to maintain the pH at 7. The suspension was heated under reflux at 98 °C, with stirring, for 6 h so as to ensure the complete wetting of the support. A solution of H₂IrCl₆.xH₂O dissolved in 60 ml water was stirred for 1 h and then added dropwise to the reaction mixture via a dropping funnel. The resulting mixture was refluxed for a further 2 h after which time a five times molar excess of formaldehyde, diluted in water, was added dropwise via the dropping funnel. The mixture was then refluxed for a further 15 h at 98 °C. The resulting dark blue precipitate was separated and washed five times by centrifugation at 8000 rpm, with the colourless supernatant discarded and replaced with boiling water for each repeat. The recovered precipitate was finally rinsed into a beaker and air-dried in an oven at 110 °C.

To investigate the effect of heat treatment on Ir/ITO catalysts, portions of the 40 wt. % Ir/ITO sample were heated in air for 30 min in a preheated Fisher ThermoScientific box furnace at 200, 300, 400, 500 and 600 °C. Samples treated under non-oxidising conditions were heated in a Lenton tube furnace at 300, 500 or 700 °C under flowing N₂. Prior to heating, the tube furnace was purged with N₂ for 30 min, before the sample was heated to the desired

Chapter 4: Ir/ITO electrocatalysts for the O₂ evolution reaction

temperature at a heat ramp of 5 °C min⁻¹ and then held at temperature for 30 min. The sample was then allowed to cool to room temperature under flowing N₂.

4.2.2 EDX analysis

A Phillips XL30 SEM equipped with a Thermo-Scientific UltraDry EDX system was used to examine the composition of the catalyst samples. Area scan EDX analysis was performed at an accelerating voltage of 20 kV and working distance of 10 mm.

4.2.3 XRD

XRD for was carried out using an Agilent SuperNova diffractometer with a Cu K α radiation source. XRD patterns were collected over a scan range of 10 ° to 120 ° 2 θ with a 300 s exposure time and the detector set 52 mm from the sample.

4.2.4 TEM

TEM imaging was performed using a JOEL JEM 2100 microscope with specimen samples prepared by dusting powders onto holey carbon coated Cu grids. Linear scan EDX analysis was also performed on selected samples with a FEI Technai12 TEM system.

4.2.5 BET

BET measurements were carried out with a Micromeritics Gemini 2375 Surface Area Analyser at 77 K with N₂ used as the adsorbate gas.

4.2.6 TGA

Thermogravimetric analysis was carried out with a Mettler Toledo TGA instrument that was placed in a glove-box under an O₂ atmosphere (O₂ flow rate 50 mL min⁻¹). Samples were heated in ceramic crucibles from 25 to 700 °C with a temperature increase rate of 10 °C min⁻¹.

4.2.7 Electrochemical characterisation

Electrochemical characterisation was carried out in N₂ purged 0.5 M H₂SO₄ at room temperature using an Autolab PGSTAT30 potentiostat. Thin film catalyst layers on glassy carbon electrodes prepared from catalyst inks were used as the working electrode in the RDE

cell. Pt gauze was used as the counter electrode and an MMS electrode (0.69 V vs. RHE) as the reference electrode.

4.2.7.1 Cyclic voltammetry

Cyclic voltammograms were recorded between 0.00 and 1.40 V vs. RHE at a sweep rate of 50 mV s⁻¹ with the electrode stationary.

4.2.7.2 Steady state polarisation

Steady state polarisation was carried out between 1.00 and 1.70 V vs. RHE at a sweep rate of 1 mV s⁻¹. The working electrode was rotated at 900 rpm throughout the measurements in order to remove trapped O₂ bubbles from the surface of the electrode.

4.2.7.3 Stability tests

The stability of the samples was examined by repetitive potential cycling between 0.00 and 1.45 V vs. RHE at 50 mV s⁻¹ for 1000 cycles. To measure the change in catalytic activity with potential cycling, steady state polarisation curves were recorded from 1.00 to 1.70 V vs. RHE at a sweep rate of 1 mV s⁻¹ before and after potential cycling of the experiment. During the entire measurement, the electrode was rotated at 900 rpm while N₂ gas was bubbled continuously through the electrolyte solution in order to remove O₂ from the electrode surface.

4.2.8 PEM electrolyser tests

Single cell PEM electrolyser tests were performed using the PEM electrolyser cell described in Chapter 2, section 2.4.2.2. Tests were carried out using Nafion 115 CCM's with the supported Ir electrocatalyst samples as the anode catalyst and Pt black as the cathode catalyst. The active area of each electrode was 8 cm². Tests were carried out with type 1 water supplied to the anode and cathode at 60 °C and a flow rate of 40 mL min⁻¹. The cell was pressurised to 20 bar by blowing compressed air into the back sides of both the anode and cathode. Prior to testing, the cells were held at 1 A cm⁻² for 30 min using an ISO-TECH IPS-603 DC power supply unit with the cell voltage monitored with a digital voltmeter.

4.2.8.1 Polarisation curves

Steady state polarisation curves were obtained with a Bio-Logic VMP3 potentiostat coupled to a High Current Booster, with the current stepped every 60 s from 8.00 to 0.05 A.

4.2.8.2 Stability test

The stability of the electrolyser cells was examined using an ISO-TECH IPS-603 DC power supply unit with the cell voltage monitored and recorded every 5 min with a digital voltmeter. The cells were held at constant current of 8.00 A (current density 1.00 A cm⁻²) for the duration of the test period.

4.2.9 XANES and EXAFS

XANES and EXAFS measurements were carried out on B18, Diamond Light Source, Harwell Science and Innovation Campus, UK. Spectra were collected at both the Ru K edge (22117 eV) and Ir L3 edge (11215 eV) absorption edges. Higher harmonics were rejected by using a Si(311) crystal monochromator equipped with a Pt coated mirror (Ru K edge) and a Si(111) crystal monochromator with a chromium coated mirror (Ir L3 edge).

Catalyst electrodes (surface area 1.247 cm²) were prepared as detailed in Chapter 2, section 7.2.5.1. Ex situ XANES and EXAFS measurements were carried out on dry catalyst electrodes. In situ XANES measurements were carried out on the catalyst electrodes in 0.5 M H₂SO₄ using the in situ electrochemical XAS cell as described in Chapter 2, section 7.2.5. Prior to in situ measurements, the catalyst electrodes were hydrated by boiling in water. Once the loaded cell was filled and connected to the potentiostat, three cyclic voltammograms were recorded between 0.00 and 1.40 V vs. RHE at a sweep rate of 50 mV s⁻¹, to ensure that the electrode was fully wetted and connected to the potentiostat. In situ experiments were then carried out with the following procedure:

- Potential swept from open cell voltage to 1.00 V vs. RHE at a sweep rate of 1 mV s⁻¹
- XANES spectra collected
- Potential swept from 1.00 to 1.40 V vs. RHE at a sweep rate of 1 mV s⁻¹
- XANES spectra collected
- Potential swept from 1.40 to 1.70 V vs. RHE at a sweep rate of 1 mV s⁻¹
- XANES spectra collected
- Potential swept from 1.70 to 1.80 V vs. RHE at a sweep rate of 1 mV s⁻¹
- XANES spectra collected
- Potential swept from 1.80 to 1.00 V vs. RHE at a sweep rate of 1 mV s⁻¹
- XANES spectra collected

The measurements were carried out whilst constantly pumping electrolyte solution across the surface of the electrode using a peristaltic pump. The XANES spectra were collected in fluorescence mode with 5-10 scans collected for each potential in order to improve the signal to noise ratio and to check that the sample was not changing throughout the measurement. Due to the positioning of the electrochemical cell, it was not possible to measure reference foils simultaneously with the sample data. Instead, to ensure the monochromator remained stable throughout the measurements, the reference foils were measured periodically.

4.3 Results and discussion

4.3.1 Analysis of Ir/ITO catalysts with variable Ir loading

4.3.1.1 EDX analysis

Table 1 presents EDX elemental analysis of the Ir/ITO catalysts. The experimental compositions are an average of three EDX measurements made on different parts of the sample with the error determined from the standard deviation. The data shows that the measured Ir content is very close to the nominal content, indicating that the synthesis process is successful in producing samples with the desired Ir loading. Accurate determination of the amount of Sn and In present in the samples was not possible as the L α transition energies of these elements are too similar and the peaks overlap in the EDX spectra (In = 3.286 eV, Sn = 3.443 eV). For all prepared samples, only peaks corresponding to Ir, In, Sn and O were observed.

Table 1 EDX elemental analysis of supported samples

Sample	Wt. % Ir
40 % Ir/ITO	39 \pm 2
20 % Ir/ITO	22 \pm 1
10 % Ir/ITO	10 \pm 1
5 % Ir/ITO	6 \pm 2

4.3.1.2 XRD

XRD diffractograms of the 5, 10, 20 and 40 % Ir/ITO catalysts are presented in figure 1. Patterns of the ITO support and unsupported Ir are also included. The major peak positions of the face-centred cubic Ir (ICSD 640729²⁷) and cubic ITO (ICSD 50849²⁸) crystal phases are indicated by the blue and red lines, respectively. For the supported Ir/ITO samples, only the reflections corresponding to the ITO support are identified with no discernible peaks corresponding to Ir observed. There is also no evidence of rutile IrO_2 peaks in the reflection patterns of any of the prepared samples. The XRD analysis therefore suggests that the Ir in the as prepared catalysts is amorphous.

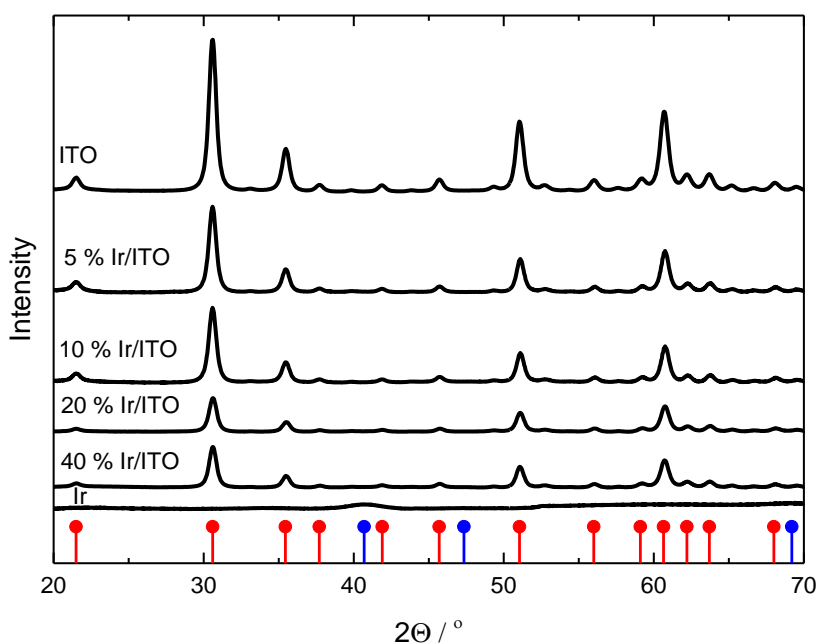


Figure 1 XRD patterns of 5, 10, 20 and 40 wt. % Ir/ITO samples compared to unsupported Ir and ITO. Peak positions of Ir reference (ICSD 640729)²⁷ are indicated by the blue lines. Major peak positions of ITO (ICSD 50849)²⁸ are indicated by the red line.

Figure 2 shows an expanded plot of the XRD patterns of the 40 % Ir/ITO and unsupported Ir sample so as to highlight the differences between the two spectra. Only a very broad Ir (111) peak at 40.7° is observed in the pattern of the unsupported Ir, indicating that this material has a highly amorphous structure. In contrast the 40 % Ir/ITO pattern has no peaks corresponding

to crystalline Ir. The small peak at 39.8° in the 40 % Ir/ITO spectra corresponds to the (024) reflection peak of ITO and not the Ir (111) peak, which occurs at 40.7° .

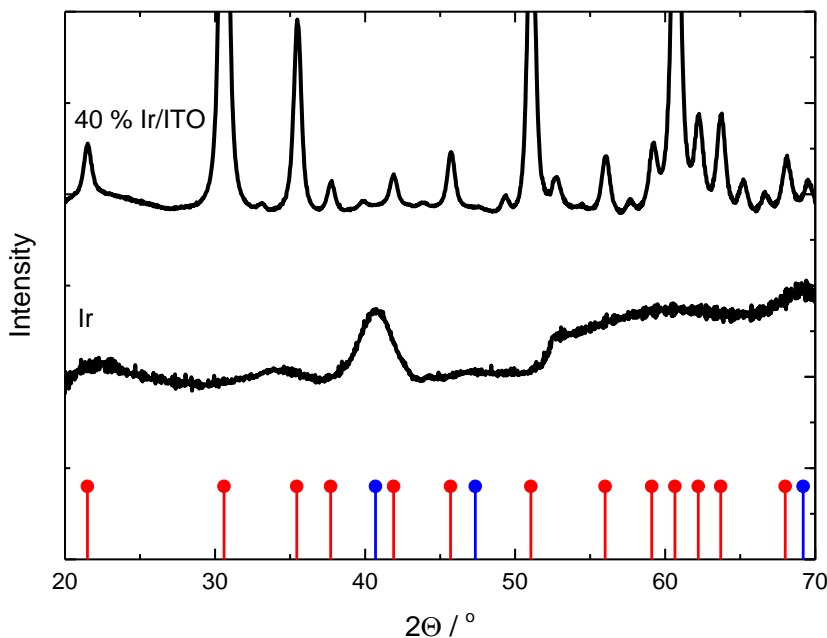


Figure 2 XRD patterns of 40 % Ir/ITO and unsupported Ir. Peak positions of Ir reference (ICSD 640729)²⁷ are indicated by the blue lines. Major peak positions of ITO (ICSD 50849)²⁸ are indicated by the dashed red line.

4.3.1.3 TEM

Figure 3 presents TEM analysis of the supported Ir/ITO samples in addition to the unsupported Ir and the ITO support. The images of the supported Ir/ITO catalysts show that they comprise distinct Ir nanoparticles dispersed over the surface of the ITO support (figures 3a-d). In contrast the unsupported Ir sample (figure 3e) is an aggregate of irregular particulates. The ITO support (figure 3f) is shown to consist of nanocrystals with particle sizes ranging between 20 – 50 nm. The average Ir particle size is observed to decrease with Ir loading. The size of the 40 % Ir/ITO catalyst is estimated to be in the range 10-20 nm, while the average size of both the 20 and 10 % Ir/ITO samples are about 5-10 nm. The size of the 5 % Ir/ITO is more difficult to discern but is estimated to be < 5 nm.

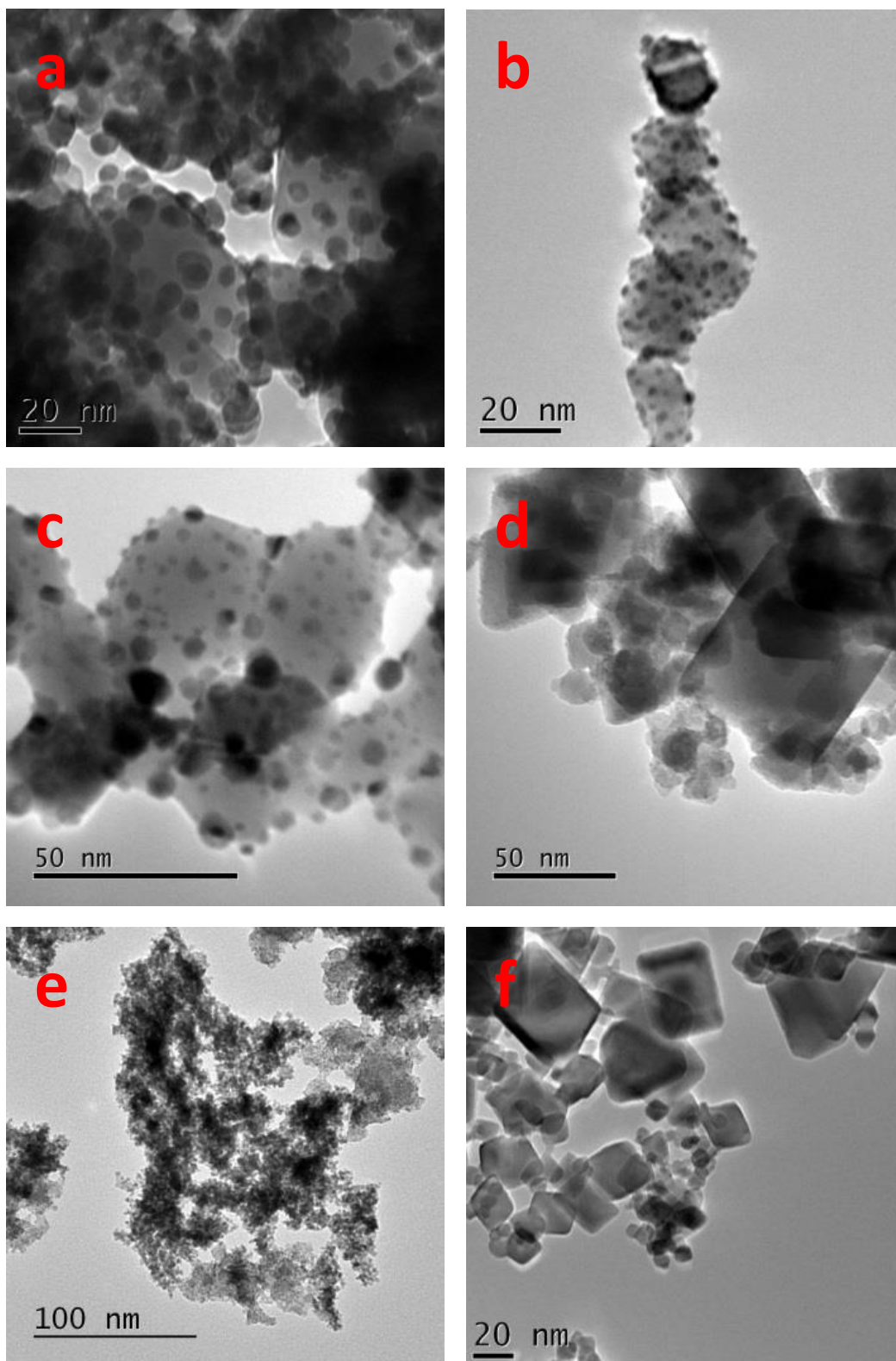


Figure 3 TEM micrographs of (a) 40, (b) 20, (c) 10 and (d) 5 wt. % Ir/ITO catalyst compared to Ir (e) and ITO (f).

EDX analysis was used to probe the relative amounts of Ir and In present in the 40 % Ir /ITO sample. Figure 4 presents linear profile EDX and the associated TEM micrograph. It can be seen from the line profile that the Ir and In are present in the same regions, which suggests that they exist in the same particles as each other as opposed there being separate regions of the two elements. Furthermore, the higher Ir signal between about 160 to 320 nm on the linear profile implies that the Ir particles decorate the surface of the ITO support and have not alloyed with it.

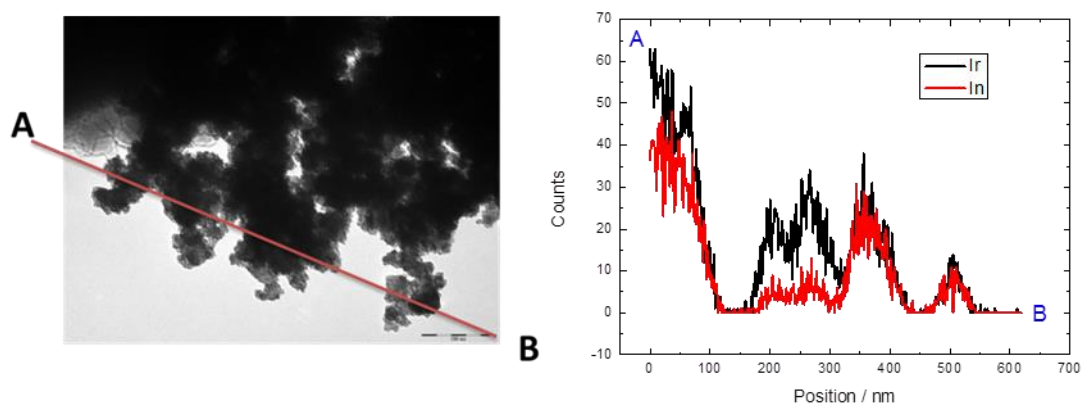


Figure 4 TEM micrograph (left) and corresponding linear EDX scan (right) showing proportion of Ir (black line) and In (red line) of 40 wt % Ir/ITO sample. The scale bar on the TEM micrograph corresponds to 100 nm

4.3.1.4 BET surface area

BET measurements were made to give an indication of the surface area of the Ir catalyst that was dispersed on the ITO support. The specific surface areas of the catalysts are shown in table 2. The surface area of the unsupported Ir sample ($48 \text{ m}^2 \text{ g}^{-1}$) is greater than the ITO support ($26 \text{ m}^2 \text{ g}^{-1}$). A similar BET surface area for ITO nanoparticles was made in the recent work by Puthiyapura et al²³. The surface area of the supported Ir/ITO catalysts is greater than the ITO support and increases with the Ir loading from $37 \text{ m}^2 \text{ g}^{-1}$ for the 5 % Ir/ITO, to $57 \text{ m}^2 \text{ g}^{-1}$ for the 40% Ir/ITO sample.

Table 2 BET surface area of supported samples

Sample	BET surface area / $m^2 g^{-1}$
Ir	48
40 % Ir/ITO	57
20 % Ir/ITO	46
10 % Ir/ITO	41
5 % Ir/ITO	37
ITO	26

4.3.1.5 Electrochemical characterisation

4.3.1.5.1 Cyclic voltammetry

Figure 5 presents the initial cyclic voltammetry curves of the catalyst samples in 0.5 M H_2SO_4 at a sweep rate of 50 mV s^{-1} in the potential window 0-1.4 V vs. RHE. The voltammetry is normalised to the geometric surface area of the glassy carbon electrode (figure 5a) and to the mass of Ir deposited on the electrode (figure 5b).

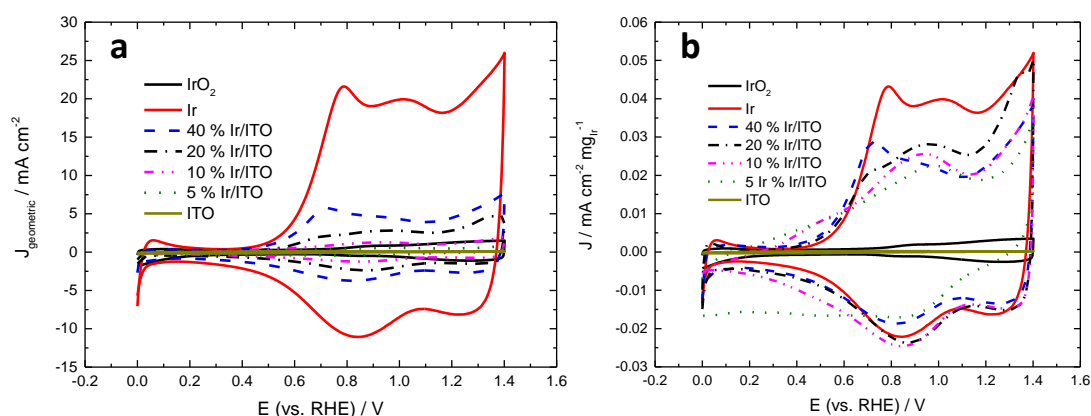


Figure 5 Initial cyclic voltammetry in 0.5 M H_2SO_4 at 50 mV s^{-1} of unsupported Ir (red line), 40 % Ir/ITO (dashed blue line), 20 % Ir/ITO (dot-dashed black line), 10 % Ir/ITO (dot-dot-dashed pink line), 5 % Ir/ITO (dot green line), ITO (gold line) and IrO_2 (black line). The voltammetry is presented normalised to the geometric surface area (a) and to the mass of Ir on the glassy carbon electrode (b).

Chapter 4: Ir/ITO electrocatalysts for the O₂ evolution reaction

The cyclic voltammetry of the Ir and the Ir/ITO catalysts in figure 5 is very different to the voltammetry of the IrO₂. The voltammetry of the Ir and Ir/ITO is characteristic of the voltammetry reported for anodic iridium oxide films (AIROF)²⁹⁻³¹. An AIROF is an Ir oxide film that has been grown electrochemically on metallic Ir, by either potential cycling or potential pulsing in the range 0.00 to 1.45 V vs. RHE. It has been suggested that the structure of AIROF's consists of an extremely thin anhydrous inner oxide layer, and an extensively hydrated outer oxide layer that contains both bound and trapped water molecules³². The observation of AIROF voltammetry without the pre-requirement of potential cycling, suggests that the as prepared Ir/ITO catalysts possess a very hydrous innate structure or that such a structure is formed on the immersion of the catalyst in the H₂SO₄ electrolyte. This hypothesis is in agreement with the XRD which showed no crystalline Ir peaks.

The sets of peaks in the potential region from 0.4 to 1.4 V are related to solid state redox transitions of the Ir centres that are accompanied by ion exchange with the electrolyte, following the general reaction scheme (equation 1)^{29,33}



The anodic peak at about 1.0 V and cathodic peak at 0.9 V are attributed to the Ir(III)/(IV) transition³⁴, while the set of peaks at about 1.35 V are believed to be due to the Ir(IV)/(V or VI) redox couple/s that occur prior to the onset of O₂ evolution at potentials above 1.40 V^{29,31}. The slight peak potential separation of the Ir(III)/(IV) peaks is thought to be due to the complex reaction kinetics of the proton exchange reaction, that may be limited either by mass transport of the protons through the hydrous oxide film, or by the electron transfer³⁵. The anodic peak at about 0.7 V is often observed in the voltammetry of hydrous iridium oxide films and is attributed to the presence of anions within the Ir structure^{36,37}, and/or to the oxidation of Ir sites located near the Ir metal/inner oxide interface³⁸. This peak was not observed in subsequent scans of any of the samples suggesting that in either case, the process is irreversible. The cathodic peak observed at 0.0 V is attributed to the onset of hydrogen evolution. In contrast to the voltammetry of the Ir/ITO catalysts, the voltammetry of the ITO support is featureless indicating that the electrochemical response of the supported catalysts is entirely dominated by the Ir.

The charge under the region from about 0.4 to 1.4 V vs. RHE of a cyclic voltammogram of a hydrous Ir oxide film gives an indication of the amount of hydrous oxide present³⁴. It is therefore assumed that the voltammetric charge is related to the electroactive surface area of the catalysts. Comparison of the voltammetry in figure 5a shows that the surface area of the Ir

Chapter 4: Ir/ITO electrocatalysts for the O_2 evolution reaction

and Ir/ITO samples is greater than that of the IrO_2 , despite the BET analysis indicating that the specific surface area of the IrO_2 ($168 \text{ m}^2 \text{ g}^{-1}$) is significantly higher than the supported Ir/ITO catalysts (40 % Ir/ITO = $57 \text{ m}^2 \text{ g}^{-1}$). This is likely to be a consequence of the highly hydrated nature of the amorphous Ir oxide particles which contribute a large proportion for the electrochemical surface area but not to the specific surface area. The voltammetric charge of the Ir/ITO catalysts decreases with Ir loading, which may be correlated to the decrease in the amount of Ir dispersed on the ITO, as shown by the BET measurements and TEM analysis.

4.3.1.5.2 Steady state polarisation

The electrocatalytic activity of the Ir/ITO samples was assessed in 0.5 M H_2SO_4 by steady state polarisation at a sweep rate of 1 mV s^{-1} , as shown in figure 6. The supported catalysts are compared to the unsupported Ir, the ITO support and the unsupported IrO_2 catalyst prepared in-house by the Adams fusion method. The unsupported IrO_2 is included to represent the performance of a current state-of-the-art O_2 evolution electrocatalyst.

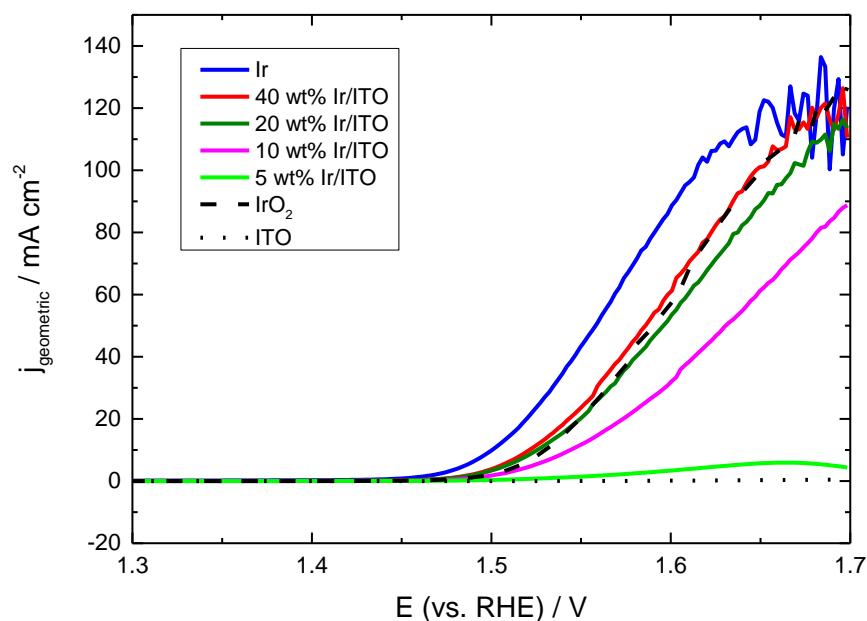


Figure 6 Steady state polarisation of Ir (blue line), 40 % Ir/ITO (red line), 20 % Ir/ITO (dark green line), 10 % Ir/ITO (pink line) and 5 % Ir/ITO (light green line) compared to IrO_2 (dashed black) and ITO (dotted black) in 0.5 M H_2SO_4 at 1 mV s^{-1} with the electrode rotated at 900 rpm. The catalyst loading was 0.50 mg cm^{-2} .

Chapter 4: Ir/ITO electrocatalysts for the O₂ evolution reaction

The steady state polarisation in figure 6 shows that the activity of the supported Ir/ITO catalysts increases with the Ir loading, correlating with the increase of the active component and the increase in the electrochemical surface area as suggested by the cyclic voltammtery. It is also apparent that the activity of the 40 % Ir/ITO and 20 % Ir/ITO are comparable to the unsupported IrO₂, while the activity decreases significantly as the loading is reduced from 10 to 5 wt. %. The ITO support is inactive towards the O₂ evolution reaction. The potential at a current density of 1 mA cm⁻² has been used in previous supported O₂ evolution catalyst literature to evaluate the catalyst performance^{10,15}. The potentials in table 3 show that the potential decreases from 1.48 to 1.53 V with the decrease in Ir content from 40 to 5 wt. %. Very similar values were obtained with IrO₂/Nb_{0.05}Ti_{0.95}O₂ samples with Ir loadings from 33 – 17 wt. %¹⁰, and with 20 % Ir/ATO¹⁵.

Table 3 Potential at the current density of 1 mA cm⁻² obtained from steady state polarisation. The error is determined from three independent measurements at a 95 % confidence limit

Sample	Potential at 1 mA cm ⁻² / V
Ir	1.45 ± 0.01
40 % Ir/ITO	1.48 ± 0.01
20 % Ir/ITO	1.48 ± 0.01
10 % Ir/ITO	1.49 ± 0.01
5 % Ir/ITO	1.53 ± 0.01
ITO	n/a
IrO ₂	1.49 ± 0.01

The best performing catalyst as observed from the steady state polarisation in figure 7, is the unsupported Ir sample which has a voltage of 1.45 V at a current density of 1 mA cm⁻². The high activity of the Ir compared to the IrO₂ is likely due to the highly hydrated nature of the Ir, as indicated by the XRD and cyclic voltammtery experiments. Several studies comparing the O₂

Chapter 4: Ir/ITO electrocatalysts for the O_2 evolution reaction

evolution reaction on thermally prepared IrO_2 and on AIROFs have shown that the same Tafel slope is observed for both materials, suggesting that the same O_2 mechanism must occur on both oxide forms^{31,39,40}. This implies that the increased activity for the O_2 evolution reaction is related to the increased surface area of the water permeable AIROF than as for crystalline IrO_2 ^{32,41}. It is further hypothesised that the impressive performance of the supported Ir catalysts compared to the IrO_2 is also due to the hydrous nature of the Ir particles on the ITO.

The steady state polarisation presented in figure 6 was normalised by the mass of Ir on the glassy carbon electrode to produce figure 7. The mass normalised current density gives an indication of the cost-effectiveness of the supported catalysts. Comparison of the mass activity of the catalysts made at 1.60 V vs. RHE is presented in figure 8.

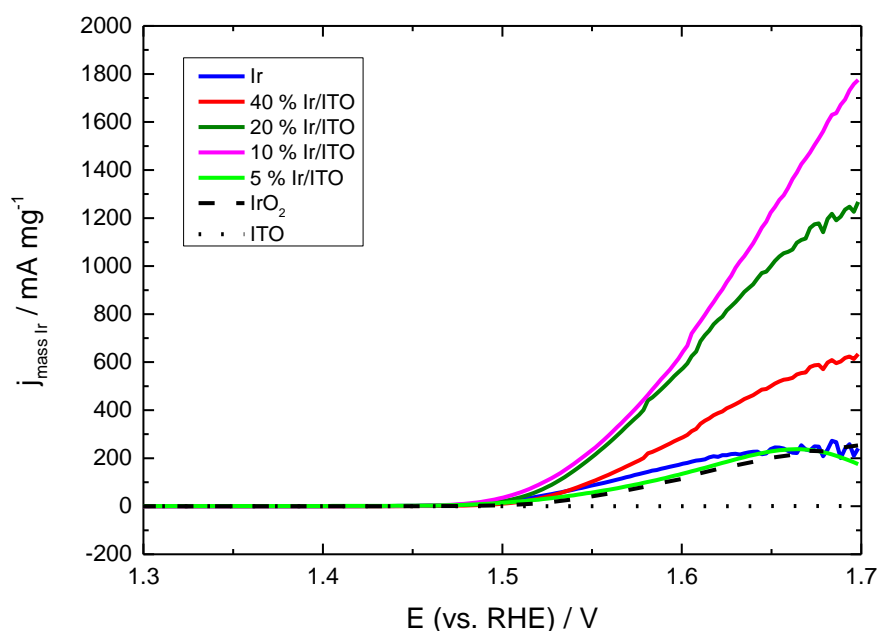


Figure 7 Steady state polarisation of Ir (blue line), 40 % Ir/ITO (red line), 20 % Ir/ITO (dark green line), 10 % Ir/ITO (pink line) and 5 % Ir/ITO (light green line) compared to IrO_2 (dashed black) and the ITO (dotted black line) in 0.5 M H_2SO_4 at 1 mV s^{-1} with the electrode rotated at 900 rpm. The catalyst loading was 0.50 mg cm^{-2} . The voltammetry is normalised to the mass of Ir on the glassy carbon electrode.

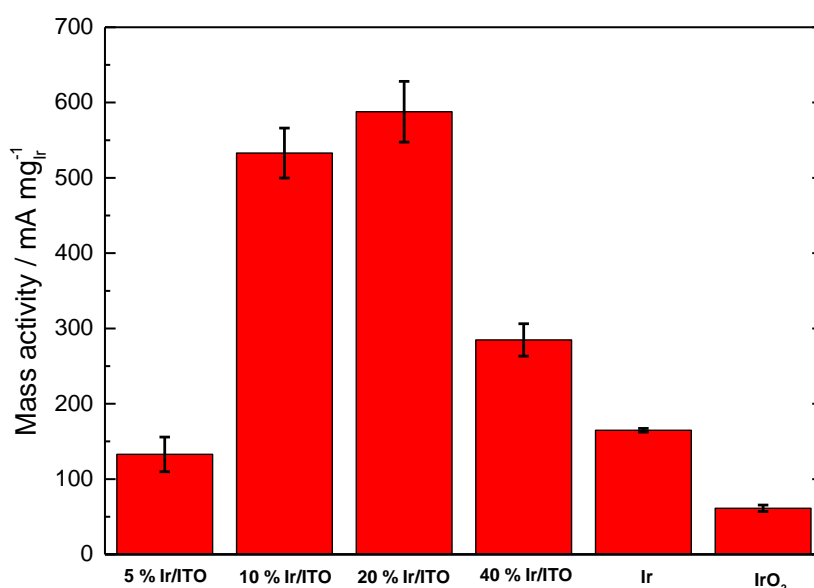


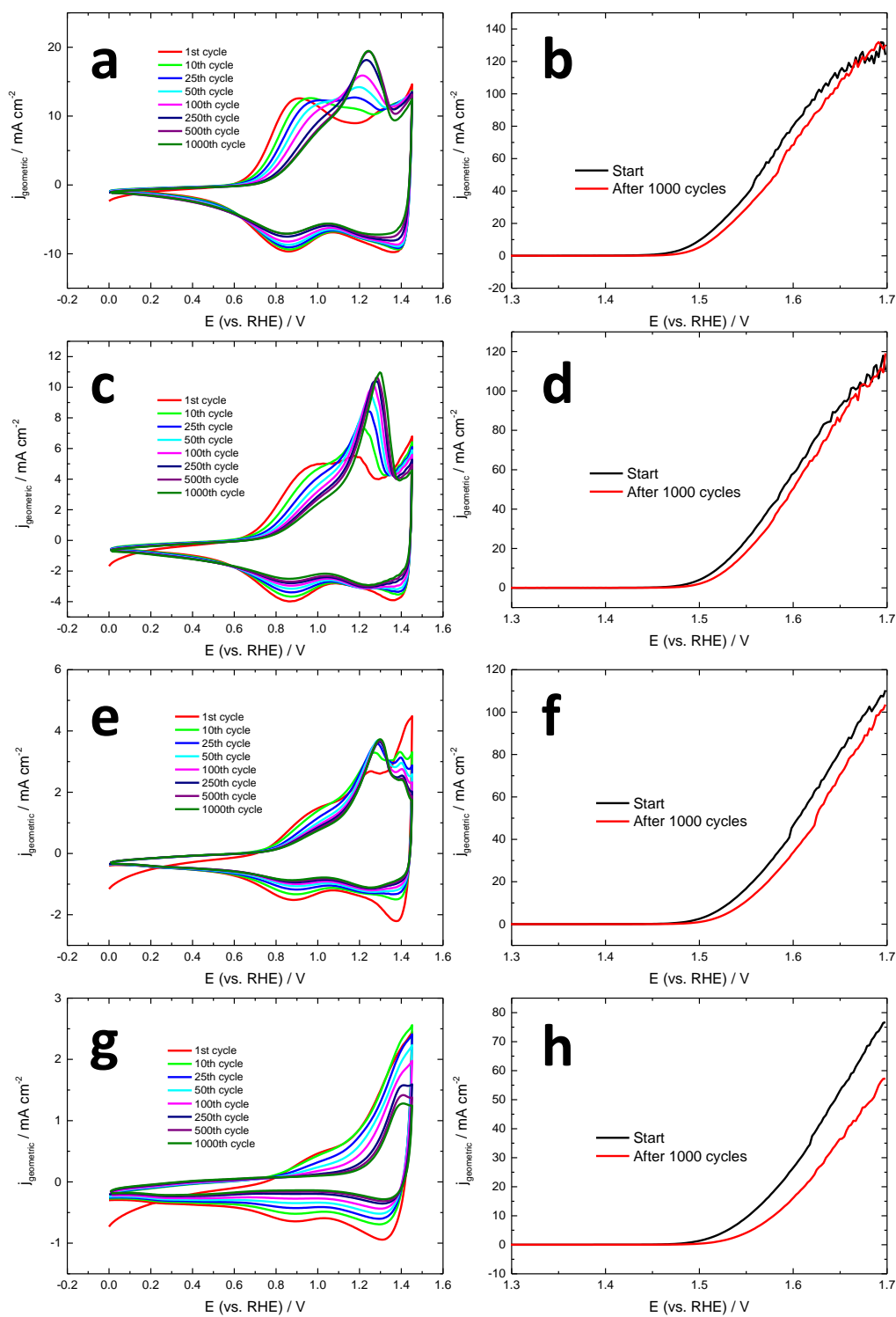
Figure 8 Mass activity at 1.60 V of supported Ir/ITO catalysts with variable Ir loadings compared to unsupported Ir and IrO₂. The error is determined from three independent repeat measurements at a 95 % confidence limit.

The mass normalised steady state polarisation in figure 7 shows that the mass activity of the 40, 20 and 10 % Ir/ITO catalysts is superior to the unsupported Ir and the IrO₂. Furthermore, with the exception of the 5 wt. % sample, the mass activity increases as the Ir loading is decreased. This suggests that the support facilitates the dispersal of the active phase and enhances the catalytic efficiency of the Ir. Comparison of the mass activities at 1.60 V in figure 8 shows that the optimal loading of 20 wt. % Ir ($588 \pm 25 \text{ mA mg}_{\text{Ir}}^{-1}$) is about 3.6 times that of the unsupported Ir ($165 \pm 9 \text{ mA mg}_{\text{Ir}}^{-1}$) and 9.6 times than that of IrO₂ ($61 \pm 3 \text{ mA mg}_{\text{Ir}}^{-1}$).

4.3.1.5.3 Stability test

The stability of the catalysts in 0.5 M H₂SO₄ was evaluated by repetitive potential cycling between 0.00 and 1.45 V vs. RHE at a sweep rate of 50 mV s⁻¹. Changes in electrocatalytic activity were assessed by recording steady state polarisation curves before and after the potential cycling procedure. Figure 9 presents the cyclic voltammetry and steady state polarisation of the stability test. Changes in the electrochemical surface area with potential cycling were estimated by measuring the voltammetric charge density of the cyclic voltammograms. Plots of the change in charge density and % loss of charge density with potential cycling are shown in figure 10.

Chapter 4: Ir/ITO electrocatalysts for the O_2 evolution reaction



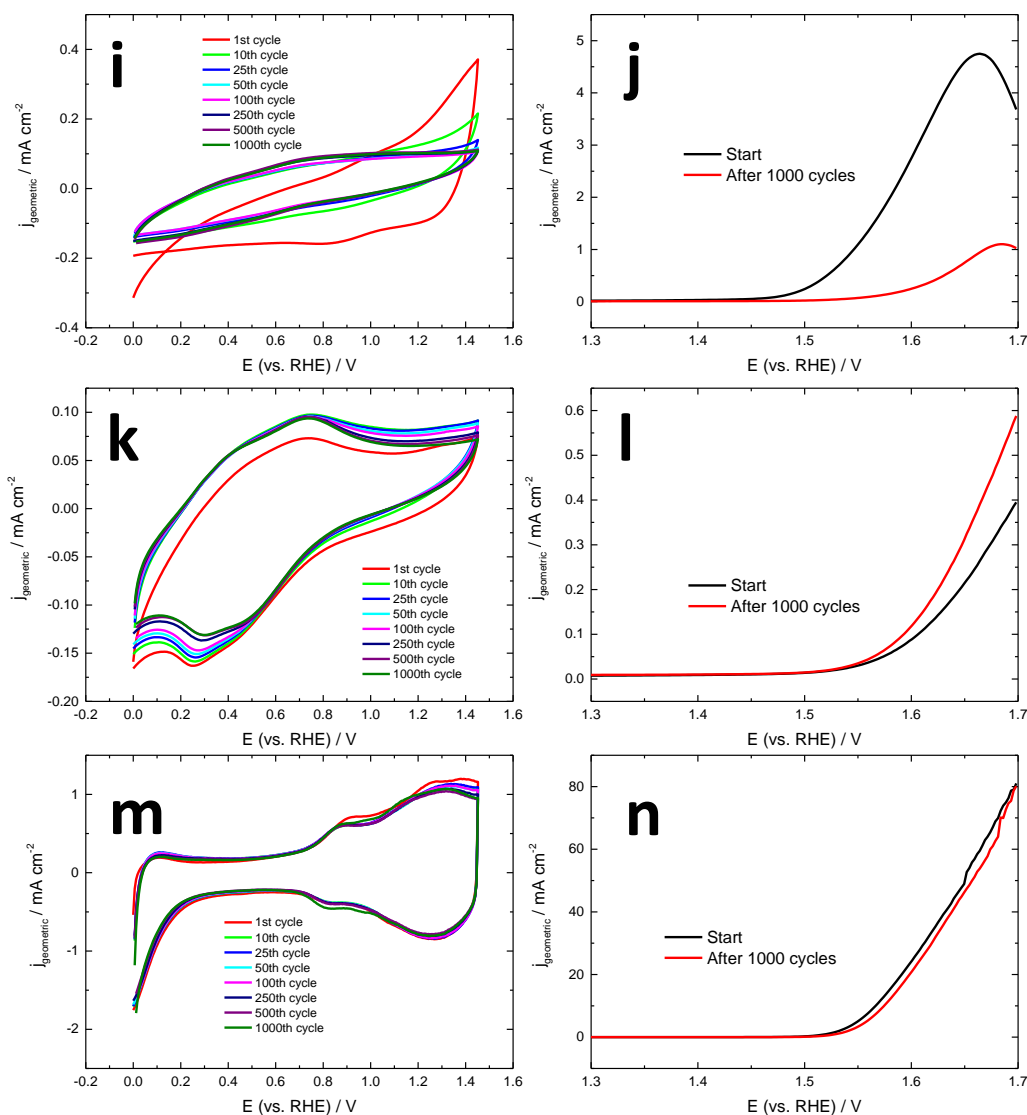


Figure 9 Repetitive cyclic voltammetry at 50 mV s^{-1} (left) and steady state polarisation at 1 mV s^{-1} recorded before and after the 1000 potential cycles. Samples are Ir (a and b), 40 % Ir/ITO (c and d), 20 % Ir/ITO (e and f), 10 % Ir/ITO (g and h), 5 % Ir/ITO (i and j), ITO (k and l) and IrO_2 (m and n).

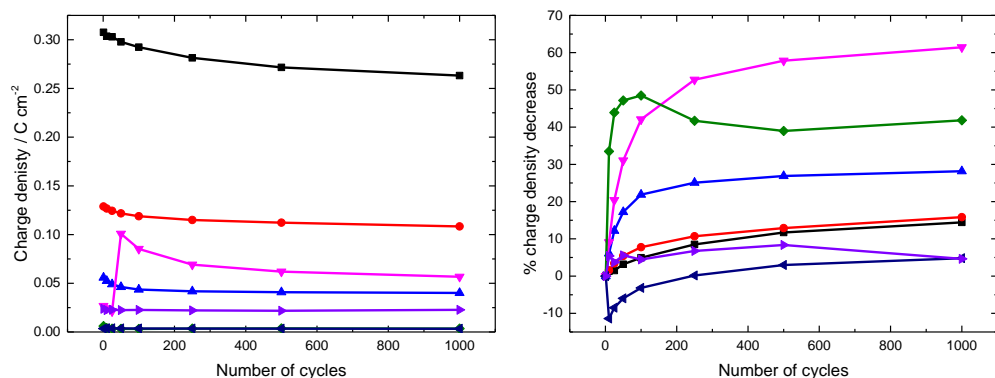


Figure 10 Change in the charge density (left) and the % loss of charge density (right) with potential cycling between 0.00 and 1.45 V vs. RHE in 0.5 M H_2SO_4 . Charge densities determined from the voltammetric charge of the cyclic voltammetry are shown for Ir (black line), 40 % Ir/ITO (red line), 20 % Ir/ITO (blue line), 10 % Ir/ITO (pink line), 5 % Ir/ITO (green line), ITO support (dark blue line) and IrO_2 (purple line).

The cyclic voltammograms in figure 10 show that the profiles of the curves change with repetitive potential cycling between 0.00 – 1.45 V. The curves of the Ir, 40 % Ir/ITO, 20 % Ir/ITO all show the same general change in shape with potential cycling. The peaks of the Ir(III)/Ir(IV) couple decrease with potential cycling and the peaks of the Ir(IV)/Ir(V or VI) couple increase. This suggests that the surface of the catalysts becomes enriched with Ir centres of higher valence state due to oxidation of the Ir species during the potential cycles. Measurement of the % charge density decrease with cycling suggests that the unsupported Ir and the 40 % Ir/ITO catalysts lose 10 % of the electrochemical surface area, whilst the 20 % Ir/ITO sample decreases by 25 %. However the steady state polarisation of these catalysts show that the change in in the surface area has a limited effect on the O_2 evolution activity, as the polarisation curves are only shifted to slightly higher potentials after the potential cycling, as indicated by the potential increases measured at 1 mA cm^{-2} shown in table 4.

In the case of the 10 % Ir/ITO sample, the potential cycling causes the peaks in the voltammetry to decrease, with a 60 % decrease in the charge density observed. This implies a large reduction in the electrochemical active area of the catalyst. The activity of the catalysts is also somewhat diminished, with a potential increase at 1 mA cm^{-2} of 30 mV.

In contrast, the 5 % Ir/ITO shows poor stability with potential cycling. Figure 10i shows that the shape of the cyclic voltammetry becomes featureless within the first 25 potential cycles and does not change significantly thereafter. The effect of the potential cycling on the steady state

polarisation is also considerable, with a potential increase of 120 mV observed at 1 mA cm⁻². It is suggested that the poor stability of the 5 % Ir/ITO catalysts is related to the small size of the Ir deposits as indicated by TEM imaging. Smaller particles are less thermodynamically stable than larger particles to processes such as dissolution⁴².

In comparison to the other samples, the voltammetry of the IrO₂ catalyst remains largely unchanged with potential cycling. The % change density decrease associated with this sample suggests that the electrochemical surface area of the IrO₂ decreases by 7 % after 500 cycles but then increases again after 1000 cycles. This is attributed to surface roughening of the catalyst surface. The activity of this catalyst remains unaffected with the cycling with a potential increase of 10 mV at 1 mA cm⁻².

Table 4 Potential increase at 1 mA cm⁻² of the steady state polarisation measured before and after potential cycling

Sample	Potential increase at 1 mA cm ⁻² / mV
Ir	10
40 % Ir/ITO	10
20 % Ir/ITO	20
10 % Ir/ITO	30
5 % Ir/ITO	120
IrO ₂	10

4.3.1.6 PEM water electrolyser cell tests

The performance of the 40 and 20 wt. % Ir/ITO catalysts compared to the IrO₂ was assessed in single cell PEM water electrolyzers at 60 °C and 20 bar. Figure 11 shows polarisation curves of the cells with the supported catalysts as the anodic catalysts and a Pt black cathode catalyst. The curves are not iR drop corrected. The performances of the supported samples are superior to that of the unsupported IrO₂ catalyst. Cell voltages at 1000 mA cm⁻² were 1.83, 1.84 and 1.85 V for the 40 % Ir/ITO, 20 % Ir/ITO and IrO₂ catalysts, respectively. The results indicate that the prepared Ir/ITO catalysts offer a better performance in a PEM electrolyser cell than IrO₂,

Chapter 4: Ir/ITO electrocatalysts for the O_2 evolution reaction

with the precious metal loading at the anode reduced by a factor of 1.35 (40 % Ir/ITO) and 1.95 (20 % Ir/ITO) mg cm^{-2} .

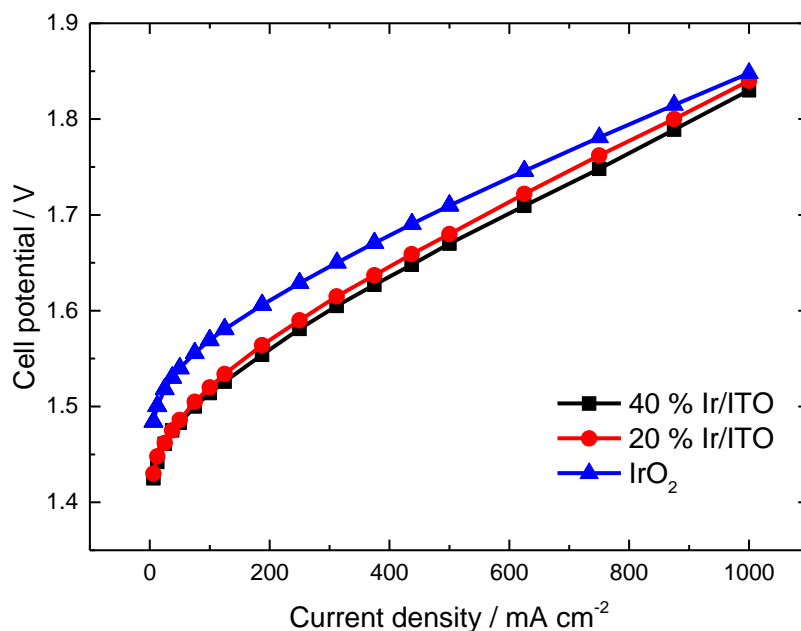


Figure 11 Polarisation curves of single cell PEM electrolyzers at 60 °C and 20 bar with 40 % Ir/ITO (black), 20 % Ir/ITO (red) and IrO_2 (blue) as the anode catalysts. The cathode catalyst was Pt black. The catalyst loading at the anode and cathode was 3 mg cm^{-2} .

The stability of the single cell PEM electrolyzers was assessed by monitoring the change in cell voltage at a constant current density of 1 A cm^{-2} for a period of 600 h. The cell potential vs. time curves of the cells with the supported Ir/ITO samples as the anodic catalysts are presented in figure 12. The decrease in the cell potential over the first 50 – 100 h observed for all cells is due to the various cell components such as the membrane and catalyst layers, becoming more hydrated and conductive.

Figure 12 shows that the cell voltage with 40 % Ir/ITO stabilises at about 1.76 V after 100 h, and remains stable with a small rise to 1.77 V observed after 600h. The cell with 20 % Ir/ITO however, is not stable as the voltage increases from 1.78 V at 100 h to 1.88 V at 600h. In comparison the cell with IrO_2 as the anodic catalyst remains at a constant voltage of 1.82 V. The rate of voltage increase for the 40 % Ir/ITO cell ($32 \mu\text{V h}^{-1}$) compares favourably to the best stability data reported in the literature for PEM electrolyzers^{11,43-46}, highlighting the significant durability of the 40 % Ir/ITO catalyst.

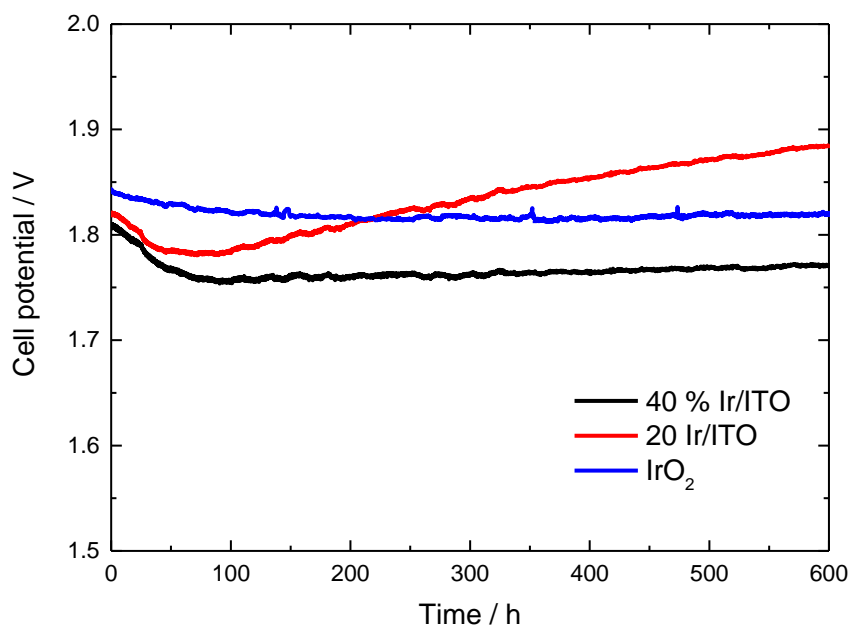


Figure 12 Stability test of single cell PEM electrolyzers at 60 °C and 20 bar with 40 % Ir/ITO (black), 20 % Ir/ITO (red) and IrO₂ (red) as the anode catalysts. The cathode catalyst was Pt black as the cathode catalyst. The catalyst loading at the anode and cathode was 3 mg cm⁻².

4.3.2 Heat treatment of 40 % Ir/ITO

4.3.2.1 XRD

XRD patterns of the 40 % Ir/ITO catalyst heated in air at 200, 300, 400, 500 and 600 °C are presented in figure 13. The major peak positions of the tetragonal IrO_2 (ICSD 84577⁴⁷) and cubic ITO (ICSD 50849²⁸) crystal phases are indicated by the blue and red lines, respectively. No peaks corresponding to any other phases were observed. For the Ir/ITO samples heated at temperatures from 200 to 400 °C, only the reflections corresponding to the ITO support are identified with no discernible peaks corresponding to IrO_2 observed. However the samples heated at 500 and 600 °C show reflection peaks matching an IrO_2 phase. The XRD analysis implies that 40 % Ir/ITO catalysts heated at temperatures below 400 °C remain amorphous, whereas for catalysts heated at temperatures at and above 500 °C, the Ir is oxidised to IrO_2 .

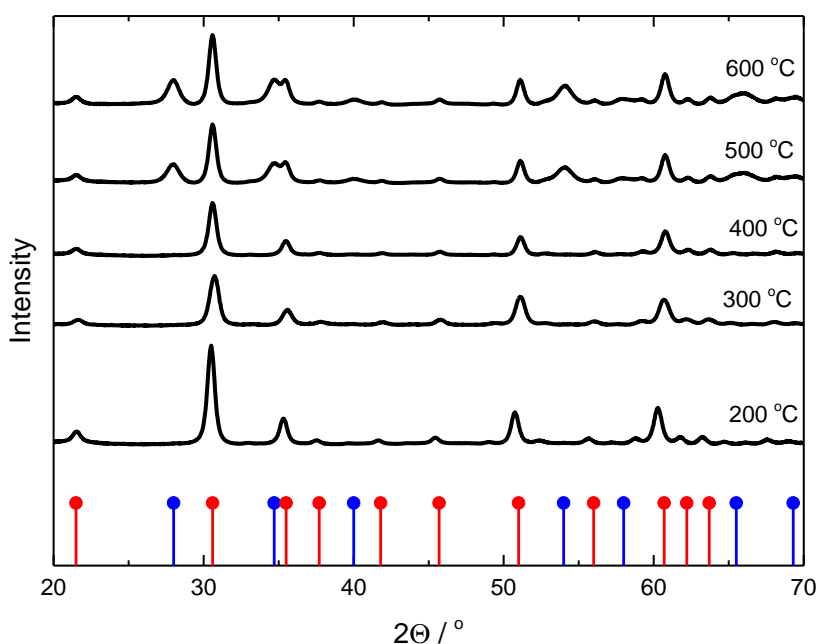


Figure 13 XRD patterns of 40 wt. % Ir/ITO heated in air for 30 min at various temperatures, compared with the major reflection peaks of ITO (red line) (ICSD 50849)²⁸ and IrO_2 (blue line) (dashed orange line) (ICSD 84577)⁴⁷ references

XRD patterns of the 40 % Ir/ITO catalyst heated in N_2 at 300, 500 and 700 °C are presented in figure 14. The major peak positions of the face centred cubic Ir (tetragonal IrO_2 (ICSD 84577⁴⁷) and cubic ITO (ICSD 50849²⁸) crystal phases are indicated by the blue and red lines, respectively. No peaks corresponding to any other phase were observed. The sample heated at

300 °C only has reflection peaks for ITO suggesting that the Ir is amorphous. However for the samples heated at 500 and 700 °C, peaks corresponding to both cubic Ir and tetragonal IrO_2 are observed. The observation of Ir peaks suggests that the amorphous Ir crystallises at temperatures above 300 °C, while the observation of IrO_2 peaks suggests that the tube furnace was not sufficiently purged with N_2 before heating or that O_2 leaked into the furnace during heating. Alternatively the oxidation may have arisen from latent oxygen species trapped within the Ir particles.

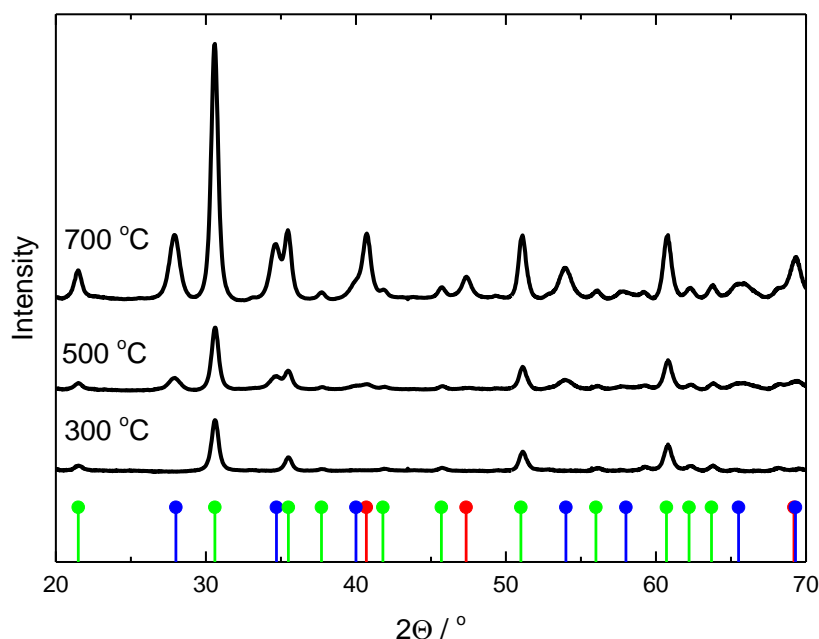


Figure 14 XRD patterns of 40 wt. % Ir/ITO heated at 300, 500 and 700 °C for 30 min under flowing N_2 , compared with the major reflection peaks of Ir (red line) (ICSD 640729)²⁷, ITO (green line)²⁸ (ICSD 50849) and IrO_2 (blue line) (ICSD 84577)⁴⁷

4.3.2.2 TGA

The thermal stability of the 40 % Ir/ITO catalyst in an O_2 atmosphere was investigated by TGA analysis. The TGA profile of the 40 % Ir/ITO sample is compared to the ITO support in figure 15. The TGA profile of the 40 % Ir/ITO catalyst shows a mass decrease of about 3 % that starts at 50 °C and continues to 400 °C. This is most likely due to the loss of water from the hydrated Ir particles, as the TGA profile of the ITO shows only a very moderate mass decrease within the same temperature range. A mass increase of about 6.5 % is then observed for the 40 % Ir/ITO catalyst, starting at 500 °C and continuing to 700 °C. This is attributed to the oxidation of the Ir particles because the XRD patterns of the 40 % Ir/ITO samples heated in air at temperatures at

Chapter 4: Ir/ITO electrocatalysts for the O_2 evolution reaction

and above 500 °C, showed peaks corresponding to crystalline IrO_2 . In contrast the ITO shows a small mass increase at about 650 °C, which is ascribed to the oxidation of the support material. Previous TGA analysis of ITO has shown it to be thermally stable up to 1000 °C^{22,23}.

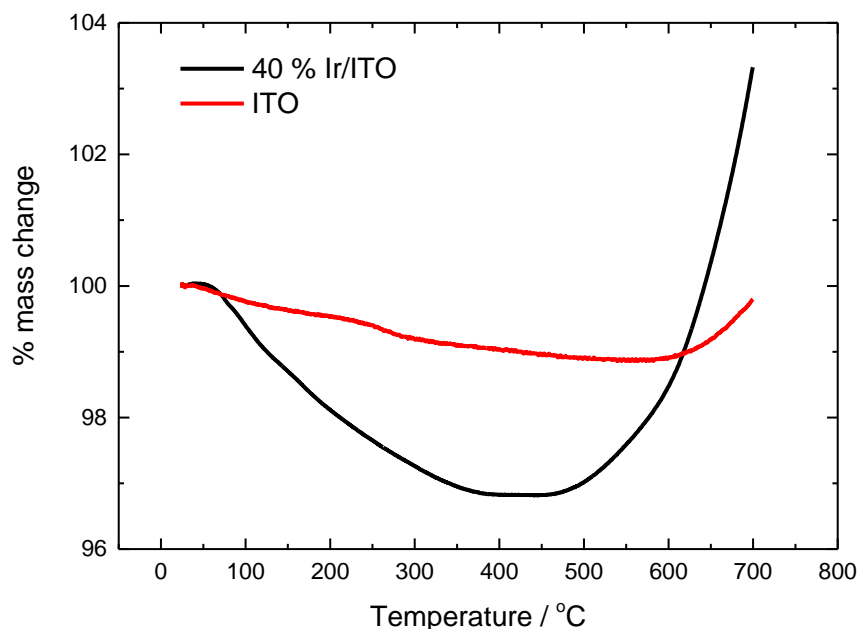


Figure 15 TGA profile of 40 % Ir/ITO and ITO heated from 20 to 700 °C under an O_2 atmosphere at a temperature increase rate of 10 °C min^{-1} .

4.3.2.3 TEM

TEM micrographs of the 40 % Ir/ITO samples heated at 300, 400 and 500 °C under N_2 in addition to the 40 % Ir/ITO heated at 500 °C in air, are shown in figure 16. The scale bar in all images corresponds to 50 nm. The TEM images of the samples heated under N_2 at 300 and 500 °C show that although there remains a good dispersion of Ir on the ITO, some Ir agglomeration has occurred with some larger particles of about 25-30 nm diameter observed. The image of the sample heated at 700 °C shows that a greater degree of agglomeration occurs at higher temperatures.

In comparison, the TEM image of the sample heated in air at 500 °C shows that the dispersion of Ir on the ITO support is reduced compared to the sample heated at the same temperature in N_2 . The shape of the Ir particles is also marginally different, with a more cubic-like structure observed in contrast to the more spherical Ir particles observed for the sample heated at 500 °C in N_2 .

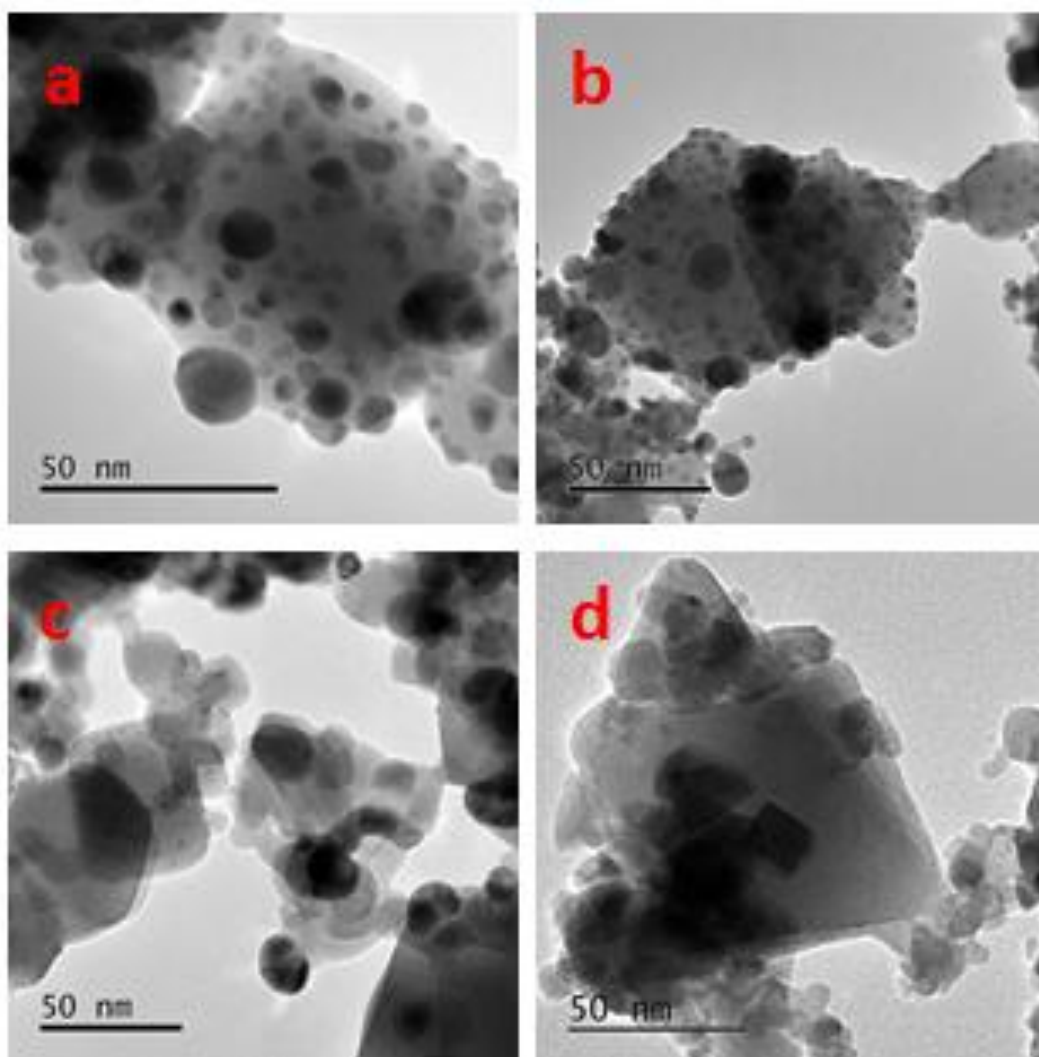


Figure 16 TEM micrographs of 40 % Ir/ITO heated under N₂ at (a) 300, (b) 500 and (c) 700 °C, and (d) under air at 500 °C. The scale bar corresponds to 50 nm.

4.3.2.4 EXAFS

Ex situ EXAFS spectra of the IrO₂, 40 % Ir/ITO, 40 % Ir/ITO (500 °C, air) and 40 % Ir/ITO (500 °C, N₂) catalysts were recorded at the Ir L₃ edge. The Fourier transforms of the EXAFS spectra for these samples are compared in figure 17. The Fourier transform of the unheated 40 % Ir/ITO has only one well-defined peak in the range 1 to 2 Å, which primarily corresponds to scattering from the first shell of octahedrally-coordinated O atoms. The absence of further shells indicates that the Ir is highly amorphous which correlates with the XRD analysis of this sample. In contrast, the Fourier transform of the IrO₂ catalyst shows a series of peaks out to distance of 7 Å, corresponding to photoelectron backscatter from outer Ir shells and reflecting the highly ordered, crystalline structure of the rutile oxide. The Fourier transforms of both heat treated samples show a very similar profile to the IrO₂ catalyst, indicating that both heat

Chapter 4: Ir/ITO electrocatalysts for the O_2 evolution reaction

treatment procedures produce highly ordered catalyst structures. The peak intensities of the sample heated in air are higher than the sample heated in N_2 which suggests that the former sample has the greater degree of crystallinity.

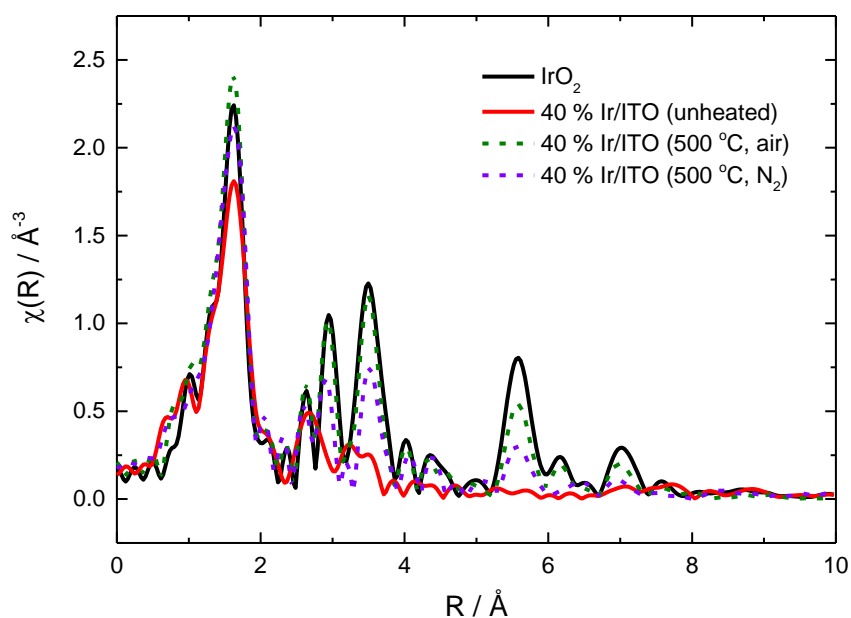


Figure 17 k^2 -weighted Fourier transforms of the EXAFS spectra at the L_3 edge for IrO_2 (black line), 40 % Ir/ITO (unheated) (red line), 40 % Ir/ITO (500 °C, O_2) (dashed green line) and 40 % Ir/ITO (500 °C, N_2) (dashed purple line)

4.3.2.5 Electrochemical characterisation

4.3.2.5.1 Cyclic voltammetry

Figure 18 presents cyclic voltammetry of the catalyst samples heated in air, in 0.5 M H_2SO_4 at a sweep rate of 50 mV s^{-1} . Figure 19 presents the voltammetry of the samples heated in N_2 . The voltammetry is normalised to the geometric surface area of the glassy carbon electrode.

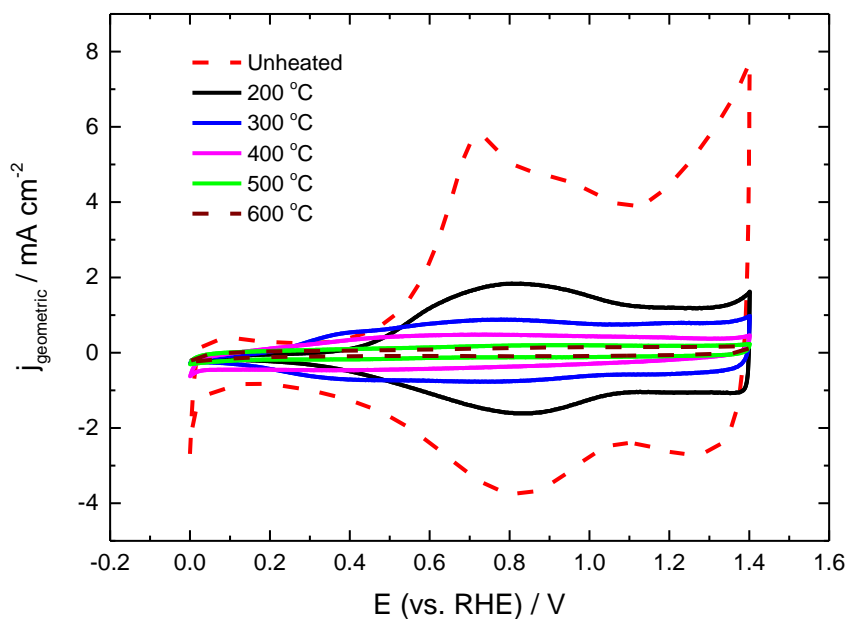


Figure 18 Cyclic voltammometry of the 40 % Ir/ITO catalyst unheated (dashed red line) and heated in air at 200 (black line), 300 (blue line), 400 (pink line), 500 (green line) and 600 (dashed purple line) in 0.5 M H_2SO_4 at a scan rate of 50 mV s^{-1}

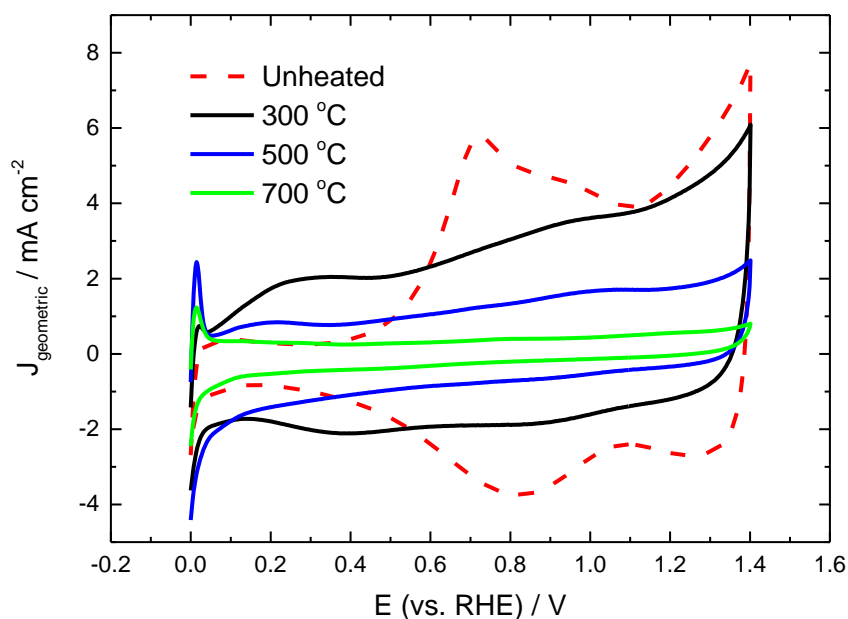


Figure 19 Cyclic voltammometry of the 40 % Ir/ITO catalyst unheated (dashed red line) and heated in N_2 at 300 (black line), 500 (blue line), and 700 (green line) in 0.5 M H_2SO_4 at a scan rate of 50 mV s^{-1}

The voltammometry in figure 18 shows that a large change in the shape of the voltammograms occurs as the 40 % Ir/ITO is heated in air. The voltammetric current decreases with the increasing temperature, with the voltammometry of the samples heated at 500 and 600 °C becoming very featureless. This change is attributed to the loss of electrochemical surface area caused by vaporisation of the water of the hydrated oxide, in addition to the crystallisation of the oxide to the rutile structure. The heat treatment of AIROFs has previously been shown to modify the voltammetric response to something resembling the characteristic voltammometry of rutile IrO_2 ⁴⁸. The voltammometry of the 40 % Ir/ITO heated in N_2 (figure 19) shows a similar trend however the decrease in the voltammetric current is not as considerable as the samples heated in air.

4.3.2.5.2 Steady state polarisation

The activity of the 40 % Ir/ITO samples heated in air and in N_2 was assessed by steady state polarisation in 0.5 M H_2SO_4 . The voltammometry of the samples heated in air compared to the unheated 40 % Ir/ITO and the IrO_2 catalysts is presented in figure 20. The activity of the catalysts decreases with the increase in heating temperature, with a large decrease observed

between the samples heated at 400 and 500 °C. The general decrease in activity with temperature is probably due to Ir particle agglomeration. However as the large decrease corresponds to the samples that displayed IrO_2 peaks in the XRD patterns, it implies that the loss of activity is caused by the oxidation of the Ir particles to IrO_2 .

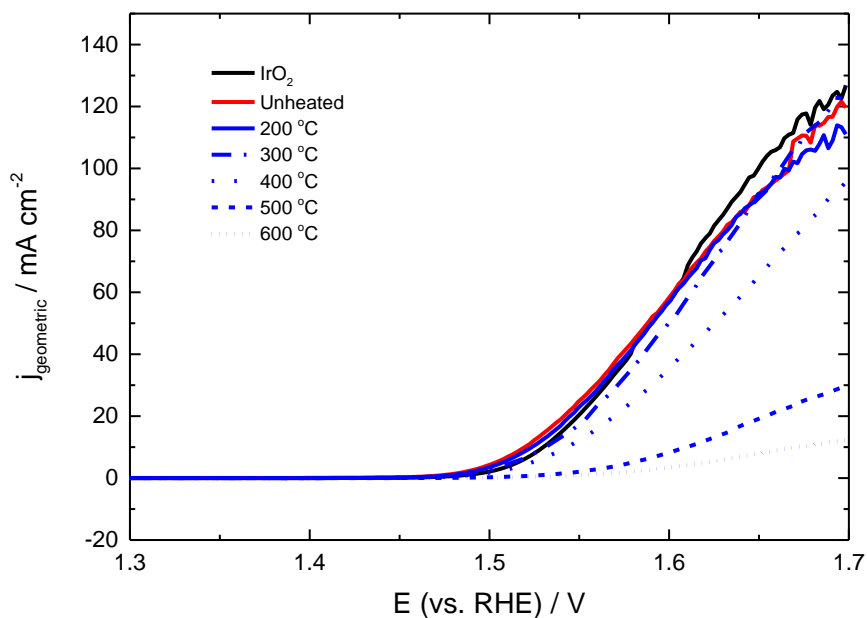


Figure 20 Steady state polarisation of 40 % Ir/ITO samples unheated (red line) and heated in air at 200 (solid blue line), 300 (dash-dot blue line), 400 (short dash blue line), 500 (dash blue line) and 600 °C (blue dot line) for 30 min. The samples are compared to IrO_2 (black line). Recorded in 0.5 M H_2SO_4 at 1 mV s^{-1}

Steady state polarisation curves of the 40 % Ir/ITO catalysts heated in a N_2 atmosphere are shown in figure 21. It is observed that heating under N_2 decreases the OER activity with respect to the unheated sample, however there is little difference between the samples heated at 300 and 500 °C. It is also noted that the sample heated at 500 °C in N_2 displays considerably greater activity than the sample heated at the same temperature in air. This may be due to the sample heated in N_2 retaining more of the metallic Ir structure than the sample heated in air, which was completely oxidised to IrO_2 . As the heating temperature is increased to 700 °C, there is a large decrease in activity which may be a result of the Ir particle agglomeration in addition to the oxidation of some of the Ir, as indicated by the XRD analysis.

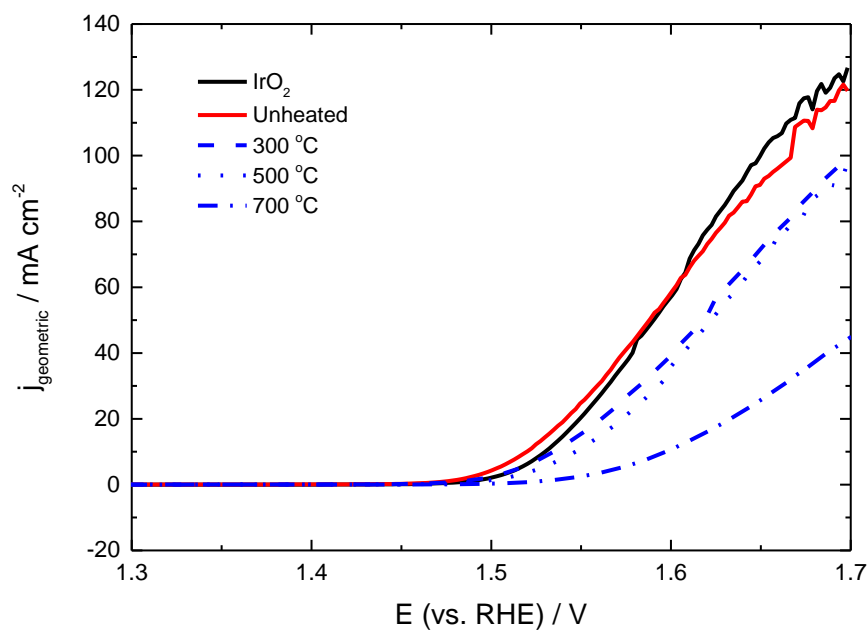


Figure 21 Steady state polarisation of 40 wt. % Ir/ITO unheated (red line) and heated at 300 (dashed blue line), 500 (dot blue line line) and 700 °C (dot-dash blue line) under flowing N_2 for 30 min in 1 M H_2SO_4 at a sweep rate of 1 mV s^{-1} . Samples are compared to IrO_2 (black line).

4.3.2.6 In situ XANES

The average oxidation state of the Ir in the unheated 40 wt. % Ir/ITO catalyst and the sample heated in N_2 at 500 °C as a function of the applied potential was investigated by in situ XANES measurements collected at the Ir L_3 edge. Prior to collecting XANES spectra, cyclic voltammograms of the catalysts in the in-situ electrochemical cell were collected at 50 mV s^{-1} . The voltammograms in figure 22 show that the curves display a similar profile to the voltammetry observed with the thin film RDE experiments.

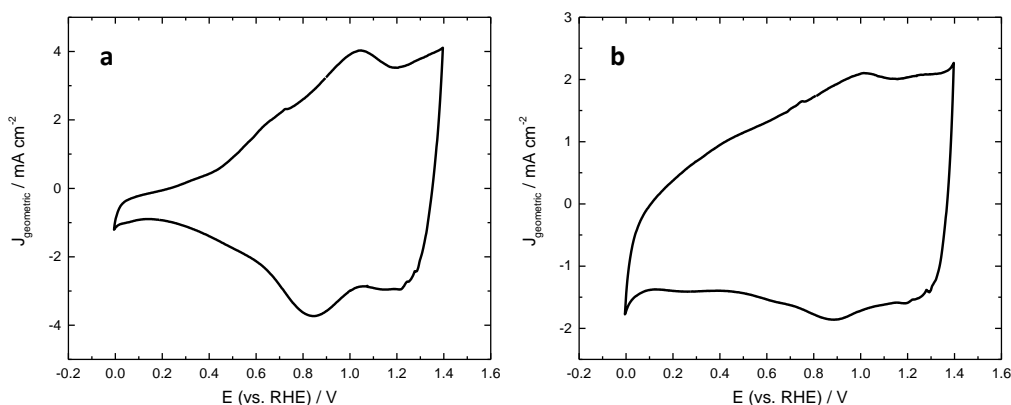


Figure 22 Cyclic voltammetry of the 40 % Ir/ITO catalyst unheated (a) and heated at 500 °C in N_2 (b) button electrodes in the in-situ XAS cell in 0.5 M H_2SO_4 at 50 mV s^{-1}

Ir L_3 edge XANES spectra of the 40 wt. % Ir/ITO unheated and heated at 500 °C in a N_2 atmosphere, as a function of the applied potential are presented in figure 23 and 24 respectively. The position of the Ir L_3 edge was determined by the peak maximum of the white line intensity. Figure 25 shows the energy shift of the Ir L_3 edge position from the tabulated value of $Ir^0 E_0$ (11215 eV), as a function of the applied potential. The energy shift of the supported catalysts is compared to the unsupported IrO_2 sample data presented in Chapter 3. The actual Ir oxidation state of the catalyst as a function of potential was determined using the calibration curve of the Ir reference samples, as detailed in Chapter 3. Table 5 compares the Ir oxidation state of the supported catalysts to the IrO_2 sample.

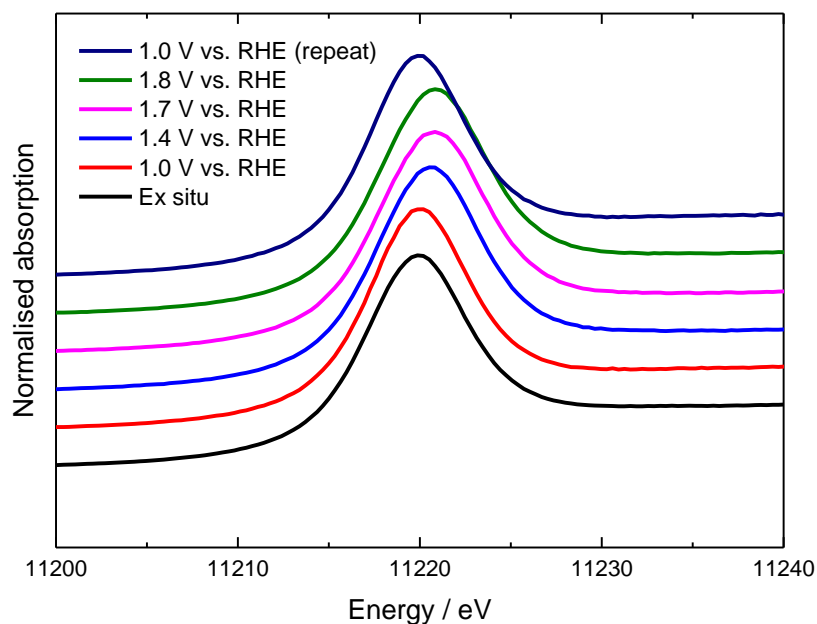


Figure 23 Ir L_3 edge XANES of 40 % Ir/ITO recorded ex situ (black line) and in situ at a potential of 1.0 (red line), 1.4 (blue line), 1.7 (pink line), 1.8 (green line) and 1.0 V (repeat) (purple line) vs. RHE.

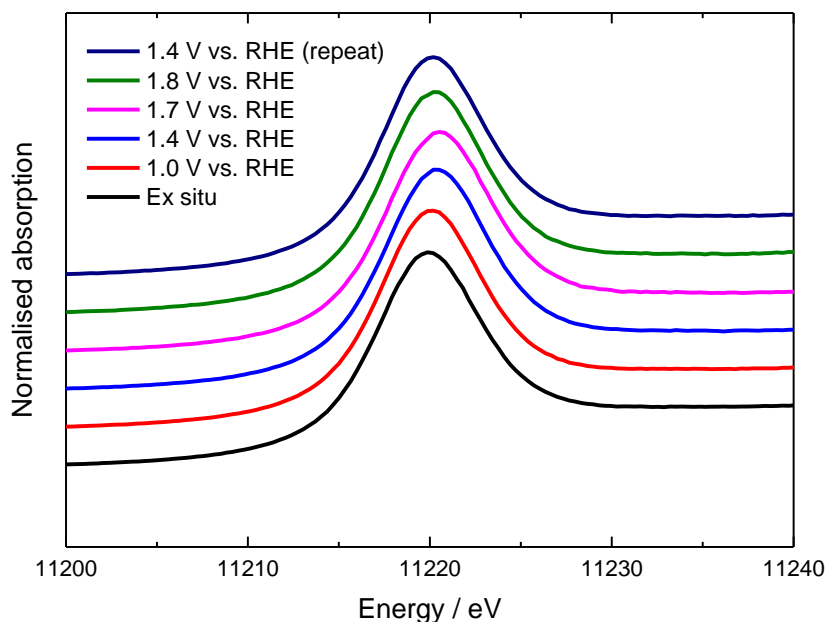


Figure 24 Ir L_3 edge XANES of 40 % Ir/ITO 500 N_2 recorded ex situ (black line) and in situ at a potential of 1.0 (red line), 1.4 (blue line), 1.7 (pink line), 1.8 (green line) and 1.0 V (repeat) (purple line) vs. RHE.

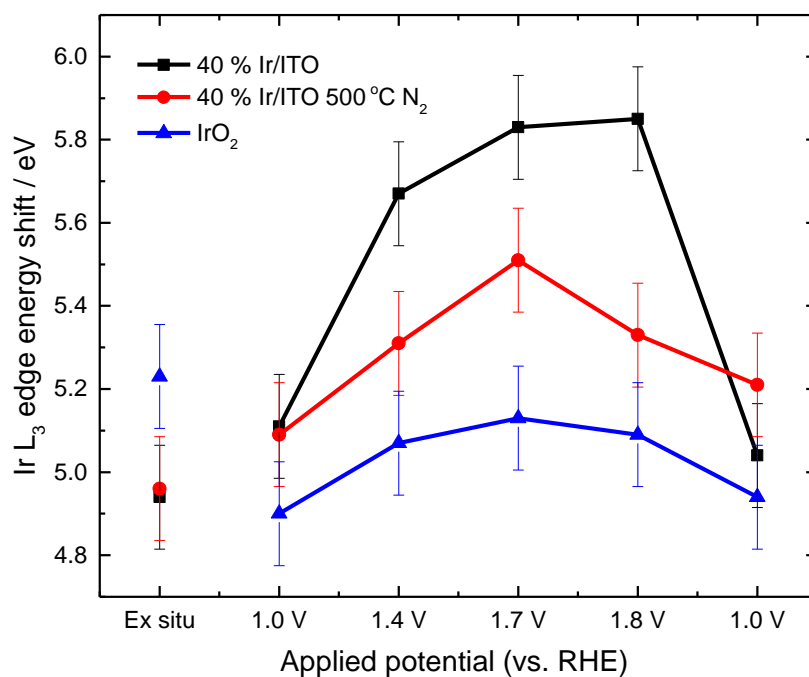


Figure 25 Ir L₃ edge energy shift of 40 % Ir/ITO (black line), 40 % Ir/ITO (500 °C, N₂) (red line) and IrO₂ (blue line) as a function of the applied potential

Table 5 Calibrated Ir oxidation states of supported Ir samples as a function of applied potential

Sample	Oxidation state					
	Ex situ	1.0 V	1.4 V	1.7 V	1.8 V	1.0 V (repeat)
40 % Ir/ITO	4.1 ± 0.9	4.3 ± 0.9	4.7 ± 0.9	4.9 ± 0.9	4.9 ± 0.9	4.2 ± 0.9
40 % Ir/ITO (500 N ₂)	4.2 ± 0.9	4.3 ± 0.9	4.4 ± 0.9	4.6 ± 0.9	4.5 ± 0.9	4.4 ± 0.9
IrO ₂	4.4 ± 0.9	4.1 ± 0.9	4.2 ± 0.9	4.3 ± 0.9	4.3 ± 0.9	4.1 ± 0.9

The Ir L₃ K edge XANES of the unheated 40 % Ir/ITO catalyst and the sample heated at 500 °C in N₂ in figures 23 and 24 respectively, in addition to the plot of Ir L₃ edge energy shift as a function of potential in figure 25, show that the position of the Ir L₃ white line intensity shifts to higher energies as the potential is increased. This indicates that the Ir oxidation state in both

Chapter 4: Ir/ITO electrocatalysts for the O₂ evolution reaction

catalyst samples increases during O₂ evolution. The calibrated data in table 5 suggests that the average Ir oxidation state of the unheated sample increases from 4.3 ± 0.9 V at 1.0 V, to 4.9 ± 0.9 at 1.8 V, while the sample heated at 500 °C in N₂ increases from an average Ir oxidation state of 4.3 ± 0.9 V at 1.0 V, to 4.5 ± 0.9 at 1.8 V. Both of these trends supports the model that on Ir-based electrocatalysts, O₂ evolution occurs concurrently with the oxidation of the Ir to valencies > 4 ^{29,49}.

The increase in the Ir oxidation state of the 40 % Ir/ITO catalyst is much greater than that observed for the heat treated sample, and also than the IrO₂ catalyst which increases from 4.1 ± 0.9 V to 4.3 ± 0.9 over the same potential range. This indicates that the average oxidation state of the Ir in the amorphous 40 % Ir/ITO catalyst at O₂ evolution potentials is higher than in the two other crystalline catalysts. This is most likely due to the much greater electrochemical surface area of the highly hydrated 40 % Ir/ITO, as indicated by the cyclic voltammetry. Consequently, a larger number of Ir sites are subjected to oxidation than on the crystalline Ir or IrO₂ nanoparticles, on which only a smaller number of surface sites take part in the O₂ evolution reaction⁵⁰. This hypothesis agrees with the conclusions of Minguzzi et al. in their FEXAFS study that compared nanoparticle IrO₂ to hydrous electrodeposited Ir oxide films³⁵.

4.4 Conclusions

In this chapter, supported Ir/ITO electrocatalysts have been investigated as a means of decreasing the Ir content of the catalyst for the O₂ evolution reaction in PEM water electrolyzers. A series of catalysts were prepared with Ir loadings from 40 – 5 wt. %, using a formaldehyde reduction method. TEM and EDX analysis showed that the prepared catalysts consisted of nanoparticulate Ir dispersed on the ITO support, while XRD and EXAFS suggested that these deposits were amorphous in nature with little long range structure.

Electrochemical characterisation of the Ir/ITO catalysts in 0.5 M H₂SO₄ indicated that the Ir/ITO system shows very good performance for O₂ evolution that is comparable to the activity of IrO₂. The catalytic activity was found to decrease with the Ir loading which was ascribed to the reduction in amount of active phase on the support. The mass activity as determined at 1.60 V suggests an optimal loading in terms of the cost effectiveness of the catalyst, of 20 wt. % Ir. Single cell PEM cell testing highlighted the very promising performance of the 40 and 20 wt. % Ir/ITO catalysts compared to state-of-the-art IrO₂, with the 40 % Ir/ITO sample showing excellent stability over a 600 h test period. This result indicates that the 40 % Ir/ITO catalyst

has significant potential as a lower-cost alternative to IrO₂ for commercial PEM electrolyser systems.

The high activity of the catalysts was attributed to the highly amorphous and hydrated structure of the Ir that facilitates a very high electrochemical surface area. This hypothesis is supported by the investigation into the effect of the heat treatment of 40 wt. % Ir/ITO, in both oxidising and non-oxidising conditions. The heat treatment modifies the performance of the 40 % Ir/ITO as an O₂ evolution catalyst, decreasing the activity with respect to the unheated sample. The decrease is attributed to the loss of the hydrated oxide structure in addition to the formation of the crystalline IrO₂ at temperatures ≥ 500 °C, as indicated by XRD and EXAFS measurements.

4.5 References

- (1) García, G.; Roca-Ayats, M.; Lillo, A.; Galante, J. L.; Peña, M. A.; Martínez-Huerta, M. V. *Catalysis Today* **2013**, *210*, 67.
- (2) Costamagna, P.; Srinivasan, S. *Journal of Power Sources* **2001**, *102*, 242.
- (3) Kinoshita, K. *Carbon: Electrochemical and Physicochemical Properties*; Wiley: New York, 1987.
- (4) Mazúr, P.; Polonský, J.; Paidar, M.; Bouzek, K. *International Journal of Hydrogen Energy* **2012**, *37*, 12081.
- (5) Fuentes, R. E.; Farrell, J.; Weidner, J. W. *Electrochemical and Solid-State Letters* **2011**, *14*, E5.
- (6) Xu, J.; Liu, G.; Li, J.; Wang, X. *Electrochimica Acta* **2012**, *59*, 105.
- (7) Antolini, E.; Gonzalez, E. R. *Solid State Ionics* **2009**, *180*, 746.
- (8) Siracusano, S.; Baglio, V.; D'Urso, C.; Antonucci, V.; Aricò, A. S. *Electrochimica Acta* **2009**, *54*, 6292.
- (9) Chen, G.; Bare, S. R.; Mallouk, T. E. *Journal of The Electrochemical Society* **2002**, *149*, A1092.
- (10) Hu, W.; Chen, S.; Xia, Q. *International Journal of Hydrogen Energy* **2014**, *39*, 6967.
- (11) Thomassen, M. S.; Mokkelbost, T.; Sheridan, E.; Lind, A. *ECS Transactions* **2011**, *35*, 271.
- (12) Wu, X.; Scott, K. *International Journal of Hydrogen Energy* **2011**, *36*, 5806.
- (13) Xu, J.; Li, Q.; Hansen, M. K.; Christensen, E.; Tomás García, A. L.; Liu, G.; Wang, X.; Bjerrum, N. J. *International Journal of Hydrogen Energy* **2012**, *37*, 18629.

Chapter 4: Ir/ITO electrocatalysts for the O₂ evolution reaction

- (14) Cruz, J. C.; Rivas, S.; Beltran, D.; Meas, Y.; Ornelas, R.; Osorio-Monreal, G.; Ortiz-Frade, L.; Ledesma-García, J.; Arriaga, L. G. *International Journal of Hydrogen Energy* **2012**, *37*, 13522.
- (15) Marshall, A. T.; Haverkamp, R. G. *Electrochimica Acta* **2010**, *55*, 1978.
- (16) Avila-Vazquez, V.; Cruz, J. C.; Galvan-Valencia, M.; Ledesma-Garcia, J.; Arriaga, L. G.; Guzman, C.; Duron-Torres, S. M. *International Journal of Electrochemical Science* **2013**, *8*, 10586.
- (17) Haverkamp, R. G.; Marshall, A. T.; Cowie, B. C. C. *Surface and Interface Analysis* **2010**, n/a.
- (18) Marshall, A.; Børresen, B.; Hagen, G.; Tsyarkin, M.; Tunold, R. *Energy* **2007**, *32*, 431.
- (19) Carmo, M.; Fritz, D. L.; Mergel, J.; Stolten, D. *International Journal of Hydrogen Energy* **2013**, *38*, 4901.
- (20) Yamaguchi, M.; Ide-Ektessabi, A.; Nomura, H.; Yasui, N. *Thin Solid Films* **2004**, *447–448*, 115.
- (21) Fan, J. C. C.; Goodenough, J. B. *Journal of Applied Physics* **1977**, *48*, 3524.
- (22) Chhina, H.; Campbell, S.; Kesler, O. *Journal of Power Sources* **2006**, *161*, 893.
- (23) Puthiyapura, V. K.; Pasupathi, S.; Su, H.; Liu, X.; Pollet, B.; Scott, K. *International Journal of Hydrogen Energy* **2014**, *39*, 1905.
- (24) Adams, R.; Shriner, R. L. *Journal of the American Chemical Society* **1923**, *45*, 2171.
- (25) Antolini, E. *Journal of Materials Science* **2003**, *38*, 2995.
- (26) Goodenough, J. B.; Hamnett, A.; Kennedy, B. J.; Manoharan, R.; Weeks, S. A. *Electrochimica Acta* **1990**, *35*, 199.
- (27) Singh, H. P. *Acta Crystallographica Section A* **1968**, *24*, 469.
- (28) Nadaud, N.; Lequeux, N.; Nanot, M.; Jové, J.; Roisnel, T. *Journal of Solid State Chemistry* **1998**, *135*, 140.
- (29) Kotz, R.; Neff, H.; Stucki, S. *Journal of The Electrochemical Society* **1984**, *131*, 72.
- (30) Andreas, H.; Elzanowska, H.; Serebrennikova, I.; Birss, V. *Journal of The Electrochemical Society* **2000**, *147*, 4598.
- (31) Ouattara, L.; Fierro, S.; Frey, O.; Koudelka, M.; Comninellis, C. *Journal of Applied Electrochemistry* **2009**, *39*, 1361.
- (32) Burke, L. D.; O'Sullivan, E. J. M. *Journal of Electroanalytical Chemistry and Interfacial Electrochemistry* **1981**, *117*, 155.
- (33) Gottesfeld, S.; Srinivasan, S. *Journal of Electroanalytical Chemistry and Interfacial Electrochemistry* **1978**, *86*, 89.

Chapter 4: Ir/ITO electrocatalysts for the O₂ evolution reaction

- (34) McIntyre, J. D. E.; Peck, W. F.; Nakahara, S. *Journal of The Electrochemical Society* **1980**, *127*, 1264.
- (35) Minguzzi, A.; Lugaresi, O.; Locatelli, C.; Rondinini, S.; D'Acapito, F.; Achilli, E.; Ghigna, P. *Analytical Chemistry* **2013**, *85*, 7009.
- (36) Conway, B. E.; Mozota, J. *Electrochimica Acta* **1983**, *28*, 9.
- (37) Mozota, J.; Conway, B. E. *Electrochimica Acta* **1983**, *28*, 1.
- (38) Birss, V. I.; Bock, C.; Elzanowska, H. *Canadian Journal of Chemistry* **1997**, *75*, 1687.
- (39) Lervik, I. A.; Tsyppkin, M.; Owe, L.-E.; Sunde, S. *Journal of Electroanalytical Chemistry* **2010**, *645*, 135.
- (40) Pauporté, T.; Andolfatto, F.; Durand, R. *Electrochimica Acta* **1999**, *45*, 431.
- (41) Frazer, E. J.; Woods, R. *Journal of Electroanalytical Chemistry and Interfacial Electrochemistry* **1979**, *102*, 127.
- (42) Tang, L.; Li, X.; Cammarata, R. C.; Friesen, C.; Sieradzki, K. *Journal of the American Chemical Society* **2010**, *132*, 11722.
- (43) Li, G.; Yu, H.; Wang, X.; Sun, S.; Li, Y.; Shao, Z.; Yi, B. *Physical Chemistry Chemical Physics* **2013**, *15*, 2858.
- (44) Siracusano, S.; Baglio, V.; Stassi, A.; Ornelas, R.; Antonucci, V.; Aricò, A. S. *International Journal of Hydrogen Energy* **2011**, *36*, 7822.
- (45) Cruz, J.; Baglio, V.; Siracusano, S.; Antonucci, V.; Arico, A. S.; Ornelas, R.; Ortiz-Frade, L.; Osorio-Monreal, G.; Duron-Torres, S. M.; Arriaga, L. *International Journal of Electrochemical Science* **2011**, *6*, 6607.
- (46) Li, G.; Yu, H.; Song, W.; Wang, X.; Li, Y.; Shao, Z.; Yi, B. *International Journal of Hydrogen Energy* **2012**, *37*, 16786.
- (47) Bolzan, A. A.; Fong, C.; Kennedy, B. J.; Howard, C. J. *Acta Crystallographica Section B* **1997**, *53*, 373.
- (48) Silva, T. M.; Simões, A. M. P.; Ferreira, M. G. S.; Walls, M.; Da Cunha Belo, M. *Journal of Electroanalytical Chemistry* **1998**, *441*, 5.
- (49) Huppaufl, M.; Lengeler, B. *Journal of The Electrochemical Society* **1993**, *140*, 598.
- (50) Fierro, S.; Nagel, T.; Baltruschat, H.; Comninellis, C. *Electrochemistry Communications* **2007**, *9*, 1969.

5. Conclusions

The aim of this thesis has been to prepare and investigate Ir-based nanoparticle electrocatalysts with reduced Ir contents, so as to aid the development of lower-cost O₂ evolution catalysts for the anode of PEM water electrolyzers. The introduction highlighted two methods to reduce the Ir content of the electrocatalyst that were subsequently investigated in Chapters 3 and 4, (i) mixing the Ir with Ru to form a binary metal oxide and (ii) dispersing the active Ir phase on an ITO support.

The Adams fusion method was used to prepare binary Ir_xRu_yO₂ metal oxides across the composition range, from IrO₂ to RuO₂. TEM observations and XRD analysis showed that these oxides comprised nanoparticles of about 5 – 20 nm in diameter. Evidence for the formation of solid solution binary oxides was also presented. More conclusive proof of solid solution formation could be achieved in future work through the use of Rietveld refinement of the XRD patterns, so as to determine the lattice parameters of the oxides and explore how they change with composition. The enhancement in the electrocatalytic activity of the Ir_xRu_yO₂ towards the O₂ evolution reaction with the addition of Ru was clearly demonstrated by electrochemical testing in both 0.5 M H₂SO₄ and in a single cell PEM electrolyser. Meanwhile the stability of the oxide catalysts was shown to increase with the addition of Ir.

The interaction between the Ir and Ru in the Ir_xRu_yO₂ electrocatalysts during O₂ evolution was investigated by in situ XANES measurements. This experiment involved the design and construction of an in-situ cell that enabled XANES measurements to be made whilst holding the catalyst electrode at potentials in the operating range of a PEM water electrolyser (i.e. ≥ 1.70 V). The analysis presented evidence of a direct interaction between the Ir and Ru components at O₂ evolution potentials. It was shown that the Ir has a stabilising effect on the RuO₂ component, preventing the Ru from being oxidised to higher, unstable oxidation states. In contrast, the Ir oxidation state remains largely unchanged at O₂ evolution operating potentials. Although the increase in oxidation state from the IrO₂ to the mixed metal oxides suggests that the Ru may increase the activity of the Ir component. Determination of the oxidation state of the Ir and the Ru suggested that O₂ evolution on Ir and Ru oxides occurs with the metals in oxidation states greater than 4, consistent with previous published results with Ir_xRu_yO₂ electrocatalysts¹⁻³.

Supported Ir/ITO electrocatalysts with variable Ir loadings were prepared by a formaldehyde reduction method. TEM and EDX analysis showed that the prepared catalysts consist of

Chapter 5: Conclusions

nanoparticulate Ir dispersed on the ITO support, while XRD and EXAFS suggested that these deposits were amorphous in nature with little long range structure. Electrochemical characterisation indicated that the Ir/ITO system shows a very good performance as anode catalysts in PEM electrolyzers. The 40 % Ir/ITO sample shows particular promise as an alternative catalyst to IrO₂ as it exhibited a lower cell voltage at 1 A cm⁻² in the PEM cell over a 600 h test period. This result indicates that the 40 % Ir/ITO catalyst has significant potential as a lower-cost alternative to IrO₂ for commercial PEM electrolyser systems. The high activity of the Ir/ITO catalysts was attributed to the highly amorphous and hydrated structure of the Ir that facilitates a very high electrochemical surface area, a hypothesis that was supported by investigating the effect of the heat treatment of 40 wt. % Ir/ITO, in both oxidising and non-oxidising conditions.

In order to decrease the cost of PEM water electrolyzers, the goals of O₂ electrocatalyst development are to: (i) enhance the electrocatalytic activity so as to increase the H₂ yield per applied voltage and thus the energy efficiency of the catalyst, (ii) increase the stability of the catalyst, and (iii) lower the cost of the catalyst by reducing the amount of Ir and/or increase the utilisation of the Ir. The decision as to which catalyst to choose is likely to be a careful consideration of all three requirements. In figure 1 the electrocatalytic activity of the Ir_xRu_yO₂, 40 % Ir/ITO and the 20 % Ir/ITO samples are plotted against their electrochemical stability. The activities presented are determined from the cell potentials observed from the PEM electrolyser polarisation curves at 1 A cm⁻², while the stability is determined by the rate of cell voltage increase over 600 h. The optimal catalyst would be in the bottom left corner of the plot however it is readily apparent that none of the catalysts fulfil both criteria. Adding small amounts of Ru to IrO₂ (i.e. > 50 mol %) certainly has merit, as the small increase in activity compared to IrO₂ is not tempered with a significant decrease in stability. It is noted however that the current study is limited to a test period of 600 h and further long term testing would be required to see whether this activity benefit would continue beyond 600 h. The 40 % Ir/ITO catalyst offers a similar improvement in activity although the stability is more negatively affected than the Ir_xRu_yO₂ samples.

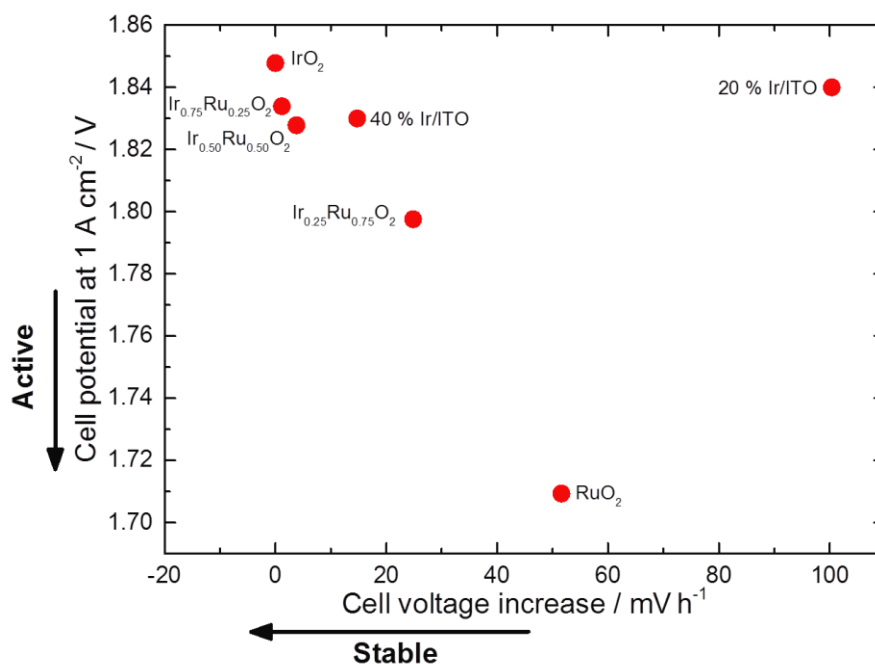


Figure 1 Classification of $\text{Ir}_x\text{Ru}_y\text{O}_2$ and Ir/ITO electrocatalysts by activity in terms of cell potential at 1 A cm^{-2} and stability in terms of the rate of cell voltage increase (mV h^{-1}) over 600 h

Figure 2 presents the mass activities of the catalysts at 1.60 V vs. RHE in 0.5 M H_2SO_4 plotted against their electrochemical stabilities. The mass activity was determined by normalising the recorded current density of the linear sweep voltammetry by the Ir loading, with the exception of the RuO_2 sample which was normalised by the Ru loading. The plot shows that the 40 % Ir/ITO catalyst utilises its Ir content far more efficiently than the $\text{Ir}_{0.75}\text{Ru}_{0.25}\text{O}_2$ and $\text{Ir}_{0.50}\text{Ru}_{0.50}\text{O}_2$, as the mass activity of the supported sample is approximately twice that of the $\text{Ir}_{0.50}\text{Ru}_{0.50}\text{O}_2$ sample and six times greater than the $\text{Ir}_{0.75}\text{Ru}_{0.25}\text{O}_2$ sample. Enhancement to the stability of the 40 % Ir/ITO catalyst, possibly through the use of an optimised heat treatment, would lead to greater synergy between catalyst utilisation and catalyst stability.

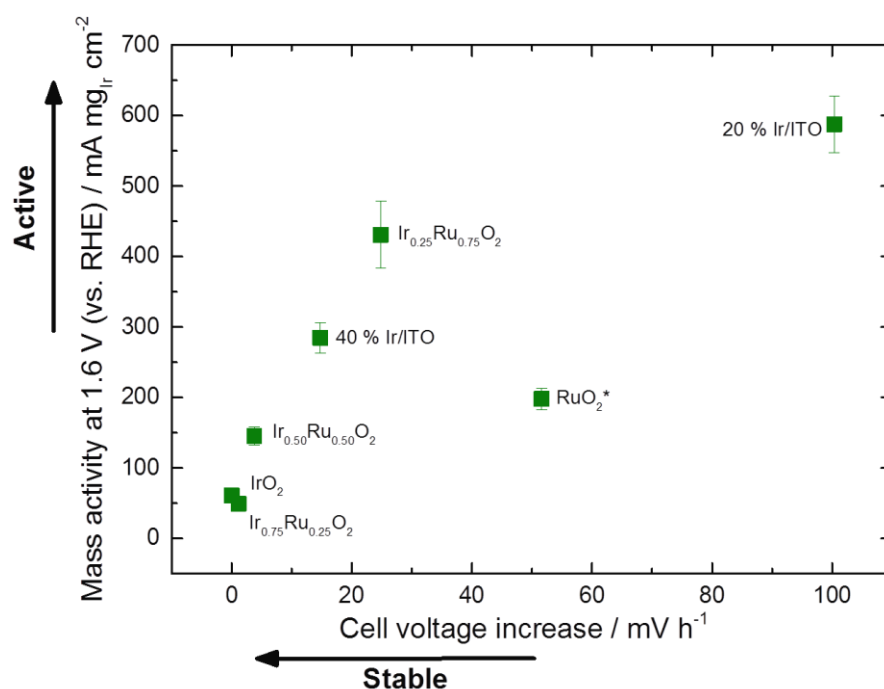


Figure 2 Classification of Ir_xRu_yO₂ and Ir/ITO electrocatalysts by activity in terms of mass activity at 1.60 V vs. RHE in 0.5 M H₂SO₄ and stability in terms of the rate of cell voltage increase (mV h⁻¹) over 600 h. The mass activity is determined by normalisation of the observed current densities by the Ir loading, with the exception of the RuO₂ sample which is normalised by the Ru loading.

Comparing the cost of different catalysts is slightly more difficult than comparisons of catalyst activity and stability, as it is influenced by such variable factors as the price of the composite materials and the costs of production. Nonetheless, figure 3 presents a plot of the monthly average price of Ir and Ru on the global stock markets since 2010, as reported by Johnson Matthey⁴. The plot highlights the far higher cost of Ir compared to Ru, in addition to the large fluctuations in the Ir price over the last five years. In comparison, the cost per gram of the ITO used in this work was US\$ 30 g⁻¹. Based on these prices the use of ITO appears to have no economic benefit, however the stock market price does not reflect the true cost of purchasing catalysts such as IrO₂ or Ir black, or the catalyst precursor chemicals. Furthermore, the cost of Ir is currently retarded by the fact that it has few industrial applications⁵. Were the production of PEM electrolyzers to go into mass production, the cost of Ir would likely increase significantly due to the uptake in demand.

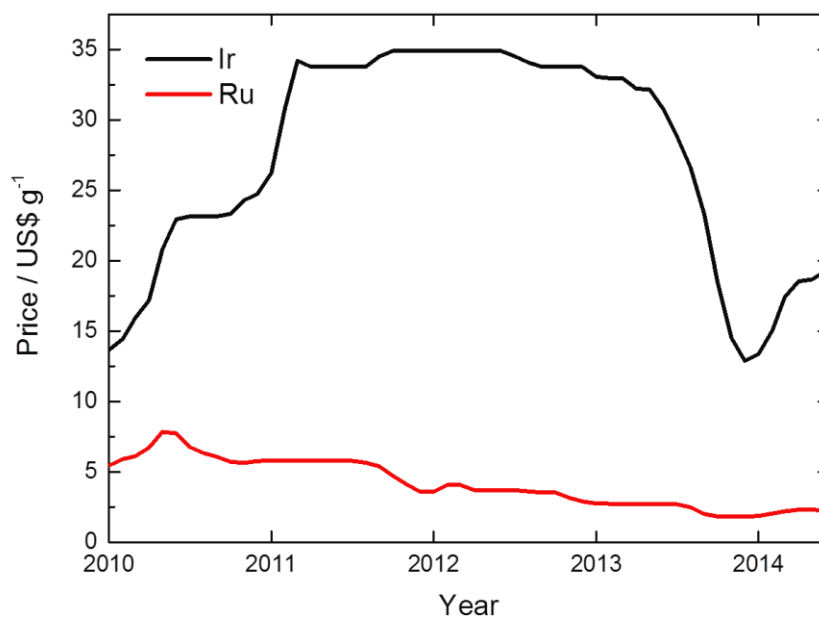


Figure 3 Monthly average price of Ir and Ru since 2010 as reported by Johnson Matthey

A fairer, up-to-date comparison of the cost of the different catalysts is made in table 1 which lists the cost per gram and the cost per gram of Ir/Ru, of the catalyst precursors used in this work ($\text{H}_2\text{IrCl}_6 \cdot x\text{H}_2\text{O}$, $\text{RuCl}_3 \cdot x\text{H}_2\text{O}$ and ITO), in addition to commercial catalysts IrO_2 and Ir black from three different suppliers (Alfa Aesar⁶, Sigma-Aldrich⁷ and Strem Chemicals⁸). The prices in the table show that the cost per gram of commercial IrO_2 (US\$ 140-196) or Ir black (US\$ 150-270) catalysts is far greater than the cost of the ITO (US\$ 30). The cost per gram of the precursor chemical $\text{H}_2\text{IrCl}_6 \cdot x\text{H}_2\text{O}$ (US\$ 67) is slightly more comparable to ITO. However normalising the price of the various materials to the cost per gram of Ir reveals that the cost of purchasing the precursor (US\$ 168) for use in a PEM electrolyser is just as expensive as IrO_2 (US\$ 166-232) and Ir black (US\$ 150-270). The cost analysis therefore suggests that the use of a support such as ITO, can lead to significant savings in the cost of the O_2 evolution electrocatalyst.

Table 1 Cost per gram and per gram of Ir or Ru of the catalyst starting materials compared to IrO₂ and Ir black from three different suppliers: Sigma-Aldrich, Alfa Aesar and Strem Chemicals

Material	Supplier	Cost per gram / US\$ g ⁻¹	Cost per gram of Ir or Ru / US\$ g _{Ir or Ru} ⁻¹
ITO	Sigma-Aldrich	30	n/a
IrO ₂ (99.9 %)	Sigma-Aldrich	174	206
IrO ₂ (99.99 %)	Alfa Aesar	196	232
IrO ₂ (99 %)	Strem Chemicals	140	166
Ir black (99.9 %)	Strem Chemicals	150	150
Ir black (99.95 %)	Alfa Aesar	157	157
Ir black (≥ 99 %)	Sigma-Aldrich	270	270
RuCl ₃ .xH ₂ O (38 % Ru)	Alfa Aesar	21	56
H ₂ IrCl ₆ . xH ₂ O (40 % Ir)	Alfa Aesar	67	168

In conclusion, this work has shown that it is possible to reduce the Ir content of O₂ evolution electrocatalysts via the mixing of IrO₂ with RuO₂ or by the effective use of a suitable support material such as ITO. Although selection of the most appropriate catalyst may ultimately be a compromise between activity, stability and cost, the work provides possible directions for electrocatalyst research that may be applicable to commercial PEM electrolyser manufacturers. Future work should perhaps explore supported Ir_xRu_yO₂ catalysts so as to reduce the cost of the catalysts yet further. The interaction between the supported electrocatalysts and the PEM electrolyte could also be investigated through such techniques as electronic impedance spectroscopy.

5.1 References

- (1) Kotz, R.; Neff, H.; Stucki, S. *Journal of The Electrochemical Society* **1984**, *131*, 72.
- (2) Kotz, R.; Lewerenz, H. J.; Stucki, S. *Journal of The Electrochemical Society* **1983**, *130*, 825.
- (3) Huppaufl, M.; Lengeler, B. *Journal of The Electrochemical Society* **1993**, *140*, 598.
- (4) Johnson Matthey, Platinum Today price charts,
<http://www.platinum.matthey.com/prices/price-charts>, Accessed 05/01/2015.

- (5) *CRC Handbook of Chemistry and Physics*; 95th ed.; CRC Press: Boca Raton, USA, 2014.
- (6) Alfa Aesar, <http://www.alfa.com/>, Accessed 05/01/2015.
- (7) Sigma-Aldrich, www.sigmaaldrich.com, Accessed 05/01/2015.
- (8) Strem Chemicals Inc, <http://www.strem.com/catalog/>, Accessed 05/01/2015.